CAAP: Embedded Passive RF Tags towards Intrinsically Locatable Buried Plastic Material

Contract Number: DTPH5615HCAP08L

University Contact:

Saikat Mondal, Deepak Kumar, Prem Chahal (Co-PI) and Yiming Deng (PI)

Phone: (517)884-0926, Email: dengyimi@egr.msu.edu

AOR Contact:

Joshua Arnold, R&D Program Manager, PHMSA/DOT

Email: joshua.arnold@dot.gov

Arthur Buff, Project Manager, PHMSA/DOT

Email: Arthur.buff@dot.gov

Department of Electrical and Computer Engineering

Michigan State University, East Lansing, Michigan 48824

Department of Electrical Engineering

University of Colorado Denver, Denver, Colorado 80217

Table of Contents

Introduction and Background

Buried pipes are expected to have a lifetime of greater than 30 years that are designed to carry a range of liquid and gaseous materials. Among the many pipe technologies, demand for plastic pipes is growing largely because of their low-cost and potential for long life time. Any tags or sensors that are incorporated within these pipes should be able to withstand harsh conditions with a lifetime meeting or exceeding that of the pipes, and should be battery free (passive tag). Furthermore, the overall system should be compact, low-cost, and easy to operate. With advanced techniques to bury the pipes using tunneling approaches it is necessary that tags withstand the associated stress and handling during construction work. Typically, the pipes are buried 3 feet or deeper in the ground and thus the reader should be able to interrogate the tags at these and at higher depths.

There are several challenges that exist with current technologies. Over the last few decades, ground penetrating radars (GPR) have been used in determining buried pipes. One of the key challenges with RF interrogation of buried object is that the signal to noise (S/N) ratio of the reflected signal is weak. The reflected signal from buried dielectric object is even less than a metal object. Furthermore, the reflected signal from ground and other objects (clutter) is many orders of magnitude larger than the signal reflected back from a buried object thus obscuring signal from target of interest. A common approach to overcome clutter includes time gating of pulsed signal in a GPR. Furthermore, very elaborate radar systems have been designed to overcome the S/N challenge, thus making them cost prohibitive. To enhance sensitivity of GPR and overcome clutter challenge, use of electronic markers (wireless tags) have been proposed as a low-cost solution. These markers have to be incorporated during installment of the infrastructure. Wireless passive tags are attractive for determination of buried objects as they reduce the complexity of the electronics compared to conventional GPR and also it allows in the specific marking of individual objects. Some common near field passive sensors include magnetoelastic, inductive-capacitive (LC) and surface acoustic. 3M offers a range of electronic markers for buried utility lines. Each type of utility line is marked using distinct resonant frequencies (example: 83KHz for gas, 145.7KHz for water, 169.8KHz for power, 101.4KHz for telephone). These passive electronic markers are usually color-coded according to the particular type of utility line they mark. These markers operate on the principle of LC resonant tanks (magnetically coupled resonant tank). They are resonantly responsive to an electromagnetic wave of a specific frequency sent from above the ground surface. Identification is incorporated by modulating the resonant frequency of the LC circuit using a CMOS circuit (ASIC) which is used to modulate the value of the capacitor. The challenge LC resonators is that the size of tag is large and the overall materials cost can also be high. The LC coil has to be less than a wavelength (λ) in distance away from the reader for efficient coupling. Thus, for larger penetration depths lower frequency or large wavelength of operation is desired. Sensors with larger inductive coil (loop or coil antenna) are used for detection at larger depths. Lower resonant frequencies coupled with larger coils are used to achieve efficient coupling between the transmitter and the passive tag to meet the depth requirements. The size of the markers can be reduced by loading the circuit with a magnetic material having large permeability (μ_r). An electronic marker based on this principle called OXEMS has been introduced in the UK as discussed in Introduction. The challenge with this technique is that the magnetic materials used are expensive and also these materials are prone to corrosion. Because of their large size these circuits will be difficult to directly embed within the plastic pipes.

Passive RFID systems, especially working in the 900MHz frequency band, have experienced tremendous growth in recent years and these operate in the far-field region (coupling at longer than a wavelength in distance) through the use of RF antennas. These tags are significantly small compared to the LC resonant type (near field) structures, can be fabricated in thin film form and are low-cost. Applications of these RFID include E-passport, smart cards, access control, and supply chain management to name a few. These RFIDs

are low cost and are readily available. A conventional RFID system which is categorized as class-1 is composed of a reader and a passive transponder. The transponder consists of an antenna and a CMOS chip. The chip receives the power from the antenna which then modulates the backscattered signal from the antenna; by altering the load impedance of the antenna. Modulation is pre-programmed in the chip which translates to their IP address. Most class-1 readers show a short range limited to about 5m in free space. It can use frequency bands (125 – 134.2KHz, 13.56MHz, 860 – 960MHz, 2.45 GHz) without a license. Nevertheless, RFIDs have to be compliant with local regulations (e.g., FCC). Apart from identification, RFIDs have been adapted to carry out wireless sensing where by the sensing elements directly or indirectly loads the antenna elements which translates into change in radiation pattern and efficiency. However, these techniques have not been adopted in buried pipe applications.

One of the biggest challenges associated with adopting existing RFIDs is that the S/N ratio is low due to interference. It has a low dynamic range and the receiving sensitivity is in therange of -60dBm to -70dBm. In these systems the continuous wave (CW) that powers up the signal is inevitably coupled to the receiver input as a strong self-interference. Filters are inefficient in reducing the interference as the frequency of the transmitted and scattered signal is very close. Different approaches, with varying complexity, have been explored for the design of readers with reduced cross coupled signal including: a) direct-conversion receiver with baseband DC blocking capacitor, b) active carrier cancellation at the receiver input, c) use of cross-polar reader transmitter and receiver antennas. Apart from cross coupling, for application in detecting buried tag, these readers will face significant challenge as the reflected signal form the surface is significantly large as compared to from the tag and suppressing this clutter is very difficult. At present, the maximum read depth of these RFIDs when buried is less than 2 feet.

To improve the S/N ratio, dual frequency based harmonic tag is studied and reported comprehensively in this report. The report is organized as follows: 1) The soil medium is characterized to select the frequency and power of the transmitted signal; 2) The detailed tag design with tag circuit and antenna is provided in section 2; 3) The packaging of the tag with the pipe material is described in section 3; 4) The on-tag sensing mechanism is described in section 4.

1. Medium and Power Budget Estimation

Before designing the RF tag, the propagation medium should be characterized for the choice of optimum frequency. Hence, first the soil medium characterization is necessary. Next important part is the power budget analysis of the whole system based on the dielectric properties obtained from the soil characterization. The transmission power requirement and antenna design would be obtained from the power budget analysis.

1.1. Soil characterization

The material properties of the soil would decide the amount of power would reach at the tag for underground detection. Hence, it is important to know the material parameters of soil at different frequency and moisture content. In general, as most of the soil is non-magnetic in nature, only dielectric properties of the soil are measured. In this report, the measured results of relative permittivity for typical Michigan soil are shown. Finally, the power budget analysis was performed using the measured dielectric constant.

The sample soil was collected from the backyard of Michigan State University and measured in a coaxial system as shown in Fig. 1.1. EM2107 coaxial adapter was used to provide a transition from a standard N-type connection to a 51Ω coaxial fixture, which can support TEM mode (no higher order modes) until 1.785 GHz in air medium. The coaxial fixture is capable of S-parameters measurement up to 1 GHz in air medium due to de-embedding constraint. A 3D-printed sample holder was used to place the soil in the coaxial fixture cavity as shown in Fig. 1.2. Once the sample was inserted, the S-parameters are measured using a network analyzer from 10 MHz to 800 MHz. The coaxial adapter effect was de-embedded using TRL (thru-reflect-line) calibration. After the de-embedding, S-parameters of the sample soil was obtained and Nicholson and Ross algorithm was used to measure the dielectric property of soil. To validate the result, an 11.8 cm long calibration fixture of Plexiglas was measured and compared to the reported data in literature. As expected, the real permittivity is around 2.6 and the imaginary permittivity is close to zero.

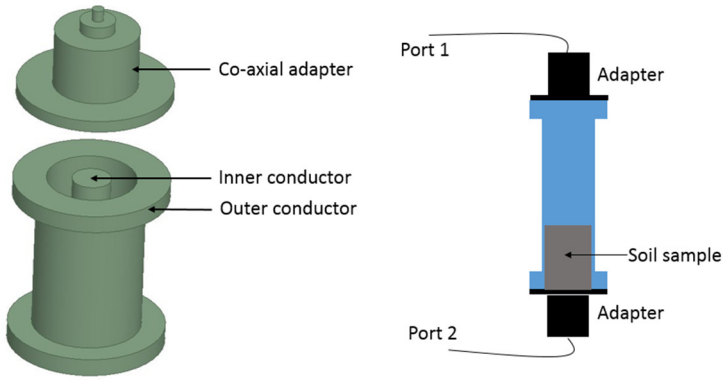

Fig. 1.1. The Coaxial Cable Setup for soil characterization.

Fig. 1.2. Measurement Setup and Sample Holder.

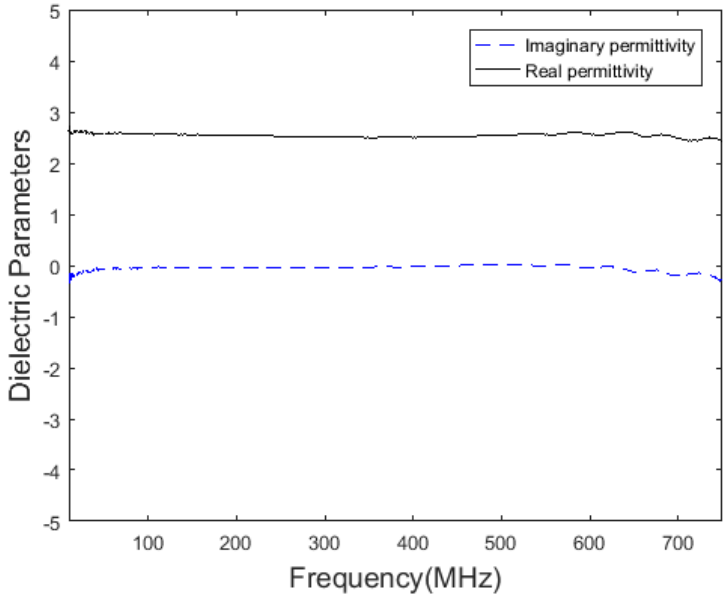

Fig. 1.3. Extracted value of Real and Imaginary permittivity of Plexiglas.

Once the measurement procedure was validated, the data is presented for the Michigan soil at different volumetric moisture content in Fig. 1.4 and 1.5. From the results, it can be observed that the real permittivity (ε_r) increases with higher moisture content as water has high dielectric constant compared to soil. Also, the soil becomes more lossy with increase in moisture content.

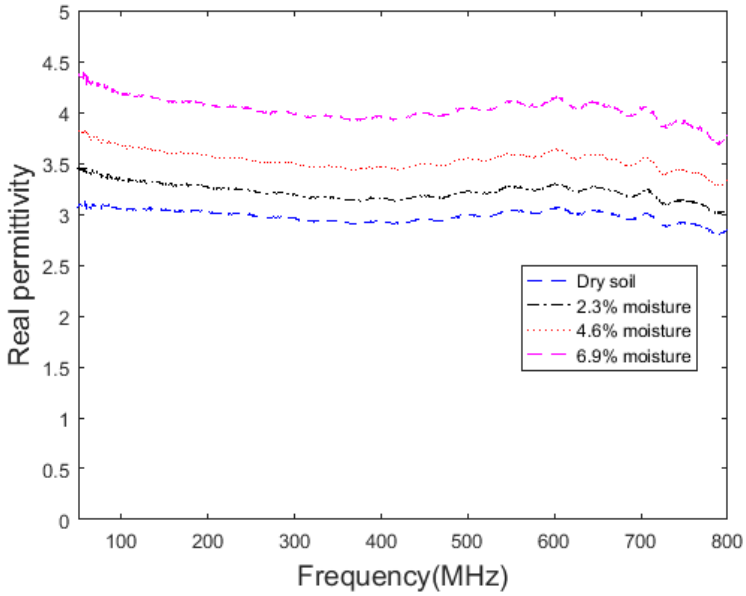

Fig. 1.4. Extracted values of Real permittivity of soil at a) Dry Conditions, b) 2.3% Volumetric Moisture Content, c) 4.6% Volumetric Moisture Content.

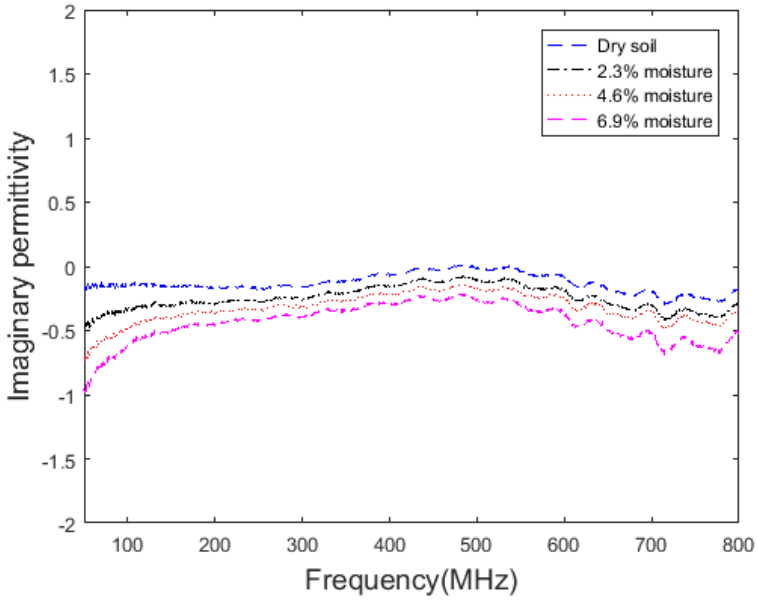

Fig. 1.5. Extracted values of imaginary permittivity of soil at a) Dry Conditions, b) 2.3% Volumetric Moisture Content, c) 4.6% Volumetric Moisture Content.

1.2. Power Budget Analysis

The detection of the buried harmonic tag is subject to a minimum power transmitted by the transmitting antenna, diode doubler efficiency and the minimum detectable SNR level at the receiver antenna. The signal goes through multiple environments such as air, soil and each environment includes multiple losses from different sources. The power budget estimation is a useful tool to pre-estimate the received power level

provided a certain power level is transmitted. Fig 1.6 shows the radio link between the developed tag and transmitter receiver antennas passing through different environments.

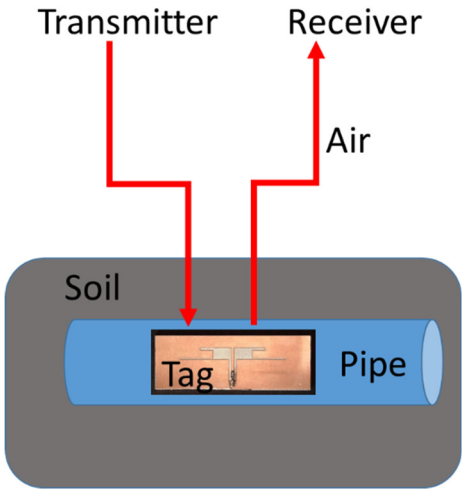

Fig 1.6. Radio link between the developed harmonic tag and the transmitter/receiver antennas.

The different losses in the entire system can be categorized as 1) Power Loss in Transmitter and Receiver, 2) Propagation loss in air, 3) Propagation loss in soil, 4) Losses at the air-soil interface and 5) Conversion losses in the harmonic tag. The Friis equation can be used to estimate the Received power at the tag (P_r) using the transmitted power (P_t) transmitter antenna gain (G_t) and the receiver antenna gain (G_r) as in equation (1.1). The received power at the tag can be expressed as:

$$P_r = P_{ta}\frac{G_t G_r \lambda}{)a} \tag{1.1}$$

where R is the distance between the transmitter and the receiver antenna and λ is the wavelength in the medium. The equation is valid if the medium between the tag and the transceiver is free space. However, due to diffraction, reflection and scattering in the air and soil medium, the far field received power is not always inversely proportional to square of the distance (R^2). The received power $P_r(d)$ at a distance d with path loss exponent γ can be expressed as in (1.2):

$$P_{ra}d) = P_{ra}d_0)\left(\frac{d_0}{da}\right)^{\gamma}a \tag{1.2}$$

where $Pr(d_0)$ is the power received at reference point d_0. The value of γ is 2 in free space. It varies from 1.6 to 5 depending on indoor (line of sight) or outdoor environment and also the medium of wave propagation. In this report, γ_s represents the path loss exponent in soil and γ_a represents the path loss exponent in air. The total path loss (PL) for air medium height of d_a and soil medium depth of ds for a reference medium height d_{0a} in air and medium depth d_{0s} in soil can be represented as followed

$$PL = \gamma_a * 10log_{10}\left(\frac{da}{d_{0a}}\right) + \gamma_s * 10log_{10}\left(\frac{d_s}{d_{0sa}}\right)a \tag{1.3}$$

Other than the individual losses in air and soil medium, there is also a reflection at the air-soil interface. And conversion efficiency losses of the harmonic tag. For reflection co-efficient Γ, tag efficiency ε and cable loss (*CL)* the total loss (*TL*) can be calculated as:

$$TL = PL - 20log_{10a}|\Gamma|) - 10log_{10a}1 - |\varepsilon|) + CLa \quad (1.4)$$

$$|\Gamma| = \left|\frac{\sqrt{\varepsilon_r}-1}{\sqrt{\varepsilon_r}+1}\right|a \quad (1.5)$$

Experiments were performed to determine the γ_a and γ_s using the harmonic tag as obtained from the soil characterization. Received power at different heights were measured to determine y_a for fixed d_{0a} =1 feet as shown in Fig 1.7. Since the incoming signal to the harmonic tag and the outgoing signal from the harmonic tag are at two different frequencies, the loss co-efficient was measured individually at 2.5 GHz and 5 GHz. The average value of the measured loss co-efficient in air at 2.5 GHz and 5 GHz are 1.25 and 1.61, respectively.

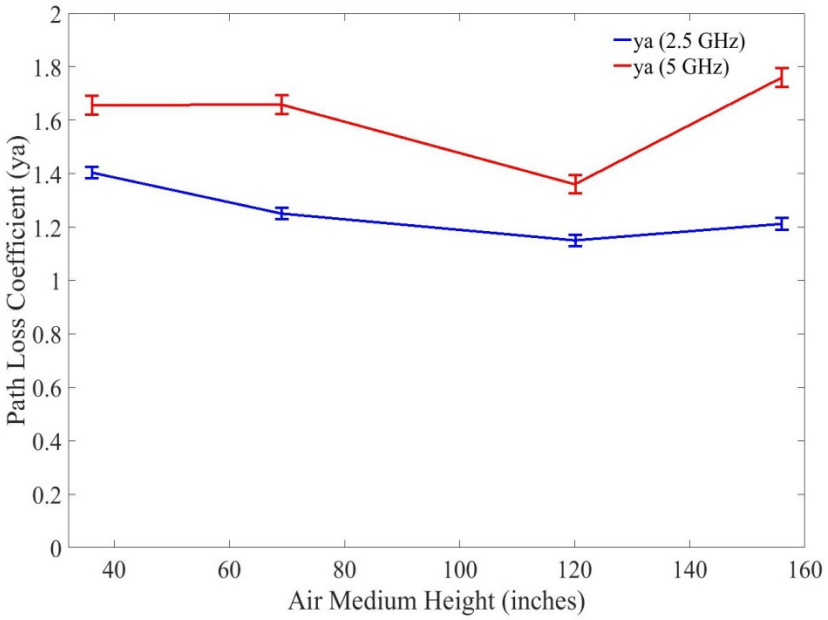

Fig 1.7. Measured path loss co-efficient in air for fundamental and second harmonic frequency.

However, as soil is a lossy medium, the power budget analysis would not be simple as shown in (1.1)-(1.5). The above analysis is valid for only in the air medium. A correction should be done in (1.1)-(1.5) for the proper power budget estimation within soil. Similar concept was used and extended for path loss model in soil medium. The Friis formula of received power at a distance d in any lossy dielectric medium is expressed as in (1.6). The loss factor (α) is given in (1.7) and the wavelength (λ_s) is to be calculated from (1.8) where $\lambda_s=2\pi/\beta$. The complex relative permittivity of the non-magnetic dielectric is given by (ε'-jε'').

$$P_r = P_t \frac{G_t G_r \lambda_s^{\ 2}}{(4\pi d)^2} e^{-2\alpha d} \tag{1.6}$$

$$\alpha = \omega \sqrt{\frac{\mu\varepsilon'}{2}} \left(\sqrt{1 + \left(\frac{\varepsilon''}{\varepsilon'} \right)^2} - 1 \right)^{0.5} \tag{1.7}$$

$$\beta = \omega \sqrt{\frac{\mu\varepsilon'}{2}} \left(\sqrt{1 + \left(\frac{\varepsilon''}{\varepsilon'} \right)^2} + 1 \right)^{0.5} \tag{1.8}$$

After the dielectric properties of soil were determined, the power budget model is developed based on the extracted value. The extracted parameters are provided in table below for different frequencies. Path loss due to attenuation is shown in Fig. 1.8 for different moisture content in soil sample. With higher moisture content in soil medium, the power loss increases. Also, it can be verified that the soil becomes much lossy at higher frequency. Hence, operation at high frequency is not suitable for underground communication.

Table 1.1. Dielectric properties used for power budget analysis

Frequency (MHz)	ε_r' (Dry)	ε_r'' (Dry)	ε_r' (2.3% moisture)	ε_r'' (2.3% moisture)	ε_r' (4.6% moisture)	ε_r'' (4.6% moisture)	ε_r' (6.9% moisture)	ε_r'' (6.9% moisture)
200	3.02	.162	3.27	.282	3.57	.363	4.07	.453
400	2.92	.058	3.15	.147	3.45	.215	3.95	.283
600	3.06	.095	3.29	.194	3.63	.261	4.14	.377
800	2.85	.178	3.07	.299	3.34	.349	3.78	.526

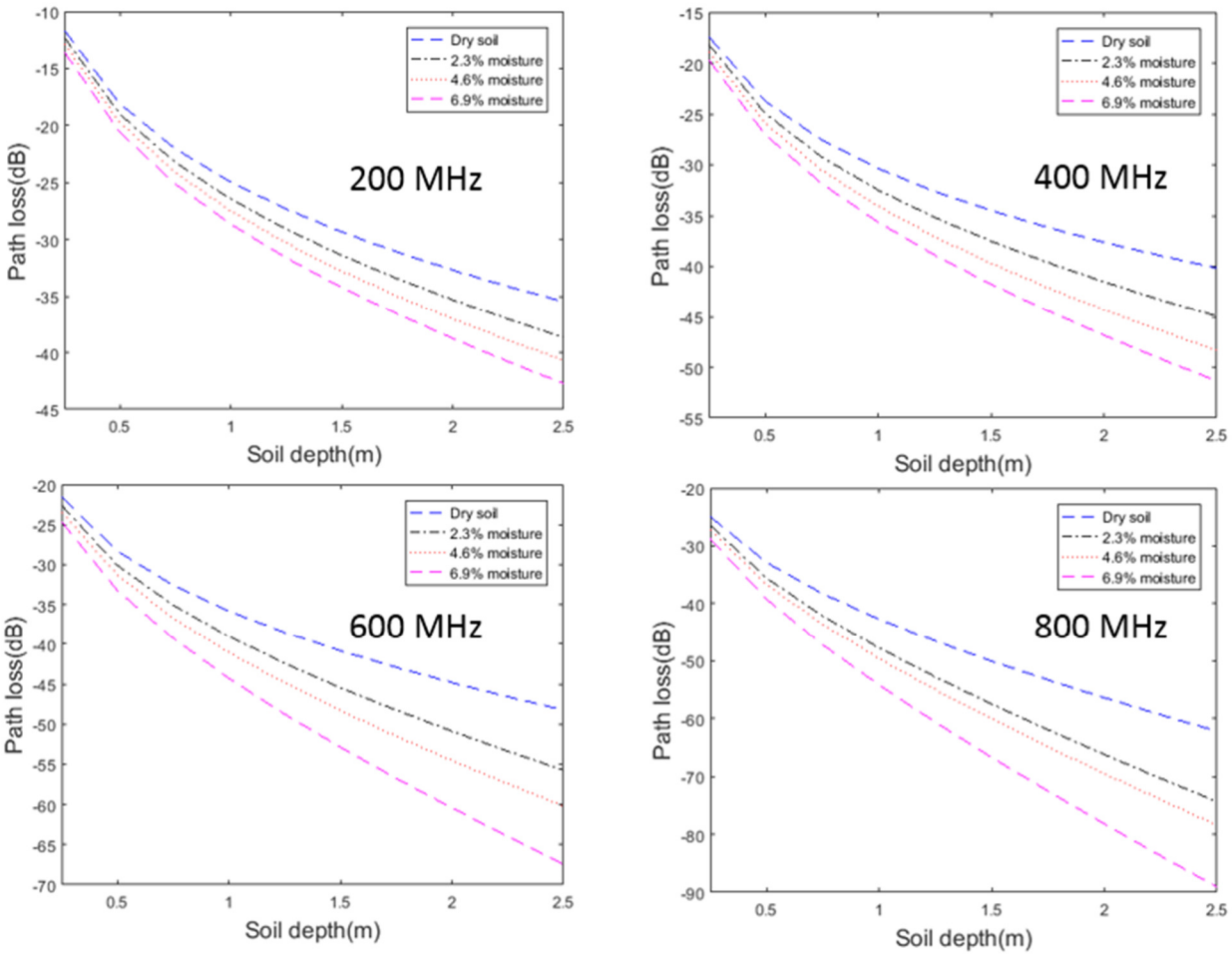

Fig. 1.8. Path loss in dB at different soil depth for four different frequencies of a) 200 MHz, b) 400 MHz, c) 600 MHz and d) 800 MHz.

2. Design and Development of Harmonic RF Tag

Different kind of harmonic RF tags were designed and fabricated. The main component of a harmonic tag is 1) an antenna and 2) a harmonic generator circuit. A nonlinear element is required for harmonic generation. Diodes were used for the harmonic generation as they have relatively high cutoff frequency and low current consumption. Primarily varactor and schottky diodes were studied and the efficient one was selected based on the underground application. The antenna used for most of the designs was a dipole kind of antenna for their good polarization. Different polarization is required to detect the pipe orientation. Hence, a linearly polarized antenna was selected based on this application.

2.1 Schottky diode based harmonic tag

Harmonic frequency doubler sensor concept is an extension of the simple dipole antenna. The key advantage of this harmonic sensor is the elimination of filters and reducing clutter. The first harmonic design consisted of a schottky diode integrated with two bow tie antennas. The receiver antenna is designed for fundamental frequency (2.5 GHz) and the transmitter antenna for the first harmonic (5 GHz). The system receives the signal at fundamental frequency and reradiates back to the receiver at the first harmonic. The analysis of signal at first harmonic helps identify the tagged infrastructure. Through time gating it can also allow for precise location in depth.

For the first experiment, a simple bow tie antenna was designed and simulated using High Frequency Structural Simulator (HFSS) operating at 2.5 GHz and 5 GHz. They were coupled together using a zero bias diode for frequency doubling. For the measurement two Vivaldi antennas were used to interrogate the harmonic tag. One antenna acts as the transmitter and the other as the receiver.

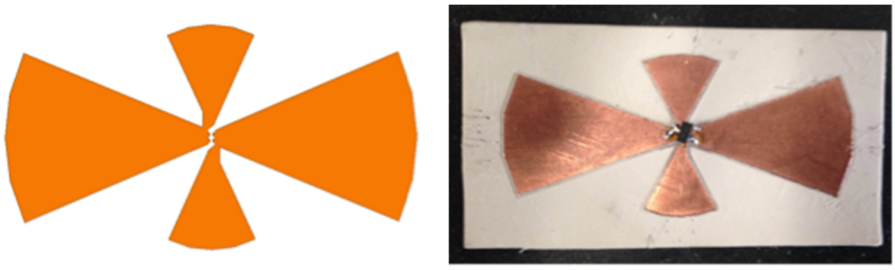

Fig. 2.1. First tag design consists of two bow-tie antennas coupled to a non-linear device.

The distance/power relationship and power/frequency relationship between the transmitter, receiver and sensor were studied and analyzed for the above tag design. In the first set of experiments, distance between the Tx/Rx and sensor was fixed as 7 inches and power radiated from the harmonic doubler was detected using spectrum analyzer. In the second set of experiments, the frequency was fixed and the performance of the system was studied by varying the distance between the transmitter/receiver unit and the harmonic tag. These first results show that the tag can be designed for desired operating frequency and can be used in clutter environment. This tag can be used a reference to compare future results from new tag designs and interrogation setup.

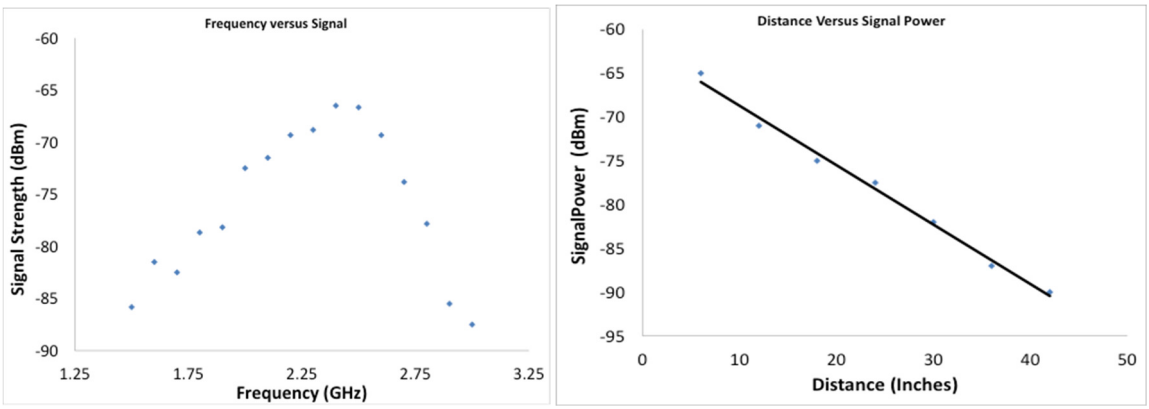

Fig. 2.2. Left: Measured frequency response of the tag, Right: Measured returned signal as a function of distance between the interrogator and the tag.

Next the use of passive harmonic tags (transponder) as markers are demonstrated for buried plastic pipes. The schottky diode based tag was improved using dual band slot dipole antennas. The tag converts an incoming 2.5 GHz frequency to a 5GHz output frequency. The antenna was fabricated on 1.52 mm thick substrate of dielectric constant 3. The fabricated tag was embedded in a plastic casing which represent wall of a plastic pipe as shown below. The casing was 3D printed using polylactic acid (PLA) dielectric material. Two harmonic tag designs based on double slot antenna are presented here: one embedded tag with a metal back reflector and the other without the metal backing.

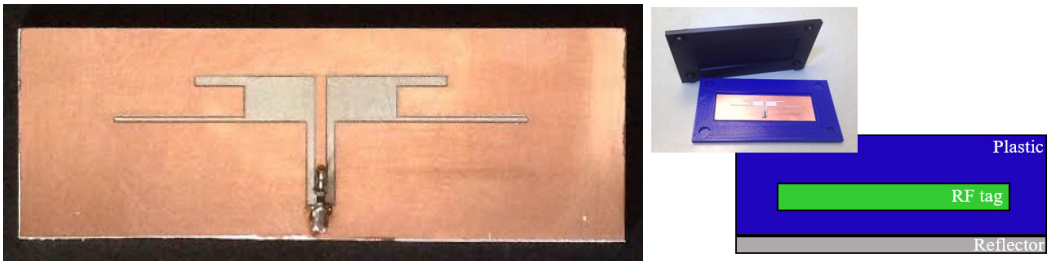

Fig. 2.3. Left: photograph of the tag placed in 3D printed plastic casing before bonding. Right: cross sectional view of the embedded tag with a metal reflector on the back.

Next, six different set of experiments were carried out to demonstrate the functionality of the developed schottky diode based harmonic tag. The first experiment is to verify the frequencies of operation of both the designs (with and without back reflector). Both of the tags works at 2.5 GHz and 5 GHz range as shown. In this experimental setup, the antenna performance is measured on a vector network analyzer (VNA) by directly connecting the antennas to a VNA using a coaxial cable. From the measured return loss (S_{11}) two operational bands can be observed. One is near 2.5 GHz and the other near 5 GHz. The operational band near 5 GHz was made wideband to accommodate fabrication tolerances. Following the return loss measurements, a diode was mounted in the structure for the generation of harmonics.

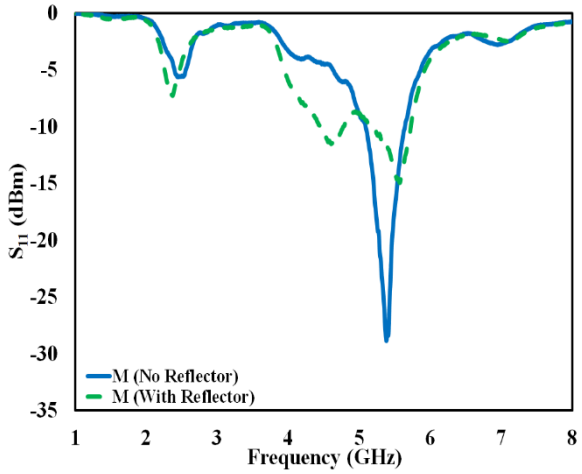

Fig. 2.4. Measured reflection coefficient of the RF tags (with and without a reflecting layer).

After mounting the diode, a second set of experiments were performed to find the optimal frequency of operation. Measurements on the tags were carried out as a function of input frequency (f_o with fixed power) versus output power at $2f_o$. The measured results are shown in Fig. 2.5 for both the tag designs. The results show that the addition of the reflector behind the tag provides better performance, which is largely due to improvement in the gain of the antennas. The performance of the tag with reflector has 10 - 30 dB higher output power than the tag without the reflector. In addition, the plot also shows the best optimal fundamental frequency is at 2.5 GHz.

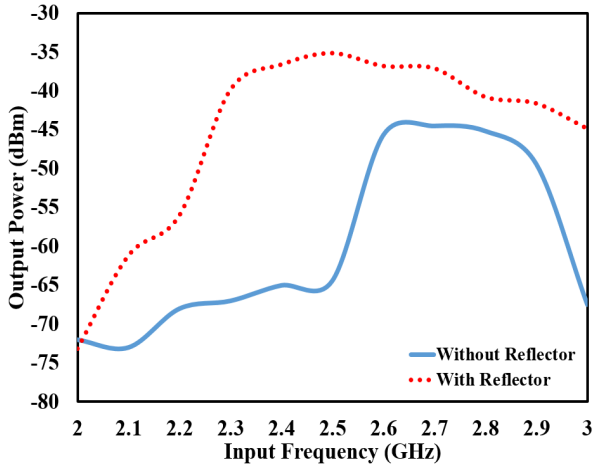

Fig. 2.5. Output power versus Input frequency for RF tag with and without reflector layer.

A third set of experiment was performed to demonstrate the long range interrogation of the tags in free space. Fig. 2.6 shows the measured return signal for the two tag designs as a function of interrogation distance. It shows that the received power decreases as a function of interrogation distance. The tag with the reflector provides better detection capability compared to the tag without the reflector due to better gain. The noise floor in the measurement is near -90 dBm. Thus, the measured results show that the signal to noise ratio (S/N) is high for these tag designs. In other words, the interrogation distance can be much longer than the measured range demonstrated here.

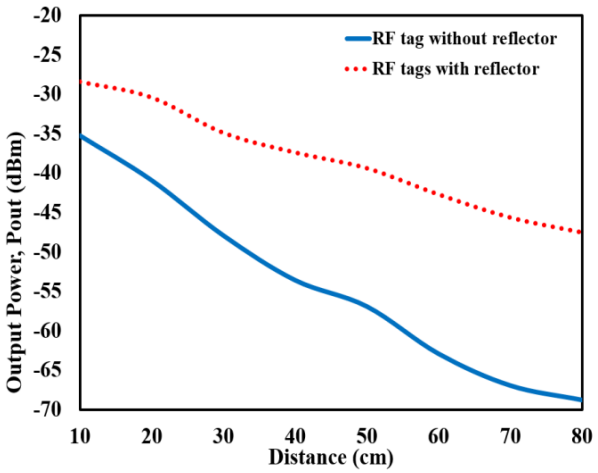

Fig. 2.6. Output Power versus Distance at 2.5 GHz fundamental frequency.

A fourth set of experiments were performed to demonstrate the functionality of the tag (with reflector) when buried under layers of wet soil (~ 10% moisture content). Fig. 2.7 shows the experimental setup. An RF absorber is placed on the backside to absorb stray signals and minimize reflected signal from the cement ground floor. The soil used consists of sand, clay, rock and other organic material that are naturally found in the backyard in Michigan, USA. In the measurements, the thickness of the soil layers on top of the tag was increased and the return signal was measured as a function of soil depth. Fig. 2.7 also shows the measured results; here the received signal from the tag decreases as a function of increase in thickness of the soil layer covering the tag. The data is presented here as a function of signal above the noise floor (-90dBm).

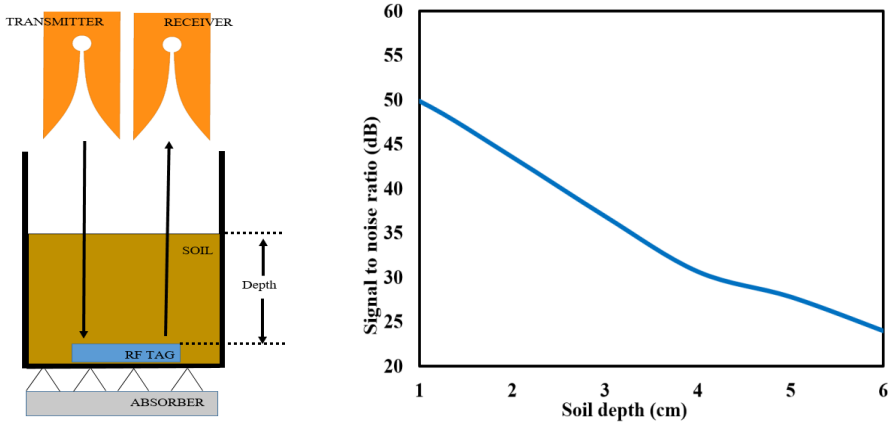

Fig. 2.7. On the left: Illustration of the experiment setup. On the right: Signal to noise ratio versus soil depth.

A fifth set of experiments were carried out to determine the direction of the buried pipes by using the polarization of the tag as a marker. The slot antennas are linearly polarized and the extinction ratio of the tag was measured while buried under soil. Fig. 2.8 shows the return signal as a function of angle between the transmitting (interrogator) Vivaldi antenna and the tag. The measured results show that polarization extinction ratio of the tag is >40 dB. This is sufficient for tagging the direction of underground buried pipes.

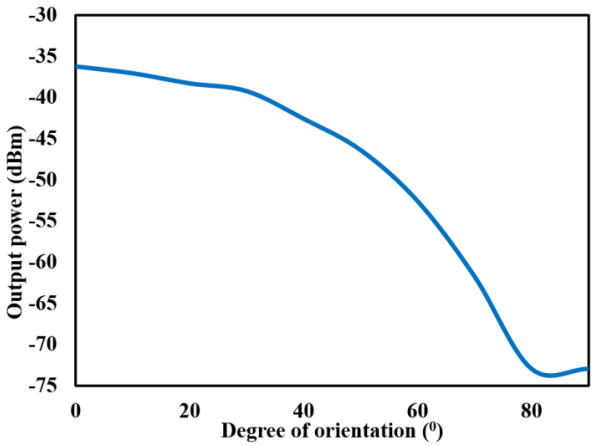

Fig. 2.8. Measured return signal as a function of polarization angle between the interrogator (transmit/receive) antennas and the tag antennas

The sixth sets of experiments demonstrate the ability to detect the tag at certain distance and angle. In this experiment, the tag was buried in the middle of a large sand box. The interrogator was moved across the sand box and the return signal was measured. An illustration of this experiment is shown in Fig. 2.9 Measurement was carried out at an increment distance of 3cm in the horizontal direction. The figure also shows the measured results as the interrogator crosses over the buried tag. It is plotted as a function of angle between the interrogator and the tag. Signal strength increases as the interrogator moves nearer to the tag or as the interrogation angle decreases. Maximum signal is when the interrogator is right above the tag. This approach coupled with time-gating of signal can be used to determine the precise location of the tag.

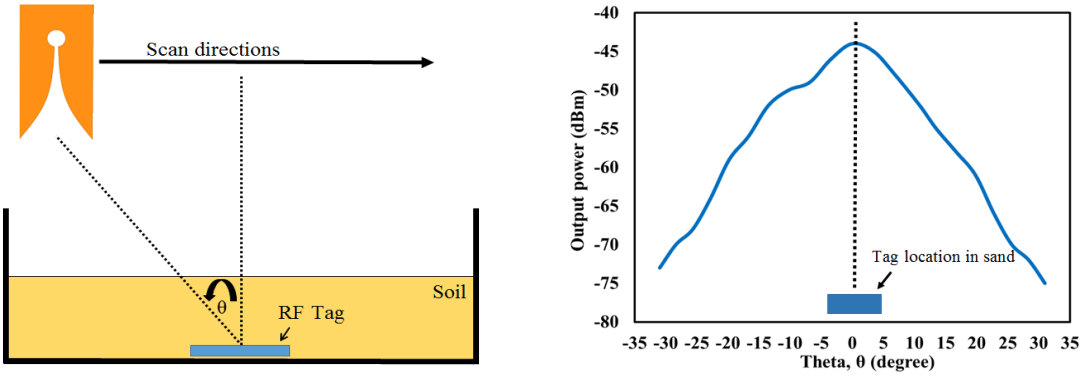

Fig. 2.9. Left: Illustration of the experiment of locating the RF tag embedded in plastic under buried sand. It was interrogated from a height of 50 cm. Right: Position versus return power from a buried antenna (under 3 cm thick sand).

Further modifications were performed on double slot antenna design for higher efficiency. The improved version of the tag is shown in Fig 2.10. Here, the antenna designs were optimized to achieve better impedance matching with the active element.

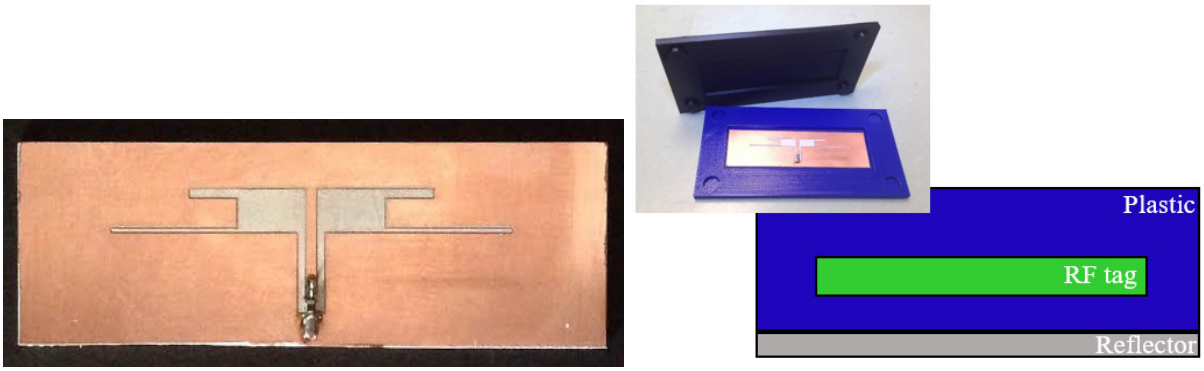

Fig. 2.10. Left: photograph of the tag placed in 3D printed plastic casing before encasing in plastic. Right: cross sectional view of the embedded tag with a metal reflector on the back of the plastic casing.

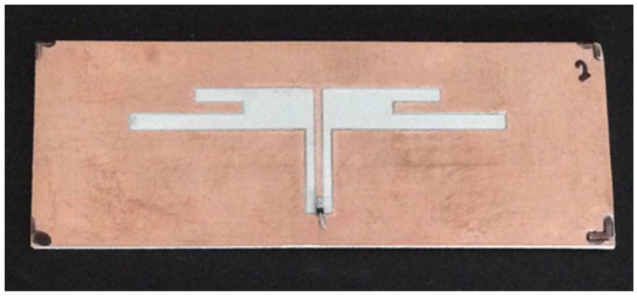

Fig. 2.11. Improved version of the tag.

In the following sections, four sets of experiments were carried out to demonstrate the functionality of the improved tag. In the first set of experiments, measurements on the tags with and without reflector were carried out as a function of input frequency (f_o) at fixed power versus return power at $2f_o$. The comparison of the measured results is shown in Fig. 2.12 for previous and improved tag design. The bandwidth of the new tag is more than the old design, and also the performance of the new tag has 2-5 dB higher output power than the old version.

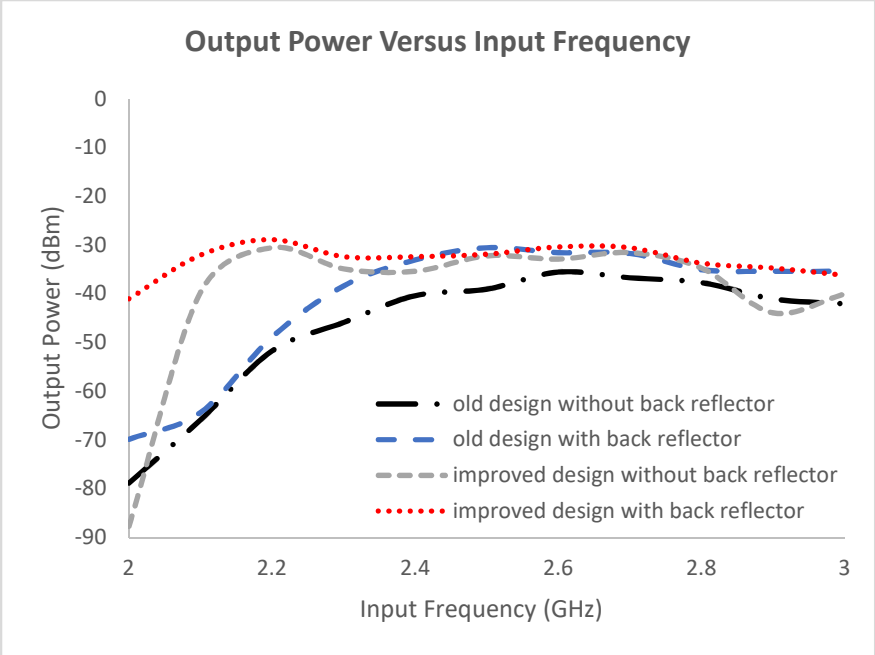

Fig. 2.12. Comparison of old and improved version of tags: return power (at $2f_o$) versus input frequency for fixed input power.

A second set of experiment was carried out to determine the direction of the buried pipes by using the polarization of the tag as a marker. Fig. 2.13 shows the comparison of the return signal as a function of angle between the transmitting (interrogator) Vivaldi antenna and the improved tag and the old tag design. The results show that the new tag has good extinction ratio, sufficient enough for using polarization as a marker for tagging the direction of the buried pipe.

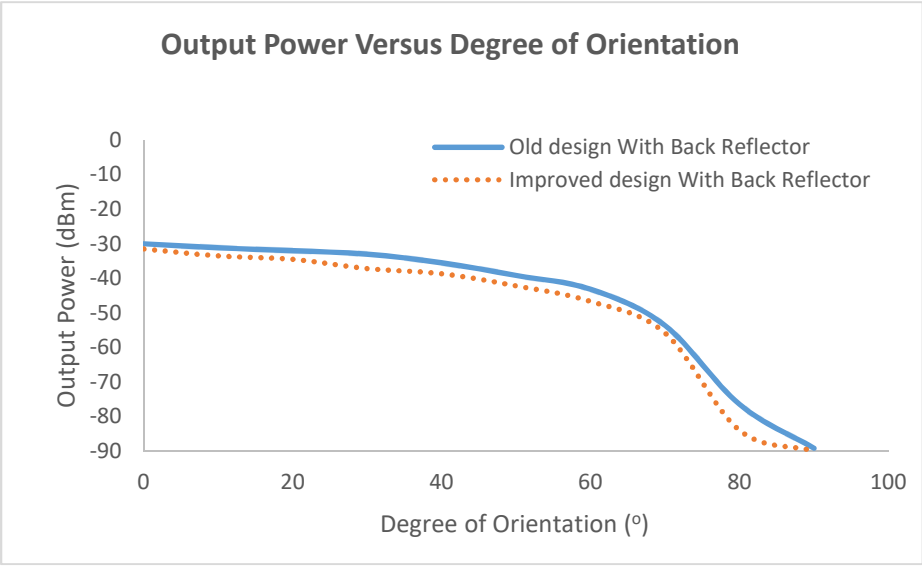

Fig. 2.13. Measured return signal as a function of polarization angle between interrogator and the tag.

A third experiment was performed to demonstrate the long range interrogation of the tags in free space. Fig. 2.14 shows the measured return signal for the two tag designs as a function of interrogation distance. It shows that the received power decreases as a function of interrogation distance as expected due to the square power law. The modified tag has better return signal as a function of distance in comparison to the old design as shown in Fig. 2.14.

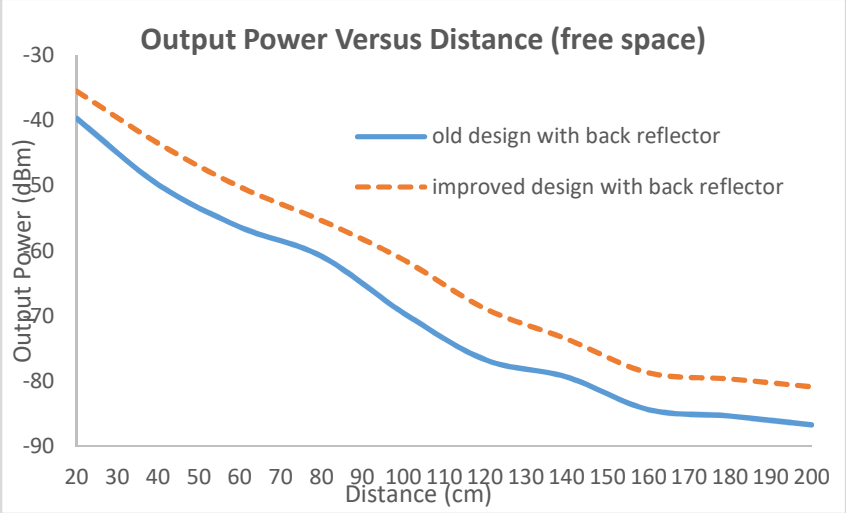

Fig. 2.14. Output Power versus Distance at 2.5 GHz fundamental frequency for old and improved designs.

A fourth experiment was executed to demonstrate the functionality of the tag (with reflector) when buried under layers of soil. The tag was placed in a large plastic container filled with soil. An RF absorber is placed on the backside of the tag to absorb stray signals and minimize reflected signal from the back side of the plastic container and the cement ground floor. Fig. 2.15 shows the comparison of output power versus soil depth (buried depth of the tag) for both the designs. It can be seen that the improved design has higher output power than the old design as a function of soil depth by approximately 15 dB. This shows that the tag can be placed at a significant depth while getting sufficient return signal (good signal to noise of the return signal).

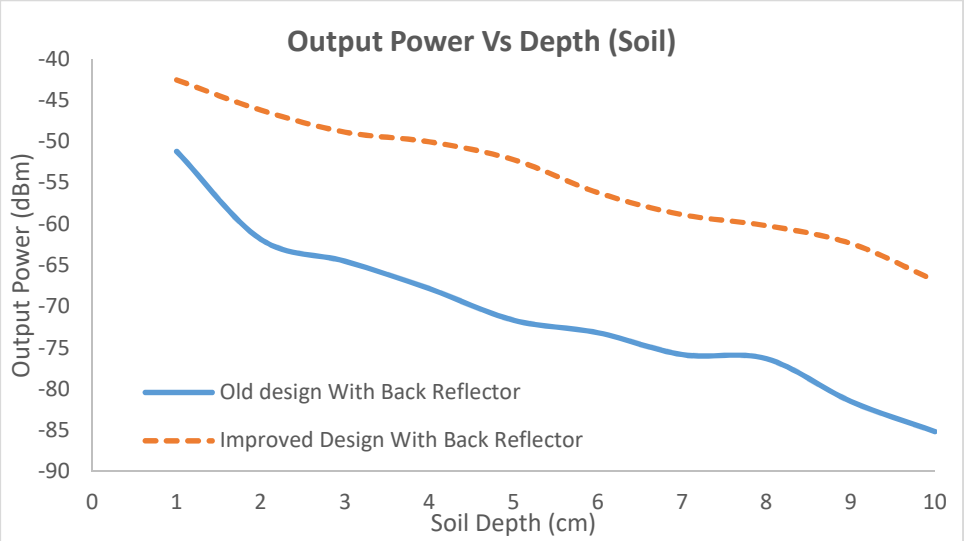

Fig. 2.15. Output Power versus soil depth for old and improved designs.

2.2 Comparative Study of Varactor and Schottky Diode Based Tags

It is well known that the path length loss in soil is significant, especially for wet soil. Thus, a buried tag with high conversion efficiency is desirable, especially at low input power. During this reporting period we examined a new tag design based of varactor diodes. The performance of this new tag is compared to our earlier design based on a Schottky dode. Three set of experiments were carried out and results are reported here: i) Direct measurement of harmonic signal generated from the two tag designs, ii) Antenna coupling between transmitter and the RF tag, iii) Complete return path signal measurement using antennas at both the transmitter and receiver ends. Simulations were also carried out for the two tag designs and these results are also presented. Overall, the goal of this design study is to design an efficient harmonic tag that operates at very low power (< -50dBm). This is necessary as the power received by the buried tag is expected to be very low due to large attenuation through the soil layer(s).

First, the direct measurements were carried out to compare in between the biased varactor and the schottky diodes, see Fig. 2.16(a). A directional coupler (10 dB) was used to couple in the power to the tags and to measure the harmonic return signal using a spectrum analyzer. Input power was generated at the fundamental frequency (f_0) and the power was measured at the coupled port of the directional coupler at the fundamental (f_0) and harmonic ($2f_0$) frequency. The generated harmonic power vs the actual absorbed power was plotted in Fig. 2.16(b). The varactor diode under a DC bias of 0.6 V lower than its threshold voltage (0.77V) performed better than the unbiased zero-bias schottky diode under low input power (<-12.5 dBm) was verified. Varactor diode based harmonic generator provides >20dB of return signal than the Schottky diode at low power. A varactor diode has low leakage current (< 1nA) and thus low DC power is dissipated. In the future a low-barrier or zero bias Varactor will be used to avoid DC biasing.

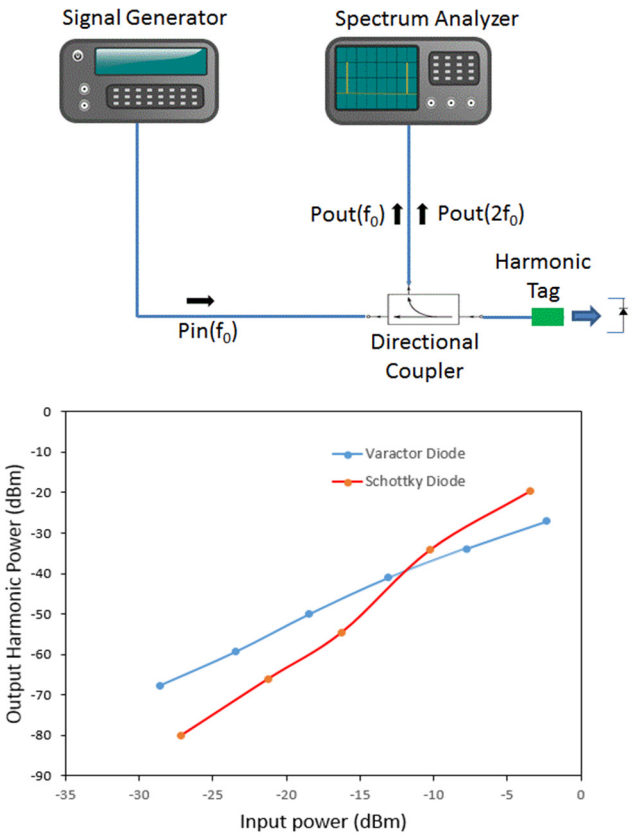

Fig. 2.16. (a) Measurement setup for the efficiency comparison of the diodes, (b) Output harmonic power comparison for the biased Varactor and Schottky diode with the measurement setup.

The harmonic tags were further optimized by impedance matching at operating frequency of 1.3 GHz to obtain the maximum harmonic power from the tag. Fig. 2.17 shows the measured results which shows improvement in Varactor diode based tag even at higher power levels, up to -5dB.

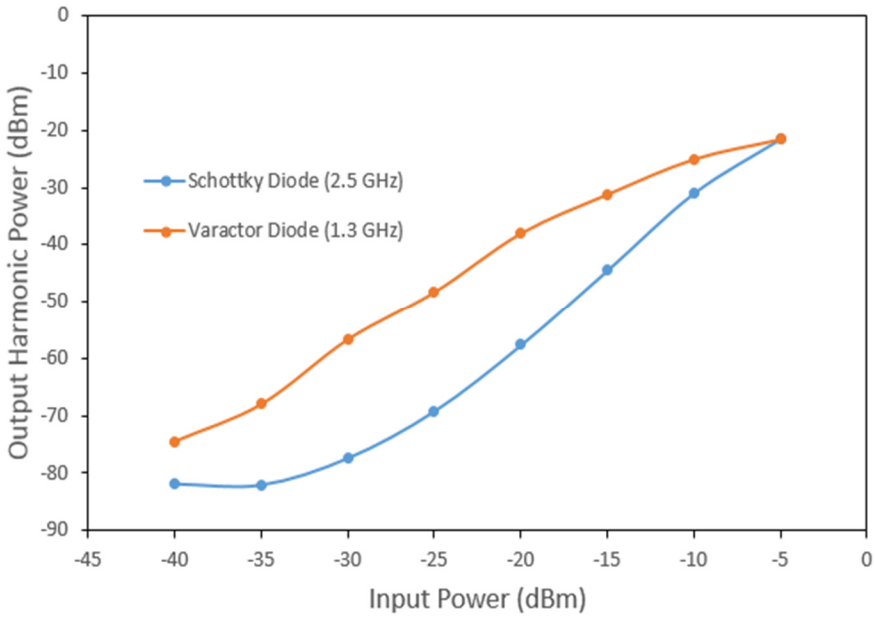

Fig. 2.17. Output harmonic power comparison for the biased Varactor and Schottky diode after impedance matching.

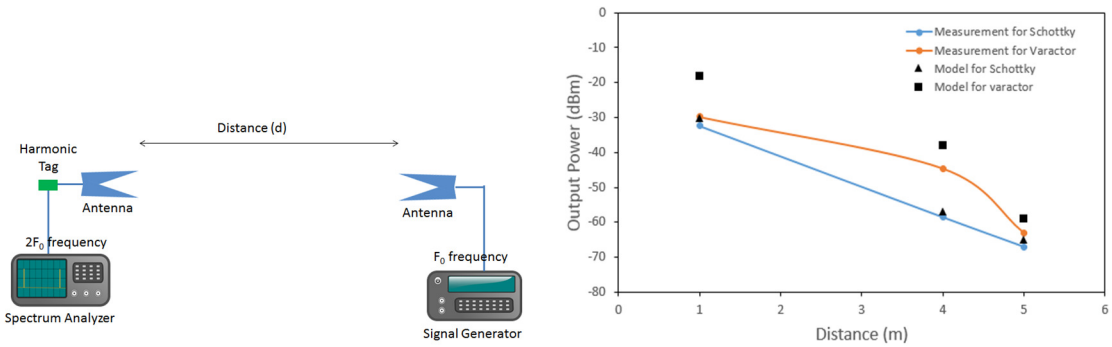

Fig. 2.18. (a) Experimental setup of the harmonic power received by the harmonic tag, (b) Power received at the signal analyzer for 1) Schottky diode with fundamental frequency at 2.5 GHz and 2) Varactor diode with fundamental frequency at 1.3 GHz.

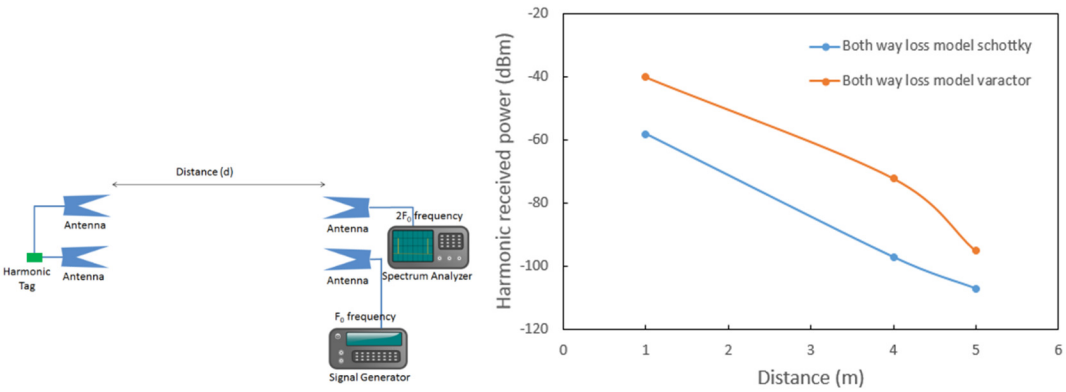

Fig. 2.19. (a) Extended 2-way model for the output received power considering all the air medium losses, (b) Model output received power for harmonic tag using Schottky and Varactor diode.

2.3 Antenna Miniaturization

As the operating frequency is lowered, antenna size becomes larger, which would make the harmonic RF tag bulky. Hence, it is required to design small size antenna with reasonable gain. Different planar and 3D antennas were simulated and measured applicable for the application.

2.3.1 Coil Antenna:

Coil antennas are popular for low frequency operation. A small coil antenna was designed, which is capable of operation along the radial direction. This orientation would be helpful for antenna realization on the pipe itself as shown in Fig. 2.20. The gain was measured using a VNA at a distance of 5 feet in between the two coils. From VNA measurement, the power loss in air medium was observed as -24 dB. The coil diameter is 17 cm with 8 turns. The region of antenna operation is from 436 MHz to 466 MHz.

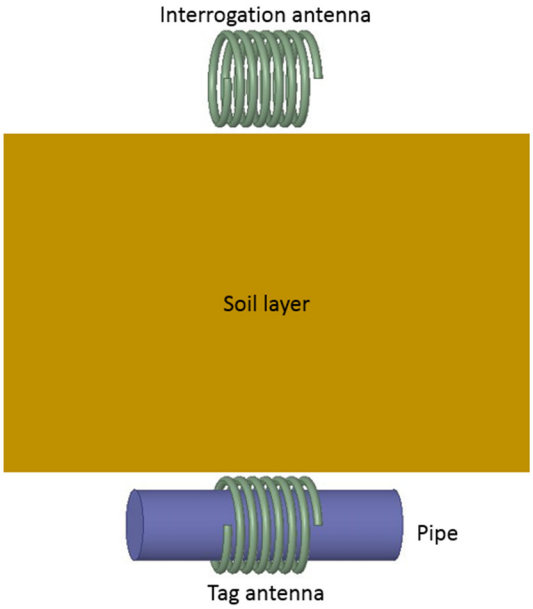

Fig. 2.20. Diagram of radially wrapped Coil Antenna.

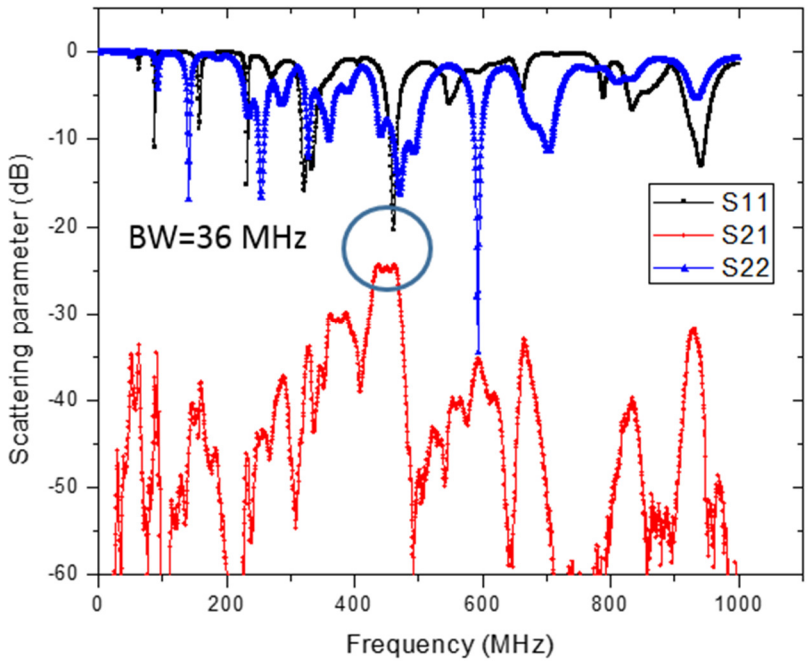

Fig. 2.21. Measured coil antenna response at 5 feet separation in air.

2.3.2 Meandered Dipole Antenna:

For low frequency operation, the antenna size gets large. Hence, it is a challenge to reduce the size of the antenna while maintaining a decent amount of gain. A dipole antenna can be designed in meandered fashion to reduce its size. The design and simulation results of the meandered dipole antenna is provided as follows:

A meandered dipole antenna was designed for 400 MHz on Rogers 4350B substrate. The maximum board size is (72mm*80mm), which is smaller compared to a conventional dipole antenna at same frequency. The total realized gain was plotted at 420 MHz. As expected, most of the power is transmitted along the z and y direction. For maximum power transmission, the input impedance of the antenna was matched to 50 Ω. A T-match was used at the feed point for the impedance matching.

In similar way the 800 MHz harmonic antenna was designed. Most of the power is radiated along the z and y direction. The size of the harmonic antenna is (40mm*80mm). A T-match and a load line were used to match the input impedance of the antenna to 50 Ω.

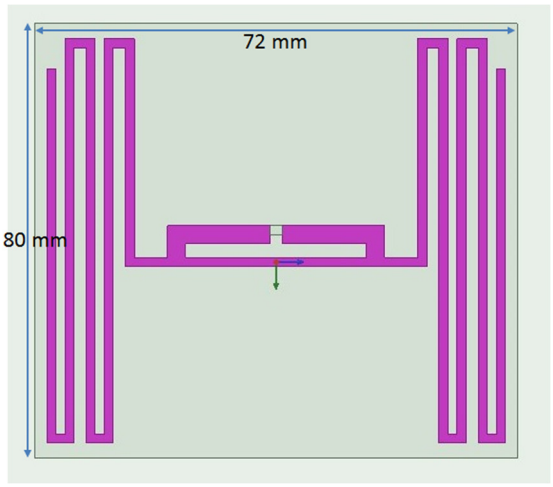

Fig. 2.22. The 400 MHz meandered dipole antenna on a Rogers 4350B board.

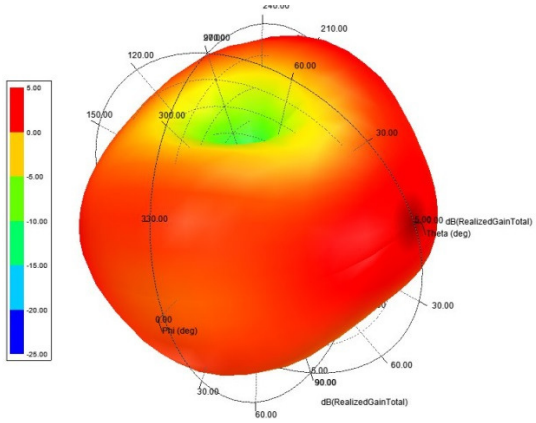

Fig. 2.23. Realized gain pattern of the 400 MHz antenna with maximum gain along y and z axis.

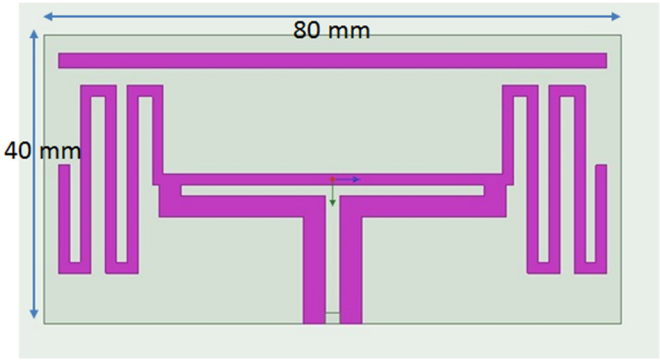

Fig. 2.24. The 400 MHz meandered dipole antenna on a Rogers 4350B board.

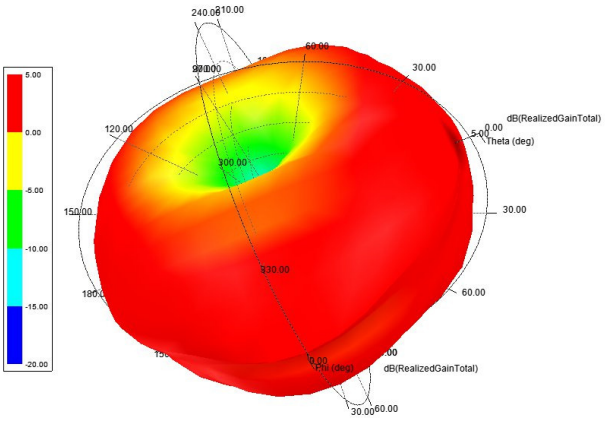

Fig. 2.25. Realized gain pattern of the 800 MHz antenna with maximum gain along y and z axis.

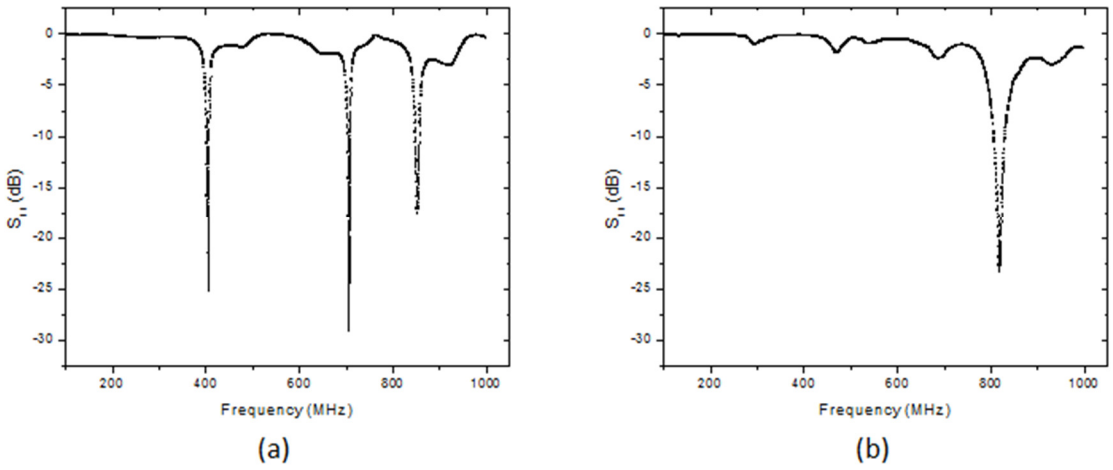

Fig. 2.26. Measured S_{11} for (a) 400 MHz antenna and (b) 800 MHz antenna.

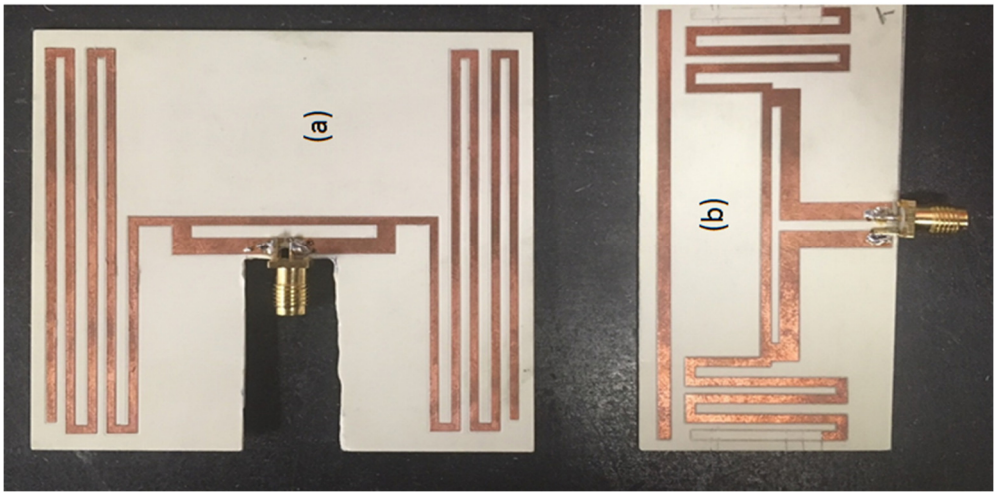

Fig. 2.27. The fabricated antennas (a) 400 MHz and (b) 800 MHz.

2.3.3 Wide band antennas:

From the soil analysis reported earlier, it was shown that the soil dielectric property varies with different frequency and moisture content. When the antenna is buried underground, the surrounding soil medium changes the resonance frequency and impedance of the antenna due to dielectric loading. Hence, a narrow-band frequency antenna would not be appropriate for underground communication. A wide-band antenna was designed for two aspects 1) Multi-frequency phase estimation and 2) Proper functioning due to resonance frequency shift. Two wide-band antennas for 430 MHz band and 860 MHz band were designed.

An 860 MHz bow-tie antenna was designed for wide band application. The schematic of the antenna is provided in Fig. 2.28.

Fig. 2.28. Bow-tie antenna of 1) Top plane and 2) Bottom plane (Board size 60cm*116cm).

The antenna was fabricated on top of a Roger's 4350 board with thickness of 1.52 mm. The reflection coefficient of the antenna was measured in a VNA and the result is shown in Fig. 2.29.

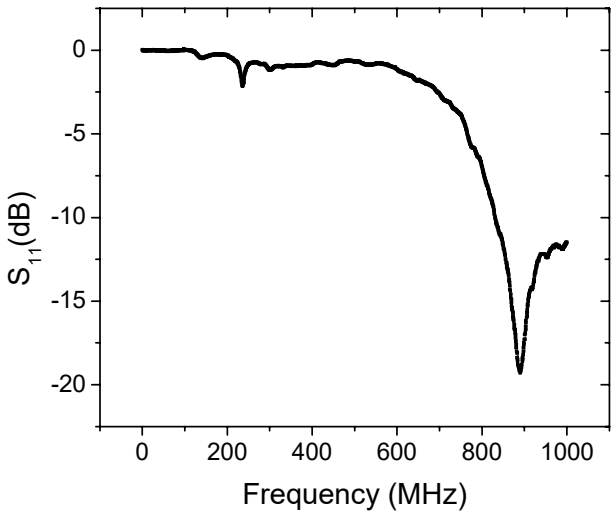

Fig. 2.29. Measured reflection co-efficient of the 860 MHz antenna (BW of 200 MHz).

Similarly for low frequency, a meandered bow-tie antenna was designed as shown in Fig. 2.30. The antenna size increases for low frequency operation. Meandered antennas are popular for their compact size. However, the bandwidth decreases due to meandering. The reflection co-efficient is plotted in Fig. 2.31 for the frequency band.

Fig. 2.30. Meandered bow-tie antenna of 1) Top plane and 2) Bottom plane (Board size 60cm*162cm).

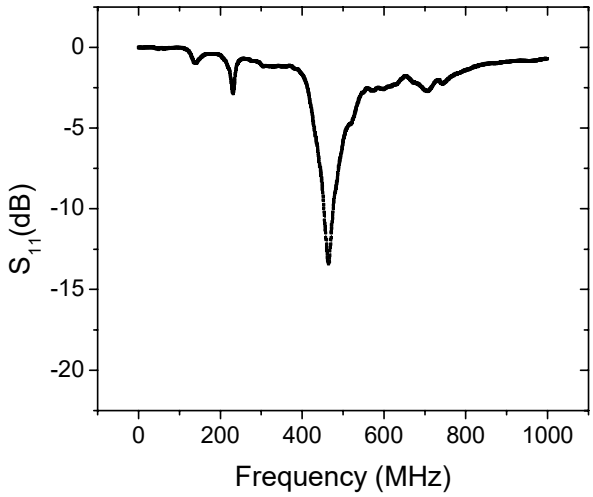

Fig. 2.31. Measured reflection co-efficient of the 430 MHz antenna (BW of 25 MHz).

The performance of the antenna changes with change in surrounding medium. The permittivity of the soil varies around 4 depending on the property and condition of soil (from very dry soil to saturated wet clay soil). The loss tangent of the soil also increases with increase in moisture content. The effect of soil on the antenna properties is simulated based on the data reported in soil characterization section. The dataset is provided in Table 1.

Table 2.1. Dielectric properties of soil

ε_r' (Dry)	ε_r'' (Dry)	ε_r' (2.3% moisture)	ε_r'' (2.3% moisture)	ε_r' (4.6% moisture)	ε_r'' (4.6% moisture)	ε_r' (6.9% moisture)	ε_r'' (6.9% moisture)
2.9625	0.12325	3.195	0.2305	3.4975	0.297	3.985	0.40975

The reflection co-efficient and the input impedance of the wide-band antenna were simulated for different permittivity of the soil as shown in Table 2.1. As expected, the resonance frequency decreased

with higher moisture content in soil. Simultaneously, the quality factor of the antenna response reduced with increased loss tangent.

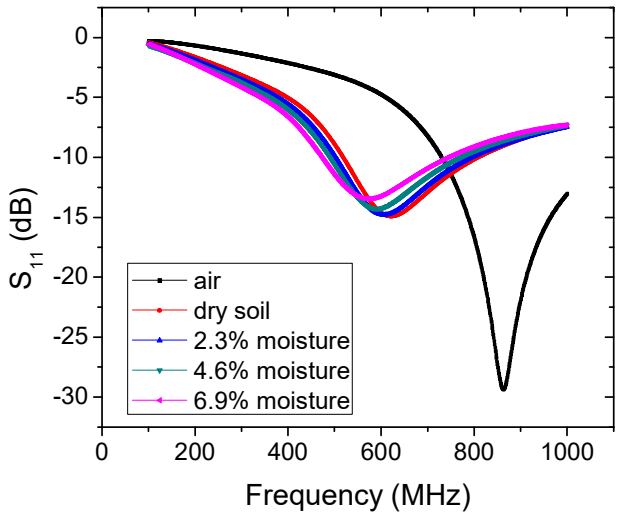

Fig. 2.32. Reflection coefficient change in air and soil with different moisture contents.

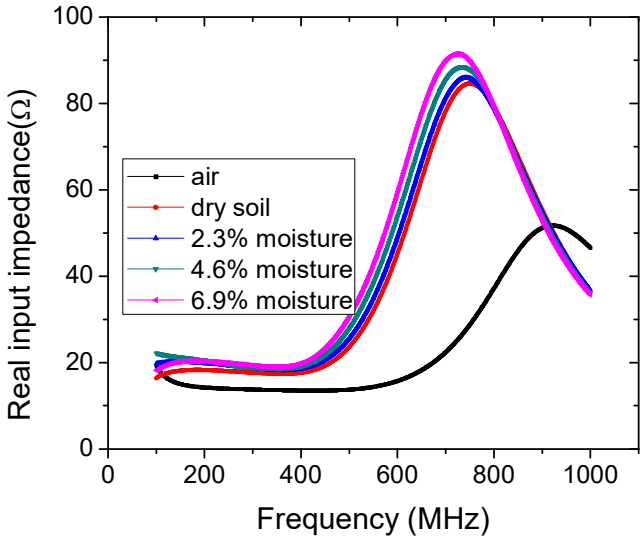

Fig. 2.33. Real input impedance change in air and soil with different moisture contents.

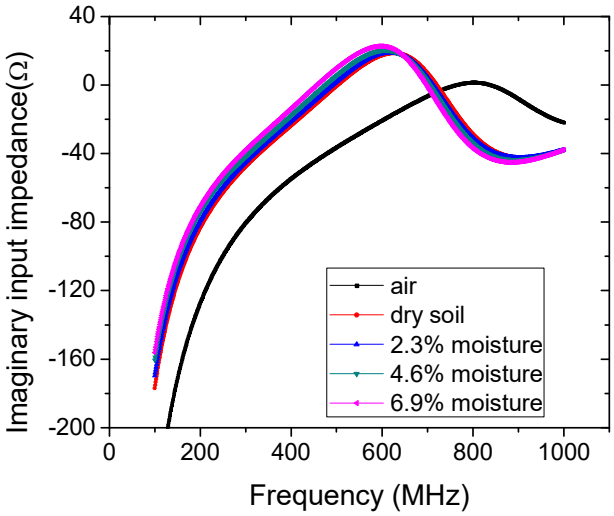

Fig. 2.34. Imaginary input impedance change in air and soil with different moisture contents.

2.4 Proposed Tag Circuit

The NLTL based harmonic generator circuit is presented as explained before. The harmonic generator consists of 1) A NLTL and 2) An energy harvesting Circuit. The design and performance of the NLTL was shown in previous report. The energy harvester performance would be demonstrated in detail here. The integrated performance of the Energy harvester along with the NLTL would be demonstrated finally. The energy is harvested by converting a part of RF input signal into DC power. Commonly rectifier circuits are used for the RF to DC conversion. However, the harvested voltage by a single diode is not enough to drive the DC circuit. Hence, multiple diodes were used in a Dickson charge pump configuration to drive the whole circuit. A 1.8 V DC voltage regulator was used to maintain the voltage at a fixed reference. The DC bias was used to create a 0.6 V reference suitable for driving the NLTL circuit. The schematic design of the circuit is shown in Fig.2.35 below.

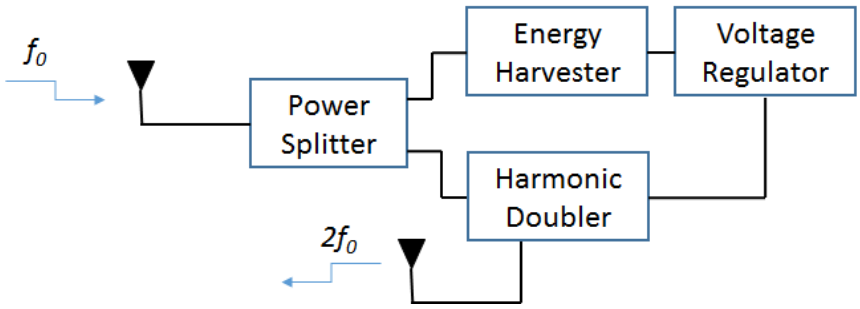

Fig. 2.35. Schematic of the harmonic doubler.

Once the circuit is designed, it is integrated on top of PCB. The photograph of different fabricated components is shown in Fig. 2.36. The power splitter divides the incoming signal into two different parts: 1) The first part is harvested in the Energy Harvester and DC bias is produced, 2) The second part is used

in the harmonic generator to produce the second harmonic signal. After different components of the tag circuit were designed, the complete tag performance was measured. Fundamental input signal was fed into the tag and the output harmonic power was measured.

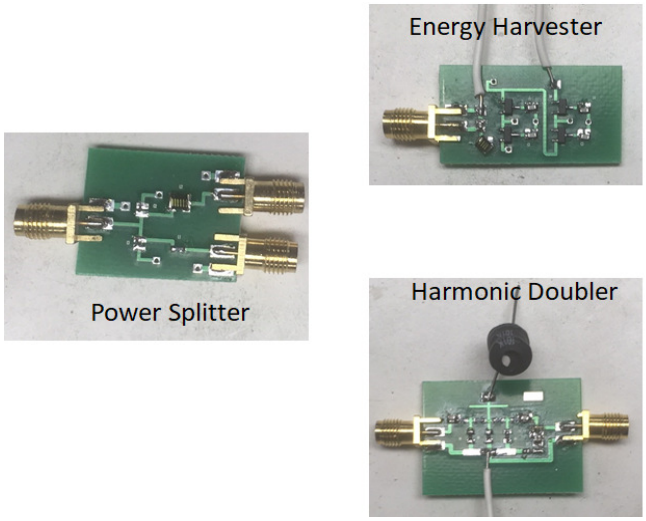

Fig. 2.36. Integration of different components of complete tag design.

The measurement result is presented in Fig. 2.37 for the complete tag circuit. The tag circuit performances well until the input power is -11 dBm without any external DC bias under direct probing. The efficiency falls below this input power primarily falls because the voltage regulator cannot regulate the required DC voltage level. An alternate energy source can be integrated with the design for better performance even at low input power of -20 dbm. The tag circuit is developed separate from the antenna, so that the antenna can be post integrated depending on applications with the pipe using a long range additive manufacturing process.

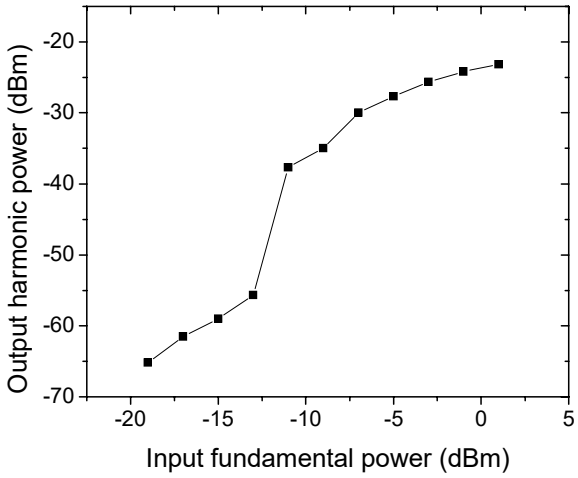

Fig. 2.37. Measured results of harmonic power for different input power at 440 MHz.

The Non-linear Transmission Line (NLTL) based harmonic complete tag with antenna was fabricated as proposed and described earlier. A discrete component NLTL based harmonic generator was proposed earlier with different components such as 1) A NLTL and 2) An energy harvesting Circuit individually for the underground application as shown in Fig. 2.36. All the different components are combined together with antennas to build the complete tag as shown in Fig. 2.38.

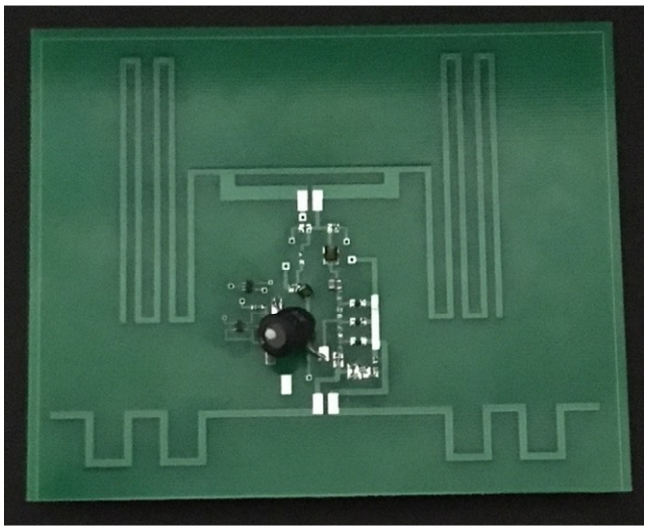

Fig. 2.38. The fabricated complete harmonic tag.

Once the tag was designed and fabricated the performance of the tag was analyzed by measuring the tag performance with different distance. As proposed in earlier report, similar instrument setup was used for harmonic power measurement as shown in Fig. 2.39.

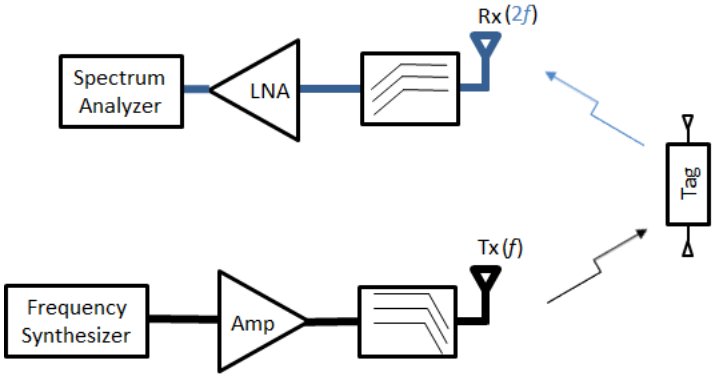

Fig. 2.39. The design of the reader circuit at the left half.

Before measuring the complete tag, first the performance of the NLTL based harmonic tag under external constant DC bias was evaluated. Same reader circuit as shown in Fig. 2.39 was used for this measurement. A constant frequency of 400 MHz was generated from a stable frequency synthesizer at at -5 dBm. A power amplifier was used to amplify the signal and finally +16 dBm of power was fed to the transmitter antenna after amplification. To reduce the harmonic power level transmitted by the 400 MHz antenna, a low pass filter was used, which provides the harmonic power level 60 dB below the fundamental

signal. As the transmitter and receiver antennas are linearly polarized, cross polarization orientation was used for receiving and transmitting antennas to reduce the harmonic power coupling and thus minimizing the noise level. After the reception of harmonic signal from the tag using the 800 MHz receiving antenna, the harmonic signal is passed through a high pass filter to remove the clutter signal created by the fundamental frequency. Once the harmonic signal is filtered out, it is amplified using LNA and finally the signal is captured in a Spectrum Analyzer.

The range of the interrogation depends upon the noise level of the received harmonic power level from the transmitter. Use of sharp roll-off low pass filter and antenna cross-polarization can increase the read range significantly.

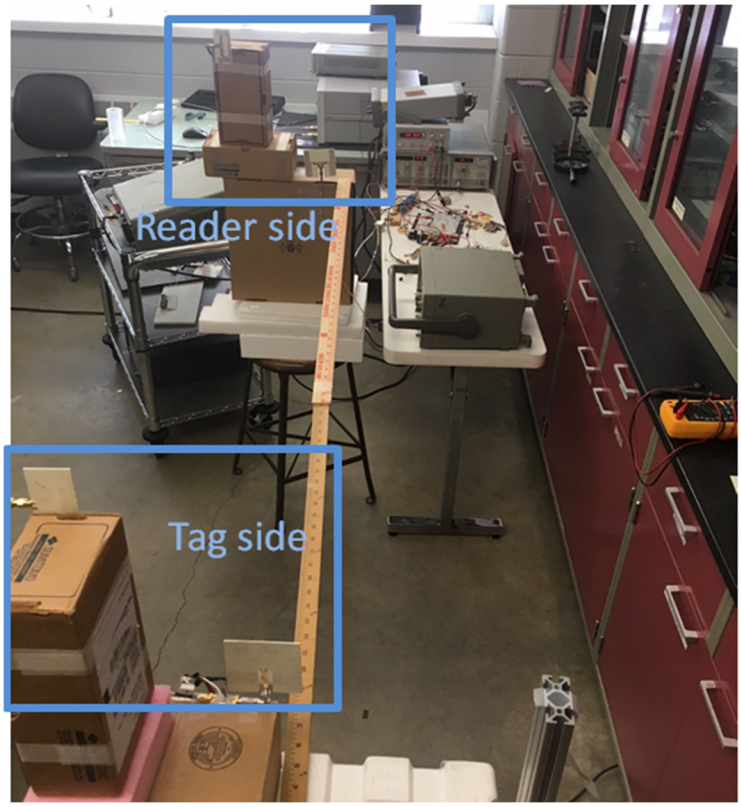

Fig. 2.40. Measurement setup of the system.

Table 2.2. Measured received power at different distance

Distance (inches)	Noise Level (dBm)	Received Power (dBm)
62	-31.5	-11.87
70	-32.37	-14.5
80	-29.5	-21.4
100	-32.2	-26.3

Once the NLTL only was verified with antenna under external bias, the complete tag as shown in Fig. 2.38 was measured. The tag harmonic power performance with varying distance is shown in Fig. 2.41, 30 dBm of power was transmitted at 433 MHz and the harmonic output power was measured at 866 MHz.

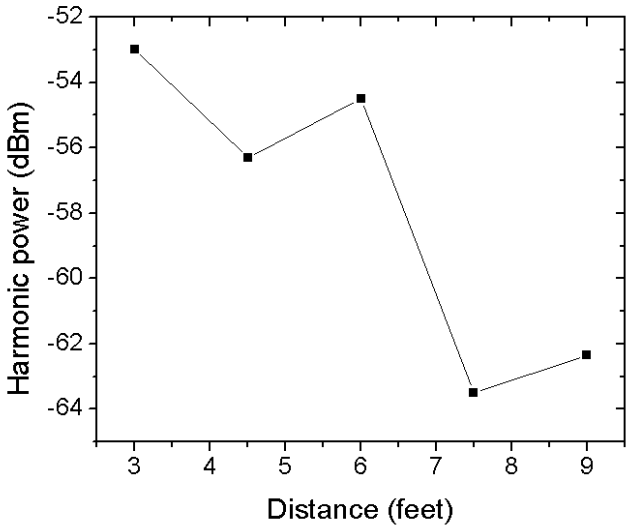

Fig. 2.41. Harmonic power profile of tag with distance.

Different type of harmonic generators such as 1) Schottky diode based harmonic generator and 2) Non-linear Transmission Line (NLTL) based harmonic generator were investigated. It was found and reported earlier that the Schottky diode based harmonic generator works better at comparatively high input power (> -5 dBm). For underground application, the received input power would be very low (< -10 dBm). Hence, Schottky diode based harmonic generators are not a good choice for underground application. A discrete component NLTL based harmonic generator was proposed earlier for the underground application. However, the NLTL needs a DC bias for effective harmonic generation. Hence, the harmonic generator requires an energy harvesting circuit, which can provide bias to the NLTL. Until last report no energy harvesting scheme was shown. A complete design of energy harvester and NLTL is proposed and shown for the final tag circuit design.

After investigating with existing and new architectures of harmonic tag design over the last quarters, the key factors of the harmonic tag design are identified as:

1) The tag should be very efficient in producing harmonics at low input power.

2) The antenna should be wide band to operate effectively under different soil condition.

3) The tag should be compatible with the manufacturing process of the pipe.

3. Injection Molding

Plastic injection molding process comprises of blanket covering of the target board using hot-melt. High density Polyethylene (HDPE) is used as the plastic resin for molding the parts. HDPE has the desired characteristics to protect the circuit attached to the pipe from mechanical tear and shear. Additionally, HDPE has the desired thermoplastic properties for molding. HDPE can endure high temperature (~250 °F) and resist different solvents and alcohols. Fig. 3.1 shows the procedure of plastic molding with the metal mold and tag inside. Spraying the alcohol (or release agent) on surface of the mold is to remove dust and particles on the mold and allow ease of release of parts after molding. To inject HDPE melt, the temperature of nozzle of plastic injecting machine set to approximately 500°F. This temperature was found to provide a suitable melt and parts with sharp corners could be easily fabricated. To sustain the regular injecting rate, the pressure of the injection machine was set to 50 psi using a nitrogen gas cylinder. Another reason to choose injection molding was it is compatible with regular plastic pipe manufacturing process.

The metallic mold was fabricated using aluminum (Al). A groove was cut inside the metal box to fit the circuit board inside the mold. Metal mold was chosen as it offers very good uniformity and surface smoothness. The mold frame geometry is shown in Fig. 3.2 with and without the sample. The mold comes in two pieces, which are clamped together with the sample inside before injection molding. The largest piece the mold can accommodate is 76 cm X 64 cm X 4 cm.

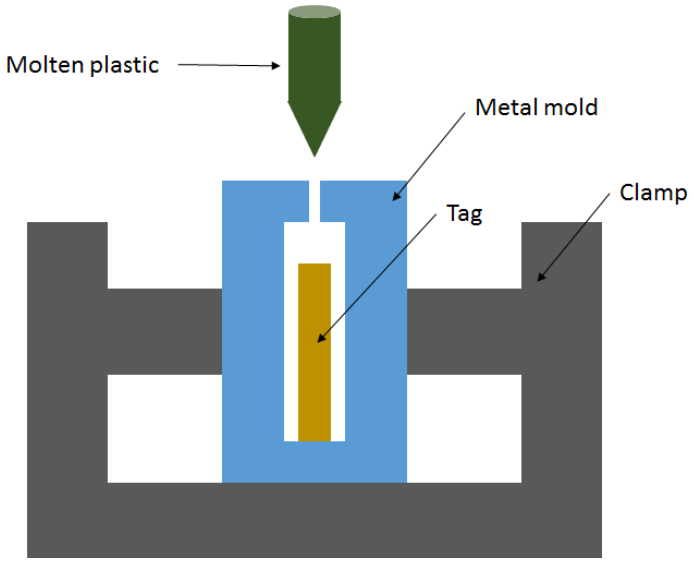

Fig. 3.1. Cross-section view of injection molding process.

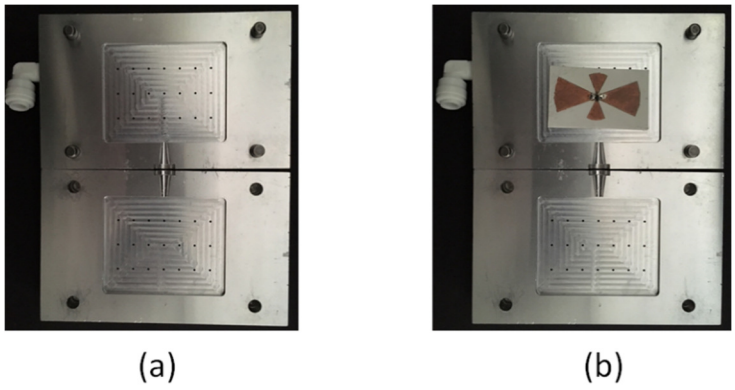

Fig. 3.2. (a) Aluminum mold and (b) Sample within the mold.

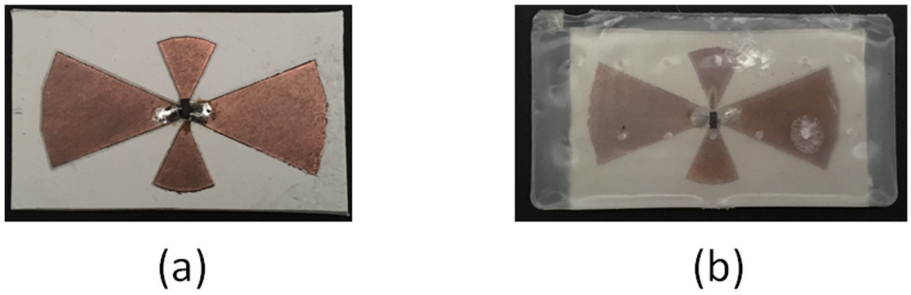

Fig. 3.3. **(**a) Tag before injection molding and (b) tag after molding.

The tag performance was evaluated before and after injection molding and the tag was found to be operating as expected. The glass transition temperature of the soldering iron was around 600 °F which was lower than the molding temperature. The molding time was set low (6 s) so that the molten plastic would not have enough time to melt the solder. In Fig. 3.3, the tag is shown before and after injection molding.

4. On-Tag Sensing and Signal Processing

Pipeline monitoring is critical for reducing the damages that can lead to loss of life, goods and services. The on-tag sensing and signal processing can help minimizing the threat by providing the necessary and critical information about the health of pipeline in real time. The literature on structural health monitoring of pipeline infrastructure suggests multiple parameters that are required to assess the current conditions and also to predict the remaining life. The important parameters include operating pressure of the pipeline, temperature and humidity conditions, which affects the integrity of the pipeline over time. Moreover, for plastic pipelines hydrocarbon permeation, rock impingement, cross-bore, joint failure, external stress, are also key challenges that can be detected or avoided using on-tag sensing technology. The current methods used for monitoring pipeline are inspired by popular active IoT solutions. The vast majority use the battery assisted wireless sensor tags that monitors absolute or relative pressure of pipeline, temperature and humidity. The real time monitoring using active tags is revolutionary but the economy do not comply with the large scale integration. The active sensor tags are expensive due to complexity, and do not last long due to limited life span of the battery.

The embedded passive harmonic RF tags can not only be used for detection and identification, the sensors can also be integrated along with the tag. The integrated sensors can pro-actively monitor the local conditions around (Inside and Outside) the pipe. In this report, the pressure and humidity sensors are presented that can be installed on a pipeline. The designed sensors operates passively without any requirement of an on-board battery and transmits back the sensor information to interrogator wirelessly. The pressure and humidity sensors are selected due to their importance in pipeline monitoring.

Additionally, the embedded harmonic passive RF tag can be used for precisely locating the pipeline buried under ground. The reflected signal from RF tags can be processed for distance information, which reduces the likelihood of hitting the pipeline during excavation.

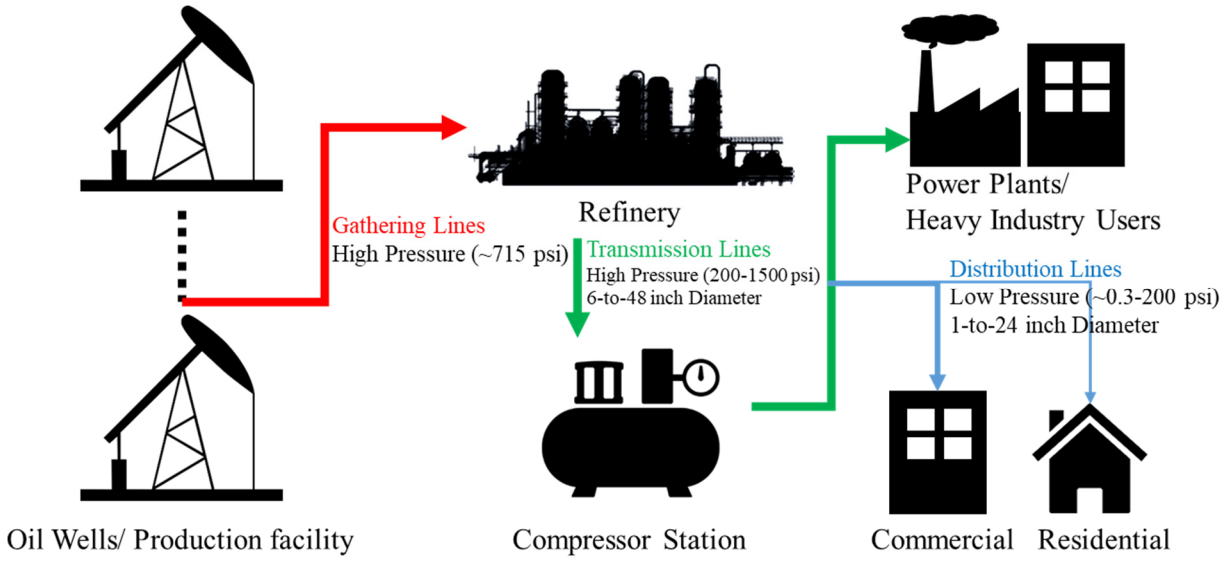

Fig. 4.1. Overview of the Natural gas Gathering, Transmission and Distribution Line infrastructure

4.1. Pressure Sensor

High pressure is one of the most important and found to be the primary cause of damage to the pipelines. A number of techniques have been proposed to monitor the pipeline pressure such as piezoresistive based sensors, capacitive sensors, and Fiber-Brag Grating (FBG) based negative pressure wave sensors. The major limitation of these sensing systems is that a direct wired connection is required for data acquisition. For example, FBG based pressure sensors requires an optical fiber cables running across the pipelines which is excited and read using a ground based system. The piezoresistive sensors acquire a differential pressure reading as voltage signal and the sensors are directly installed inside the pipeline. The direct probing or wired connection limits the application of the sensor and possess a problem for inaccessible environments like underground buried pipelines. A number of wireless sensing approaches have been proposed as an alternate solution to overcome the disadvantages of the wired sensing approaches. These approaches monitor the pressure in the pipeline by deploying large number of sensor nodes integrated on the surface of the pipes at specific locations and they transmit the data wirelessly to an interrogator. For example, Supervisory control and data acquisition (SCADA) pipeline monitoring system proposes active sensor nodes deployed across the pipeline for real-time pressure monitoring. The main disadvantage of active sensors is the need for an on board battery that increases maintenance and overall cost of the system. A battery-free, passive, low-cost, real-time sensing is ideal to provide a robust and inexpensive system with longer life and lower maintenance.

In this report, three types of pressure sensors were investigated, which includes 1) Stress loaded Patch Antenna Sensor, 2) Near-field (NF) LC tank based Pressure Sensor and 3) Far-field Capacitive Pressure Sensor.

4.1.1. Stress Loaded Patch Antenna Sensor

COMSOL Multiphysics simulation tool is used to check and validate the argument of stress loaded patch antenna sensor. A patch antenna for 1800 MHz is designed, shown in Fig.4.2 with the frequency response of the antenna.

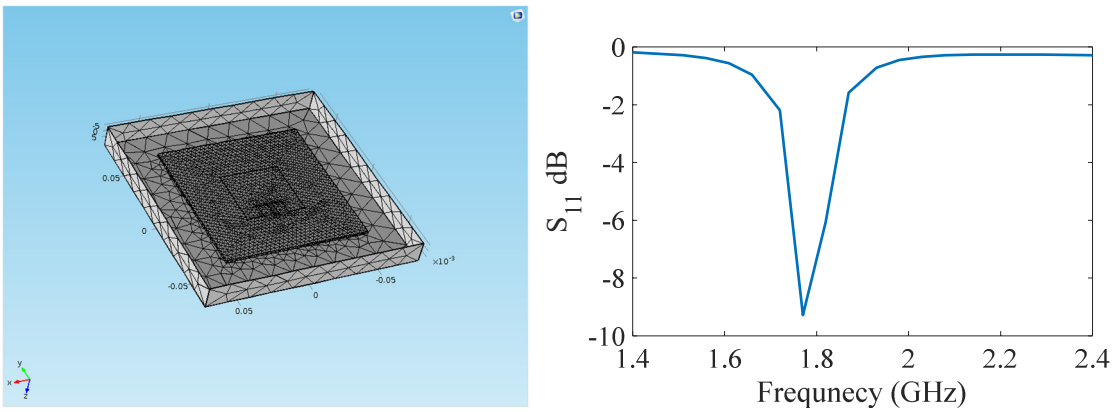

Fig. 4.2. COMSOL Model of Patch Antenna and Simulated S-Parameter

The study of solid mechanics is also added in the simulation model and a load of 1000N to 4000N is applied over the whole substrate. The changes are probed with the applied stress and the results are shown in Fig. 4.3.

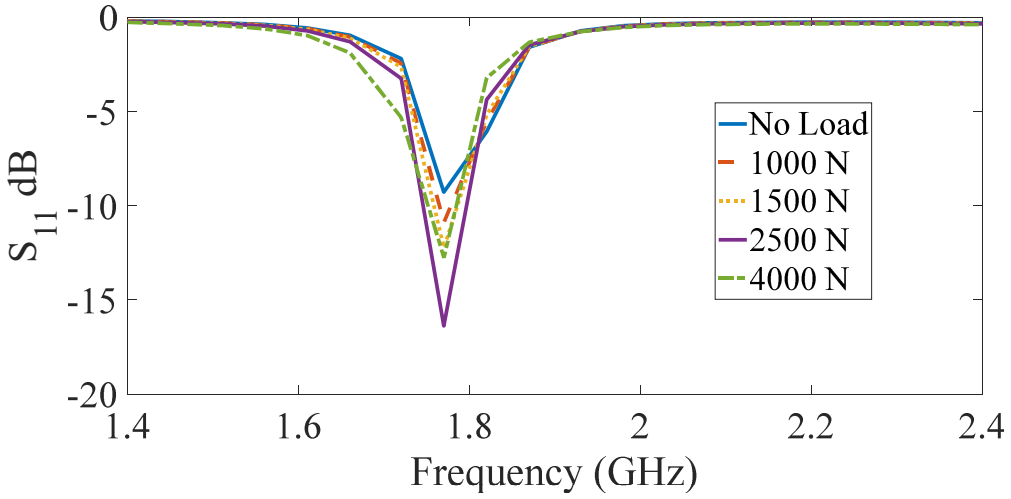

Fig. 4.3. Change in resonance frequency of the patch antenna due to applied load

The resonance of the antenna shifts with the stress can be clearly seen. In the simulations with different stress level, it is observed that the antenna can also be used to monitor any potential damage to pipe due to local stress.

4.1.2.LC Tank Based Pressure Sensor

The near-field LC Tank based pressure sensor is designed using a flexible thin film of feroelectret. The feroelectret is previously used as a Nano-generator that harvest vibration energy and transduces it into electrical energy. The feroelectret material is designed to be highly porous with a charge polarity. In the presence of any mechanical stress or vibration, the polarity of the material shifts and the corresponding capacitance across the electrode plates change as well. The phenomenon is shown in Fig.4.4.

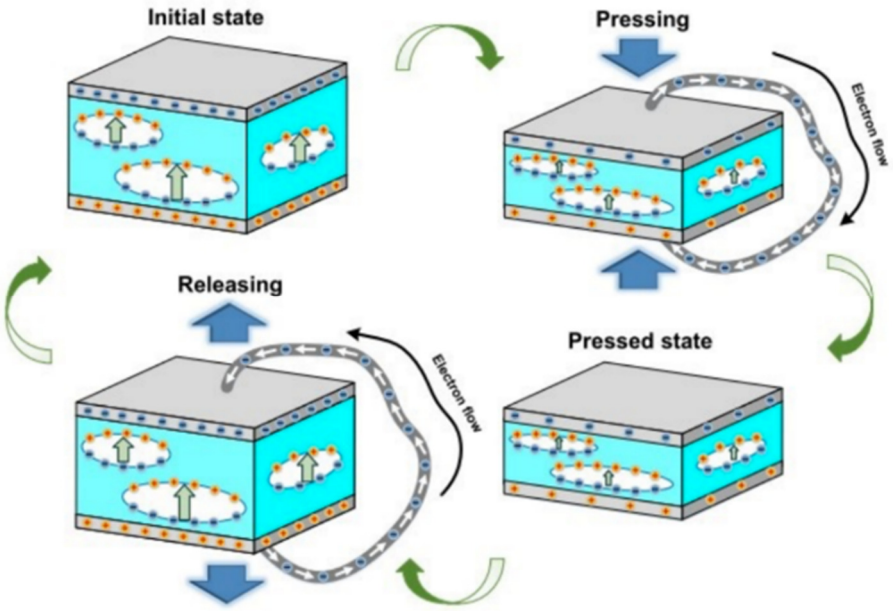

Fig.4.4. The working principle of the feroelectet based capacitive pressure sensor

The hypothesis is tested using an impedance analyzer and a mechanical stress inducing machine. The electroplated feroelectret based pressure sensor is shown in Fig.4.5 with the stress inducing machine.

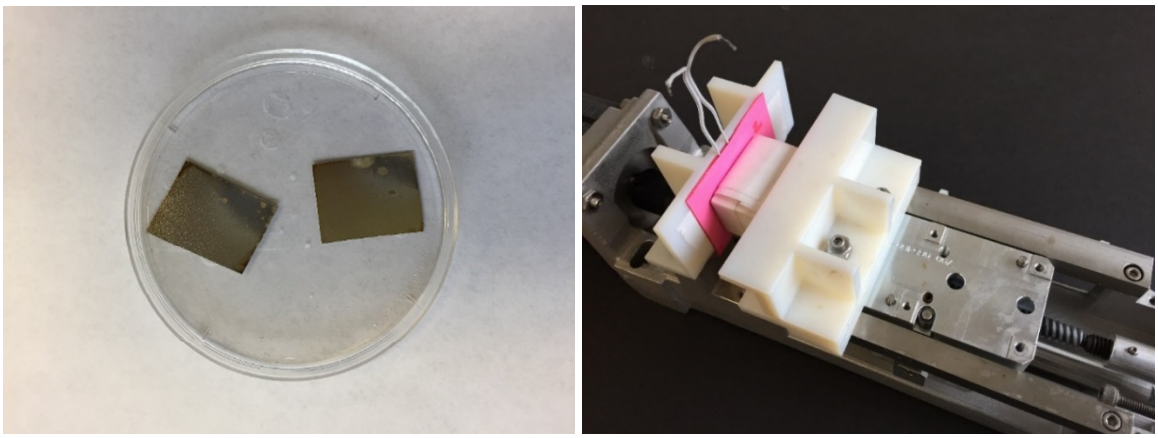

Fig.4.5. Fabricated sensor with the stress inducing machine

Five different stress sensors are designed with same size and shape for better reliability and validity. The impedance of all the sensors are measure over the range from 10 MHz to 30 MHz as shown in Fig. 4.6. The acquired impedance results shows consistency and similarity in between different sensors.

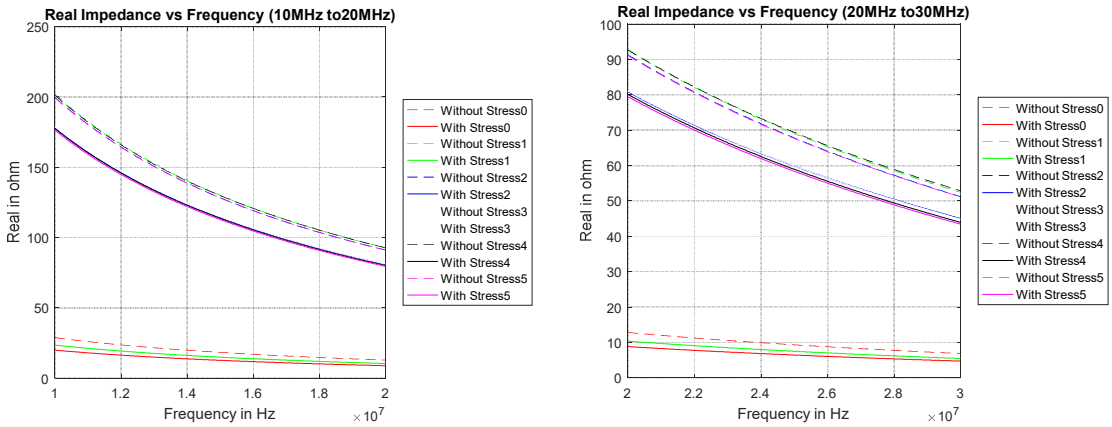

Fig.4.6. Frequency response of the capacitive sensor

The sensor 1 is selected out of 5 available sensors and a range of stress is applied for testing the sensitivity and linearity. The applied stress is quantified by number of steps taken by stepper motor while pressing the sensor. The observations are shown in Fig.4.7, where the impedance value decreases with the increase in stress.

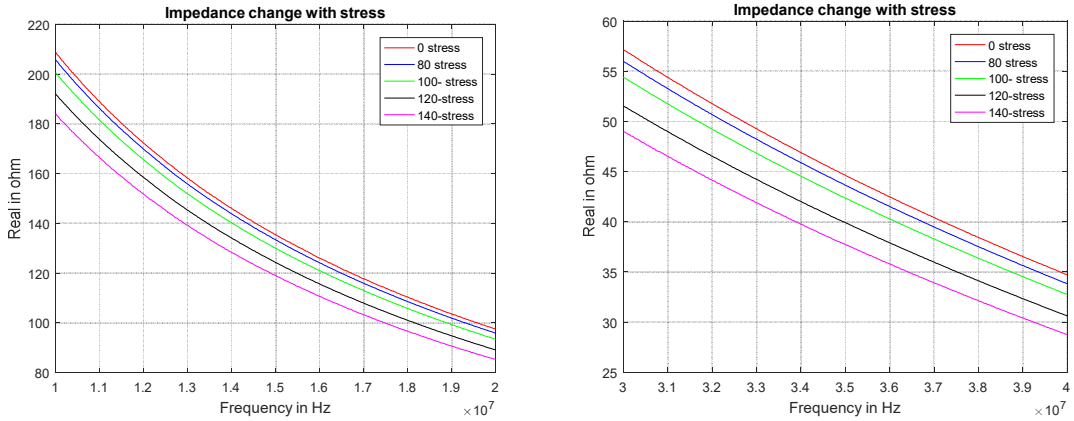

Fig.4.7. Frequency response of the capacitive sensor

The units of above shown stress is a single step of stepper motor. The additional stress from 80 units to 100 units makes a little change in impedance at higher frequency. But for the same stress change at lower frequencies shows a larger change in impedance as shown in Fig.4.8 and Table.1.

	80 to 100	100 to 120	120 to 140
@ 30 MHz	1.58	2.85	2.57
@ 1 MHz	46	85	77

Table 1

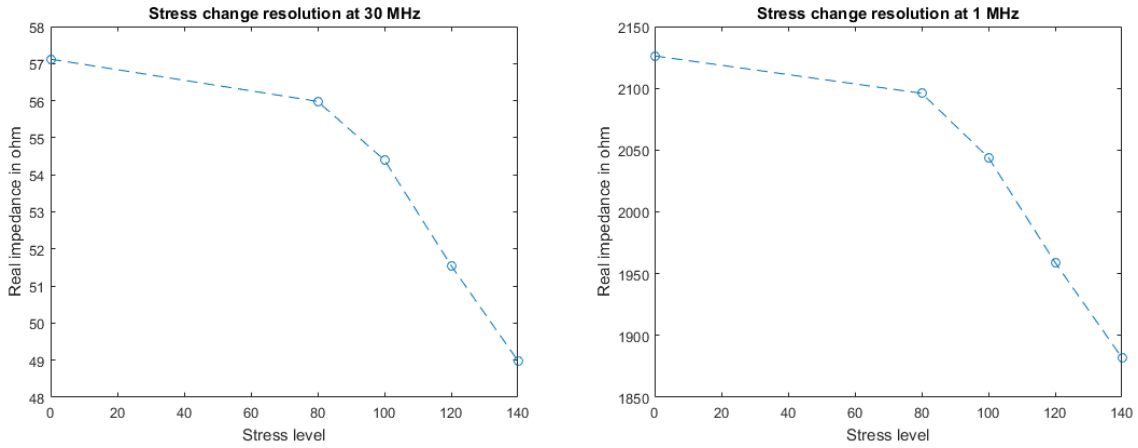

Fig.4.8. Change in impedance due to applied stress

The feroelectret sensor shows capacitive properties, which can be acquired using any active capacitance measurement device. An alternative method for detecting the change is capacitance is studied and applied to acquire the change passively. In literature, LC-tank based near-field approach is demonstrated for food and volatile sensing. The near-field probe use a coil reader that communicates with the LC-tank resonator wirelessly, and the change in capacitance is determined by the respective change in resonance. The block diagram of the measurement and sensor circuit is shown in Fig.4.9.

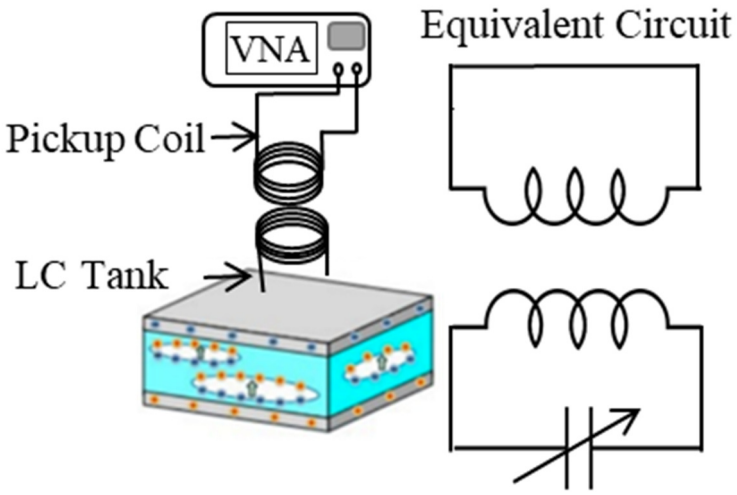

Fig. 4.9. Measurement setup for LC-tank based stress sensor

The feroelectret based stress sensor consist of a thin and porous sheet with two silver electrodes on both sides. The design makes it a lossy capacitor, which changes its characteristics according to the applied load. Calculating the precise change in capacitance is easier in lab environment but there is no direct method that can wirelessly read the capacitance change.

In order to get the change in capacitance wirelessly, the indirect method uses an Inductor-Capacitor (LC) resonator shown in Fig.4.10. The inductance in the circuit is kept constant and the variable capacitor is the stress sensor itself. The measurements are made wirelessly using a pickup coil and the initial frequency response of sensor is shown in Fig.4.11.

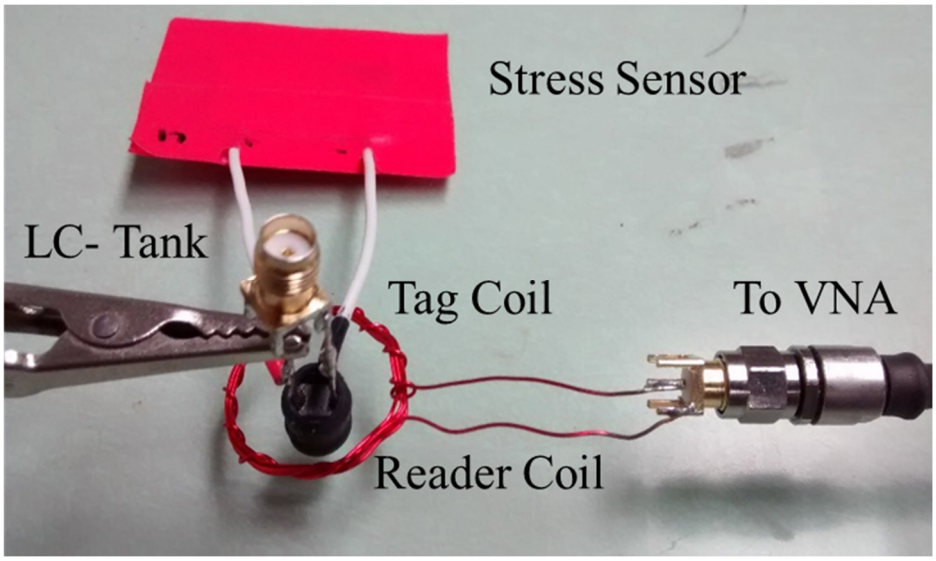

Fig. 4.10. Lab setup for measuring the frequency response of stress sensor

High values of inductor and capacitor makes the resonance frequency around 1-MHz. The resonance can be tuned by changing the net inductance of the circuit.

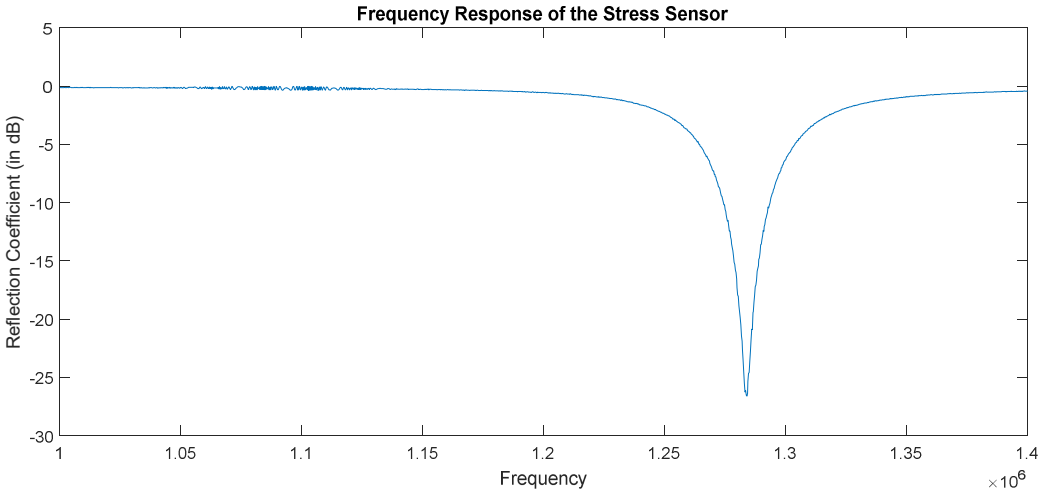

Fig.4.11. Frequency response of the stress sensor

With the applied stress, capacitance changes, and so does the resonance shown in Fig.4.12. Four metal loads are used to apply stress over the sensor with equal weight and shape. The first metal load makes a significant changes in resonance and shifts it by 36.5 KHz. Additional consecutive loads also shifts the resonance by a linear average of 9 KHz. Comparing these results to the previously shown impedance measurements due to applied stress, shows that resonance frequency is more sensitive towards detecting small stress or pressure changes, and also shows a better linear correlation between different stress loading.

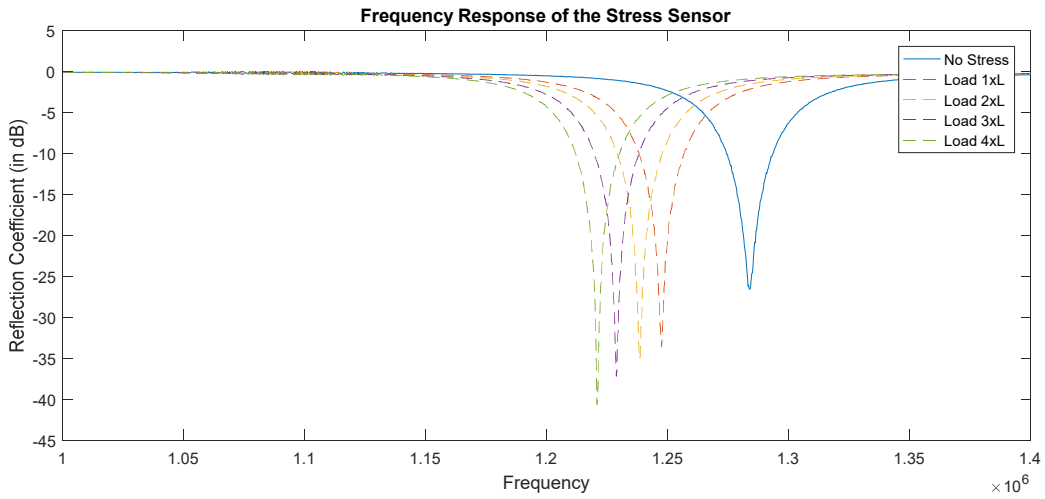

Fig.4.12. Shift in resonance frequency due to applied stress

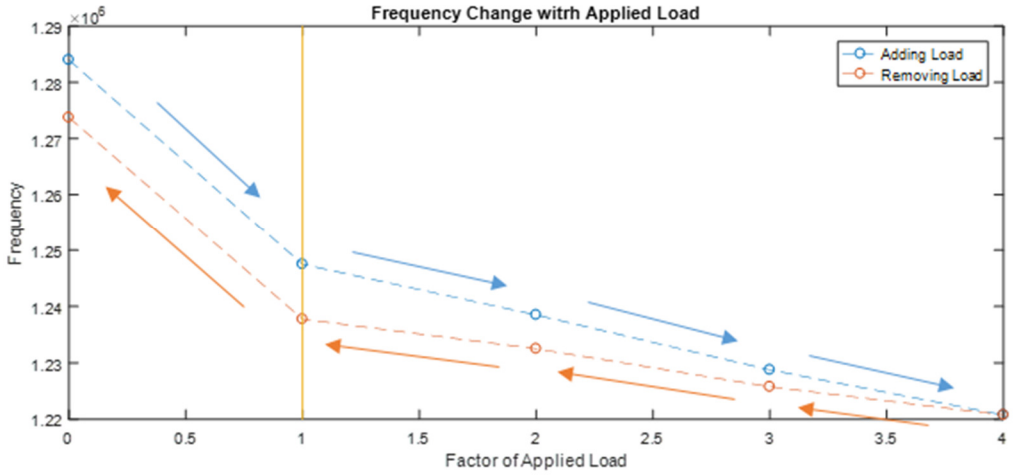

Fig.4.13. Change in resonance frequency while applying and removing stress

The feroelectret stress sensor takes some relaxation time to regain its original shape after applying pressure by some heavy load. Fig.4.13 shows the change in resonance while adding load and also while removing it. The net change in capacitance due to four equal loads is linear both ways, but the sensors do not fully regain their shape or capacitance, which leads to different resonance with the same applied load.

Many different sizes and shapes of stress sensor, shown in Fig.4.14 (a), have been studied for getting any specific capacitance even with size limitations. Sensor 4 in Fig.4.14 (a), sensor 4 in Fig.4.14 (b) and sensor 2 in Fig.4.14 (c) are all made with the same size of PPFE film, but are organized in different configurations to achieve smaller net surface area by respectively folding and stacking the PPFE. The single layer & folded sensor configurations give relatively the same internal capacitive response, while the stacked sensor capacitance is much larger, due to parallel plate configuration and this pattern is followed by the other sensors shown in Fig.4.14.

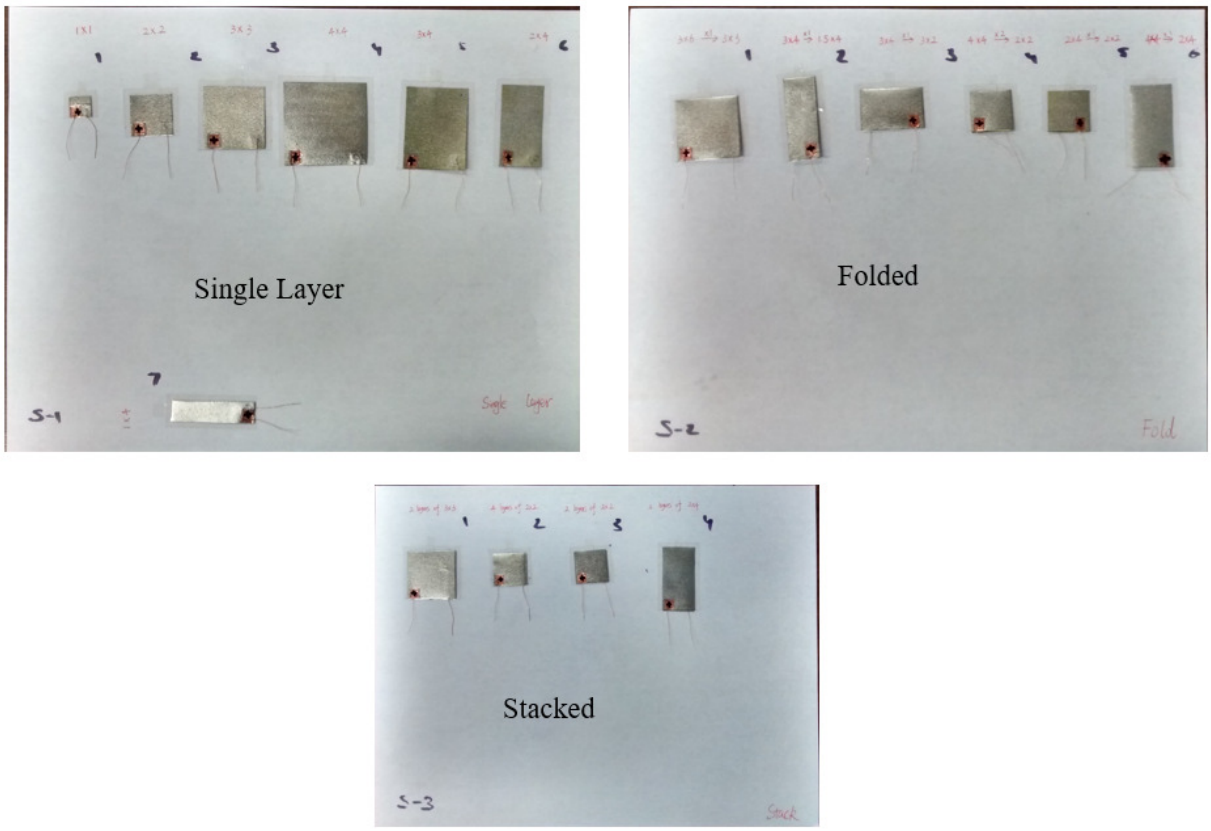

Fig.4.14. Different fabricated feroelectet based stress sensors

Configuration	Total Area	Impedance @ 15MHz
4x4 [single fold]	16mm^2	43.63
2x2 [folded]	16mm^2	47.39
2x2 [stacked]	16mm^2	210.33
2x4 [single fold]	8mm^2	70.76
2x2 [folded]	8mm^2	67.25
2x2 [stacked]	8mm^2	232.01

Table 2

4.1.3.Far-field Capacitive Pressure Sensor

Inductor-Capacitor (LC) based passive sensor tags have been proposed for monitoring pressure based on capacitive loading of pressure that in turn shifts the resonance frequency. The capacitive element is either a parallel plate configuration or inter-digited configuration. These sensors are near-field and have limited interrogation distance. The far-field passive pressure sensors operate at single frequency and are prone to clutter due to their lower signal to noise ratio. To overcome these limitations, a harmonic doubler approach is desired that eliminates clutter and increases the SNR. Harmonic doubler based passive sensors have been reported in literature for sensing liquids, wall cracks and food. In this work, a far-field passive harmonic tag with integrated pressure sensor having improved signal to noise ratio and better clutter rejection is presented for the first time for monitoring pipeline infrastructure.

The proposed sensor tag consists of three components, transmitter and receiver antennas, a harmonic doubler, and an integrated pressure sensor with a hybrid coupler. The receiver antenna operates at the fundamental frequency (fo) and the transmitter antenna operates at the second harmonic frequency (2fo). The proposed sensor is a parallel plate capacitor with a deformable dielectric substrate between the plates that changes capacitance with change in pressure. A hybrid coupler converts the change in pressure to the phase that can be interrogated wirelessly. The interrogator has access to cloud which can seamlessly integrated with SCADA's current monitoring system. A schematic of the proposed sensing system over the pipeline infrastructure is shown in Fig.4.15.

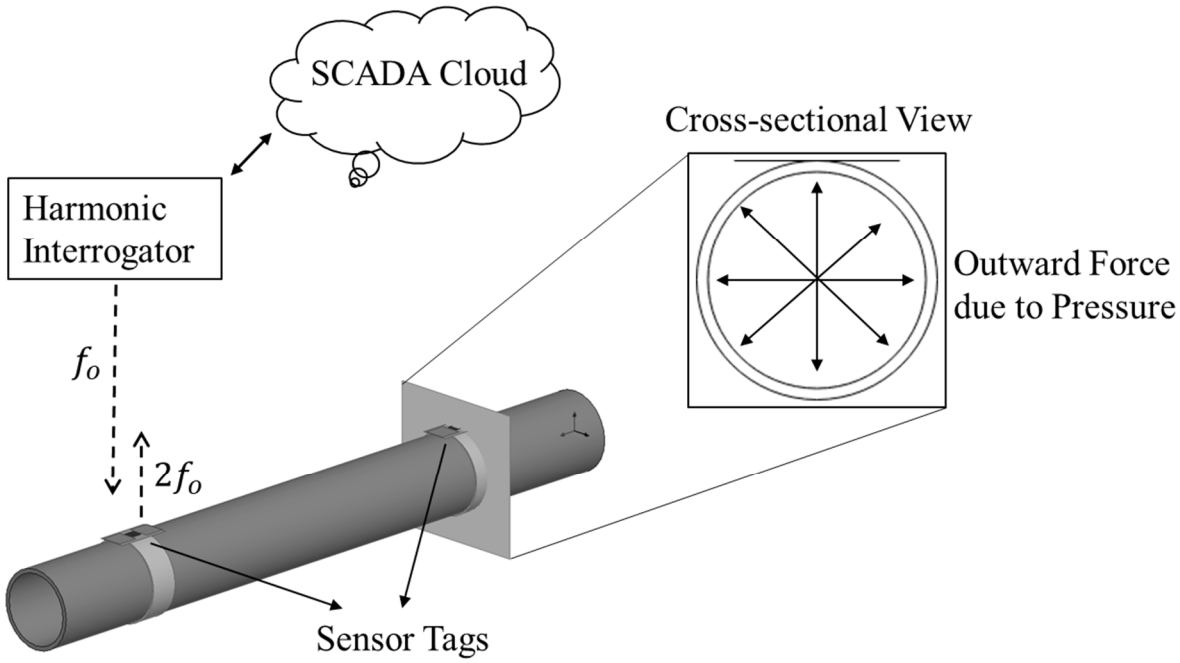

Fig.4.15. IoT based pipeline pressure monitoring system using passive tags

The high pressure operation exerts an outward normal or circumferential force on the pipeline. Due to the outward normal force, the pipeline expands leading to a net difference in the circumference.

The pipeline's expansion is very small (micrometers) and directly proportional to the applied pressure. The small difference can only be detected using a highly sensitive spatial movement probe that can be provided using capacitive sensors. The parallel plate capacitive sensors are extremely sensitive towards the separation in between electrodes, which can be positioned on the outer surface of the pipe for reading the change in circumference. The mechanism of change in separation due to applied pressure is shown in Fig.4.16. The capacitance of the parallel plate changes with change in separation of the plates since the capacitance is inversely proportional to the separation. The sensitivity and range of capacitive type pressure sensors are defined from the properties of the dielectric substrate in between plates. The rigid substrate will be able to take a very high pressure before deforming whereas the flexible substrate will deform with a respectively lower pressure.

In this work, three different flexible substrates are characterized for sensing pressure, Polydimethylsiloxane (PDMS), Polypropylene (PP) and Polyurethane Foam (PF). The electrical and mechanical properties of the chosen substrates are listed in Table 3. The Young's modulus provides the upper limit of the pressure that could be applied to the material before it is permanently deformed.

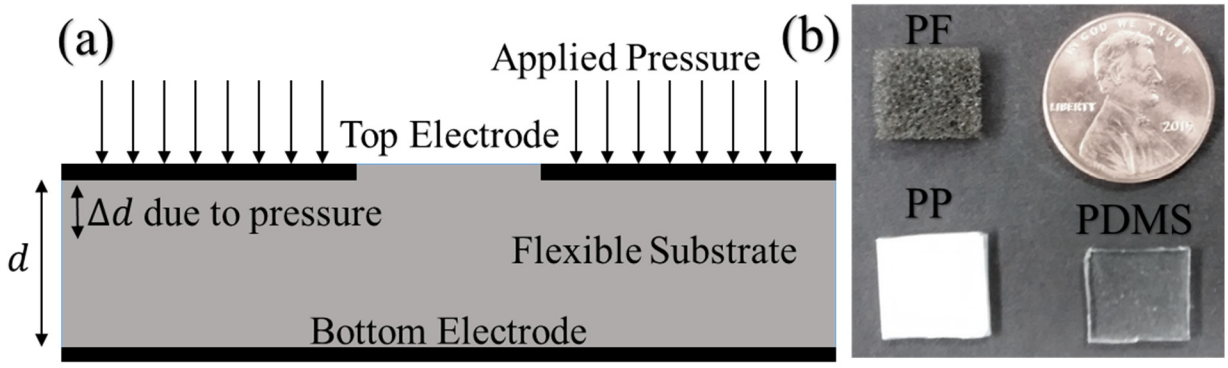

Fig. 4.16. (a) Capacitive sensor structure, (b) Substrates used for different loadings

Substrate	Dielectric Permittivity	Young's Modulus
PDMS	2.32-2.40	1.4-1.6
PP	2.3-2.36	0.9-1.5
PF	2.0-2.2	0.08-0.93

Table 3

The proposed wireless pressure sensor uses a phase shifting based RF tag for wirelessly transmitting the change in capacitance due to applied pressure. The hybrid coupler is used as a phase shifter, which is a four port reciprocal device with a single input, output, isolation, and coupled ports. The coupler is designed and simulated using ADS on an FR4 substrate with dielectric constant of 4.4 and loss tangent of 0.02. The coupler's operating frequency is at 2 GHz with a 3 dB coupling factor and 20 dB isolation. The schematic of the coupler along with the dimensions are shown in Fig.4.17.

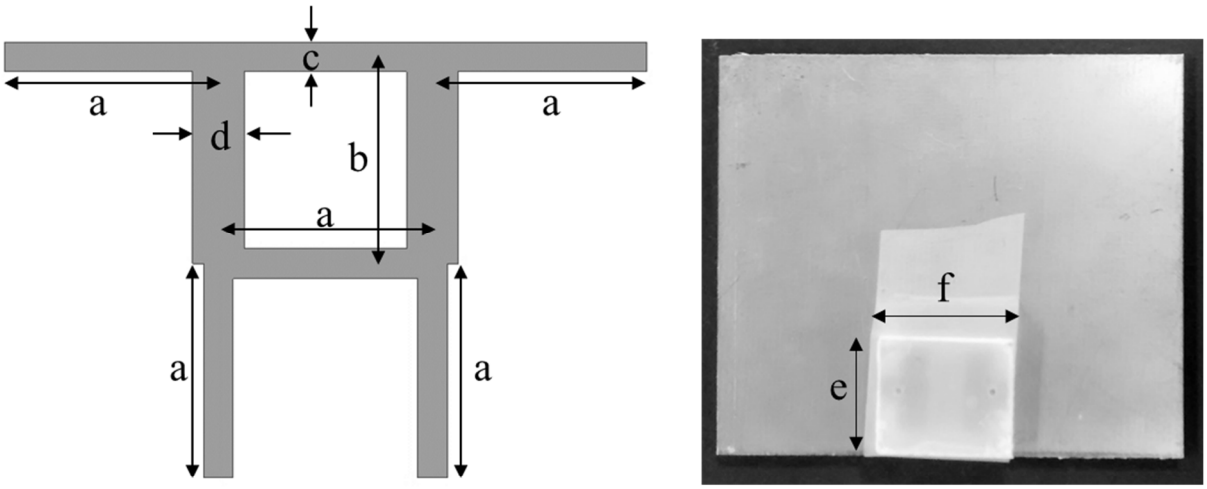

Parameter	a	b	c	d
Dimensions (mm)	20.5	19.9	2.86	4.92

Fig.4.17. Designed hybrid coupler with integrated capacitive pressure sensor

The developed capacitive sensor is integrated onto the coupler for converting the change in capacitance to RF signal's phase. The dimensions of the capacitive sensor is 10mm x 12 mm with two electrodes on the top and a single electrode at the bottom as shown in Figure.2. The dimensions of the top electrodes are 10mm x 5mm that are connected to the coupler's ports. The output and coupled ports are terminated with capacitive sensor that reflects back all the power and introduce a phase shift according to the respective capacitance.

The antenna can connected to the input port where the signal is received and is transmitted back from the isolation port with a shifted phase. But the single frequency operation for wirelessly communicating with the sensor is prone to clutter and lower signal to noise ratio. In order to avoid clutter, the communication via harmonic signal is proposed. Two different standard patch antennas operating at 2 GHz and 4 GHz was used as a receiver and transmitter for the tag respectively. The schematic of the complete tag is shown in Fig.4.18.

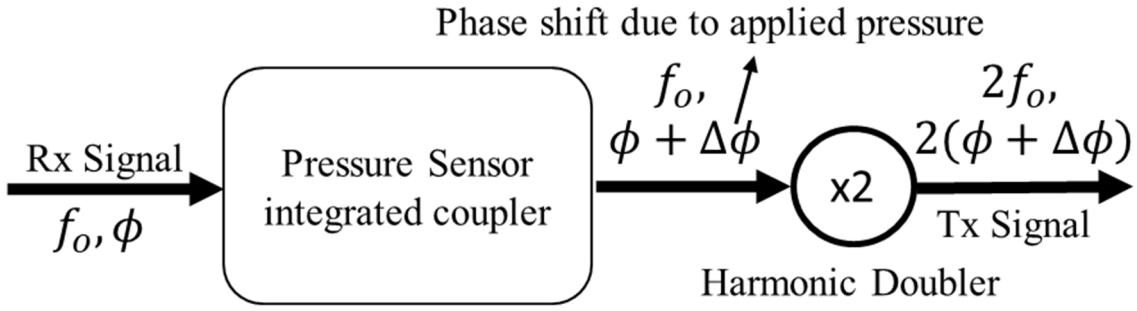

Fig.4.18. Block diagram of the passive harmonic RF Tag

The 2 GHz patch receives the signal from the interrogator and feeds it into the sensor. The output of the sensor is doubled and the transmitter antenna reflects it back to the interrogator at the second harmonic frequency with a very low phase noise. The interrogator consists of two commercial wide band Vivaldi antennas, a vector network analyzer, and RF peripherals for precisely detecting the phase change. The schematic of the measurement setup is shown in Fig.4.19.

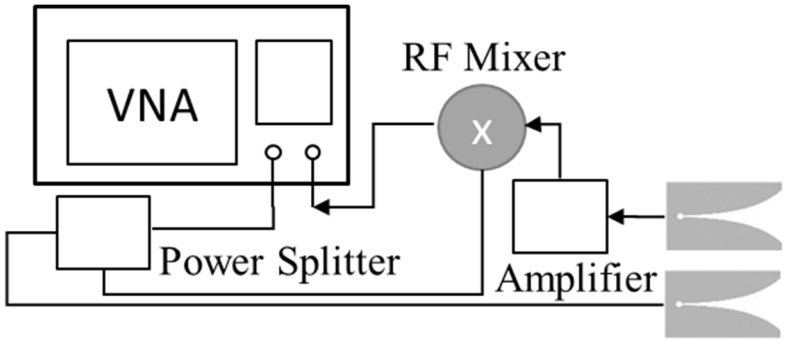

Fig.4.19. Block diagram of the harmonic phase measurement setup

To validate the operating principle of the proposed sensor, a set of simulations were performed in ADS using hybrid coupler with feed at input port, measurement at isolation port and the capacitive sensor is coupled to other two ports. The capacitance is varied from 0.7 to 1.3 pF and the results are plotted in Fig.4.20.

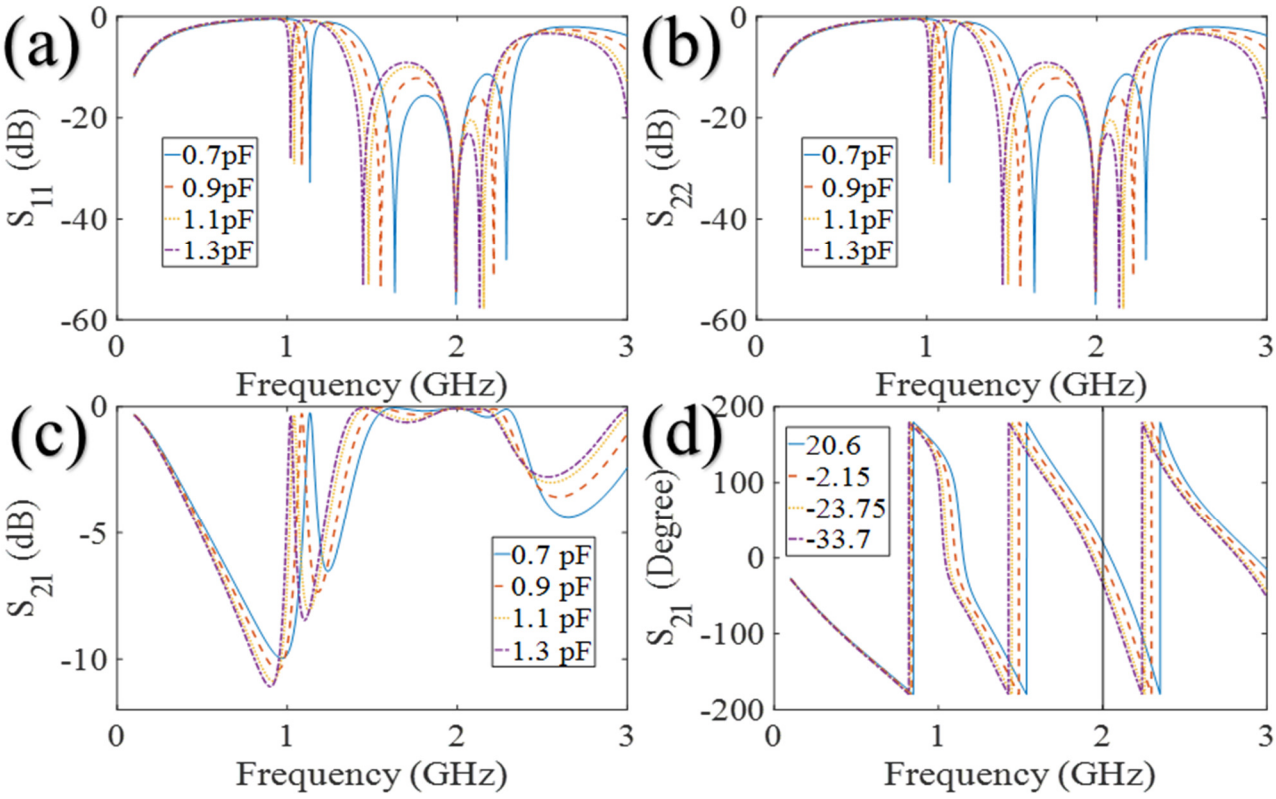

Fig. 4.20. Simulated frequency response of the hybrid coupler with change in capacitance

It can be inferred from the graph that, a small change in capacitance (0.6 pF) induces a change of 55° in phase (Fig.4.20 (d)) without any significant power loss (Fig.4.20 (c)) at 2 GHz.

Three set of experiments were performed to validate the operating principle, the first set of experiments show the change in separation of electrode (distance) for different applied pressure using laser vibrometer. The laser source used in this experiment (Polytec) is operated at the range of 640-um/V with 640-nm resolution. The capacitive sensor is fixed at a position under the laser as shown in Fig.4.21 (a) and the load is applied on the top. The change in output voltage is acquired and converted into displacement as shown in Fig.4.21 (b). The polyurethane foam is found to be more deformable than PDMS or PP, so the change in separation is more for the same applied pressure.

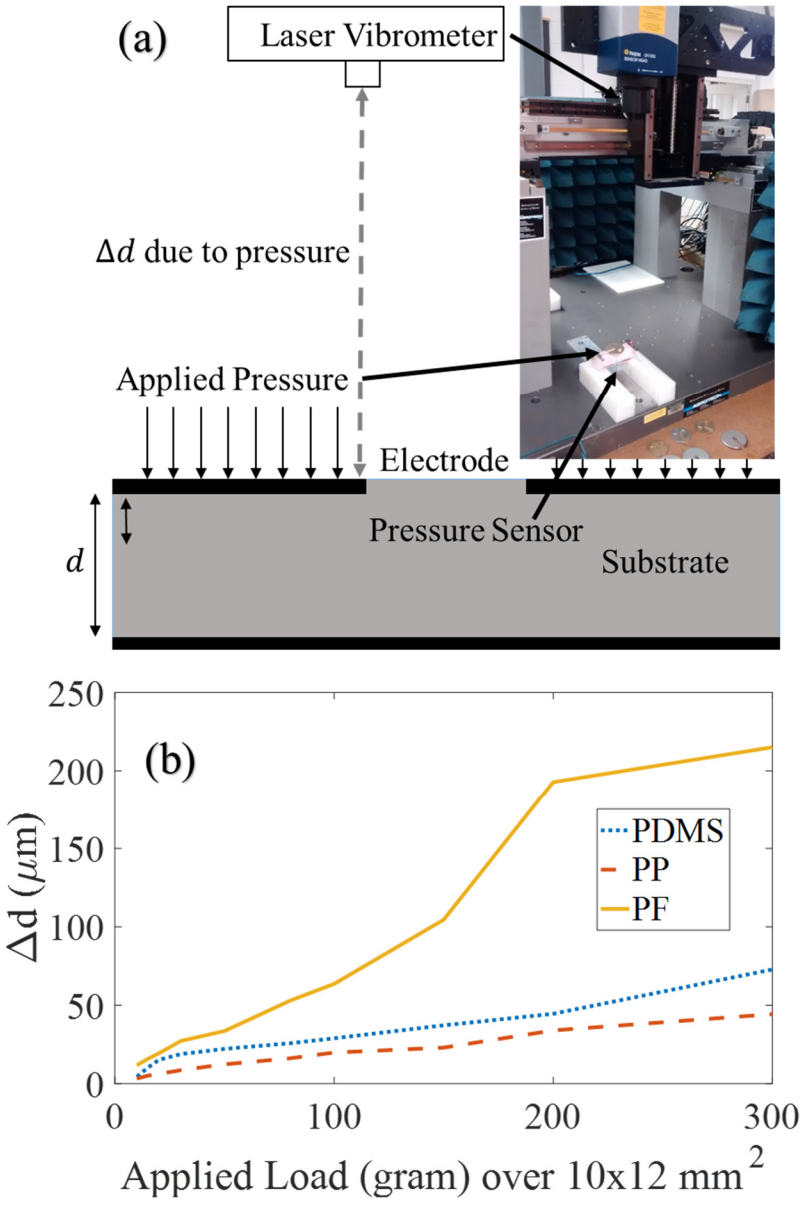

Fig.4.21. (a) Spatial movement measurement setup using laser vibrometer, (b) Change in separation of the electrodes due to applied load

The second set of experiments were performed by direct wired approach to validate the sensitivity of the designed sensor. The capacitive sensor coupled to the hybrid coupler is directly connected to a vector network analyzer (VNA) for verifying the phase change by measuring the S-parameters. The measurement set up is shown in Fig.21a and the measured results of relative phase change due to a range of applied pressure for three different materials is shown in Fig.4.22 (b).

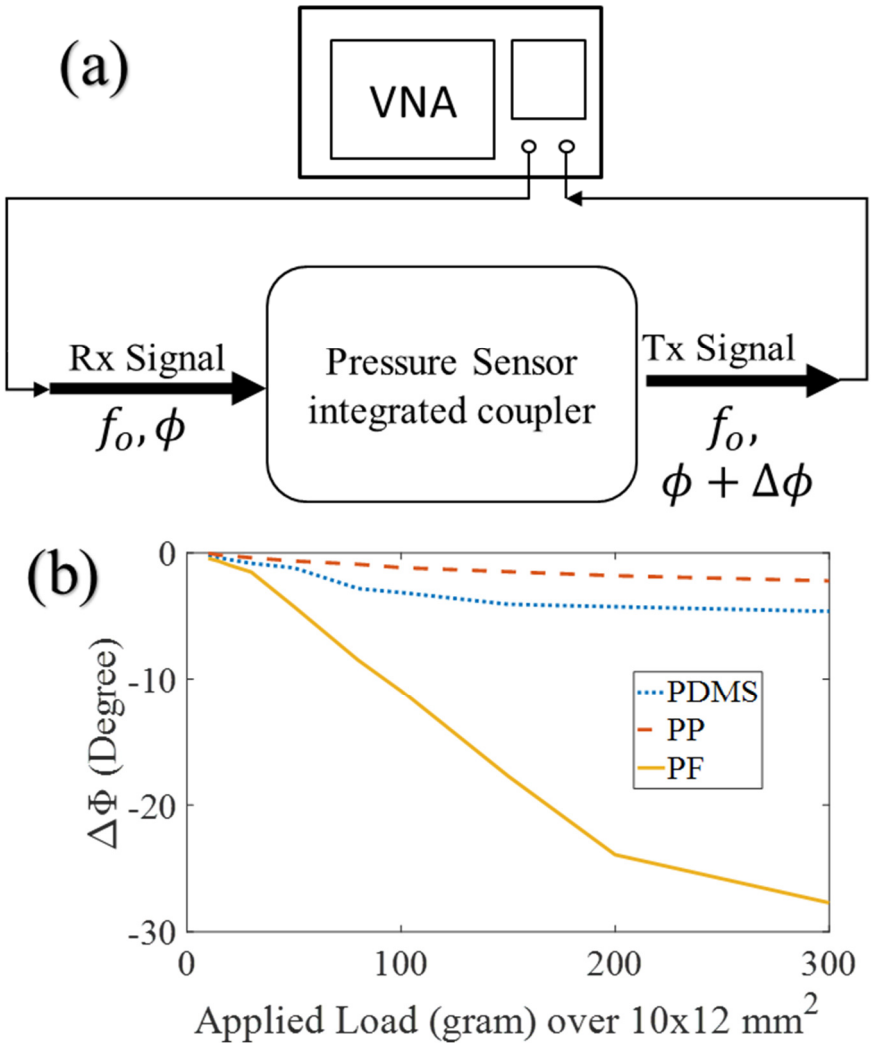

Fig.4.22. Change in phase due to applied load in wired configuration

The third set of experiments were performed to validate the wireless sensitivity of the designed sensor. The harmonic phase measurement setup schematic is shown in Fig.4.19.

In this setup, the VNA is used as a source as well as phase acquisition device. The power from the VNA is split for feeding the sensor and also used as reference for RF mixer. The output of the splitter (+7dBm) is connected to a Vivaldi antenna with vertical polarization for transmitting at 2 GHz. The sensor tag is placed 12-inches (1-ft) away from the interrogator and receives -10dBm input power. The received signal is frequency doubled using the doubler diode and the phase is changed based on the capacitive loading from pressure sensor. The harmonic doubler provides an output of -38dBm at 4 GHz with -10dBm as input at 2 GHz. The phase shifted, frequency doubled signal is transmitted back to interrogator using a patch antenna with horizontal polarization. The

received signal at the interrogator has a very low power (-60dBm), which is amplified to -18dBm using a low noise amplifier. The amplified signal (4 GHz) is mixed with the reference signal (2 GHz) and the phase change in output signal is acquired at 2 GHz. Fig.4.23, shows the measured results for a range of applied pressure on three different substrates.

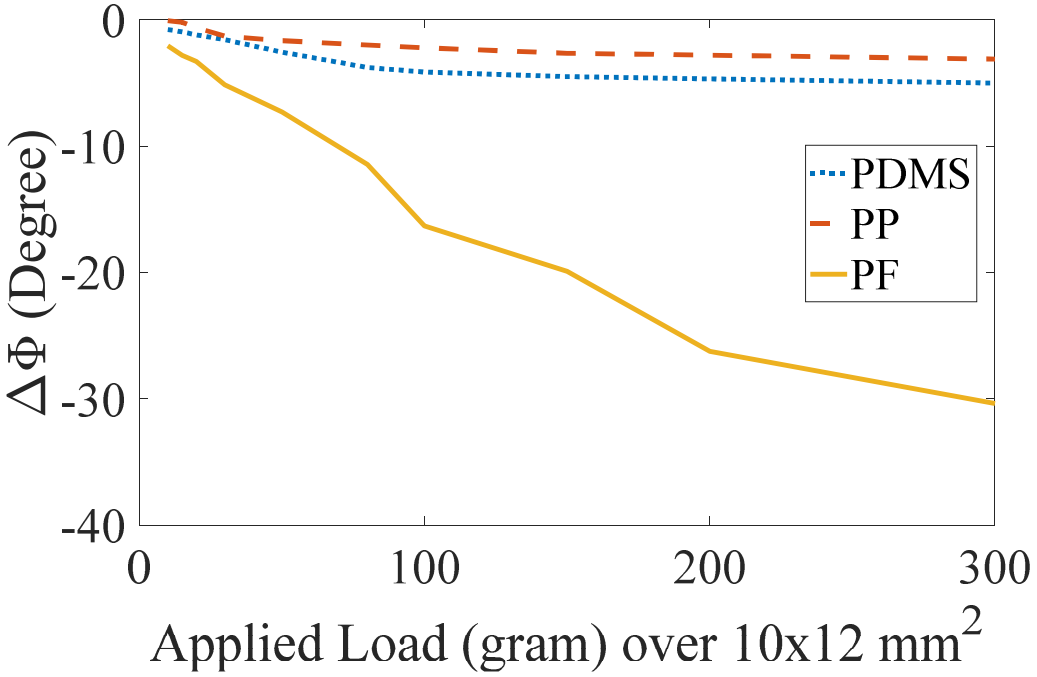

Fig. 4.23. Change in phase due to applied load in wireless configuration

The work presents a passive harmonic wireless pressure sensor consist of two antennas, a hybrid coupler and a doubler. Capacitor is the main sensing element that is connected with the hybrid coupler for the phase modulation of the incoming signal. The capacitor is realized using three different commonly available substrates: PDMS, PP and foam. The indirect pressure measurement technique is offered that can reduce the additional risks from drilling pipe for sensor placement. The change in phase due to capacitance is simulated in ADS and verified using VNA. The simulated results closely match with the observed experimental results. Harmonic generation and double phase acquisition is also verified using doubler and RF mixer. The integrated sensor tag is interrogated from a distance of 12 inches (1-ft) with only +7dBm transmitted power. The sensor can detect indirect pressure ($\geq 5\ \mu m$), which make it sensitive towards very small changes. The sensor network of the developed passive wireless RF sensor tag can be used for structural health monitoring of very large infrastructure, which is an economically viable solution.

4.2. Soil Moisture Sensor

The soil moisture sensor is designed according to the findings of the previous reports that the soil is a dielectric material and changes its permittivity according the added moisture contents. The moisture contents not only increase the relative permittivity but also effects the conductivity. A metamaterial based dielectric sensor is designed which has two square rings coupled to the transmission line for large Q-factor and high sensitivity. The designed sensor follows the metamaterial band pass configuration where the resonance frequency shifts according the dielectric loading over the rings. The designed sensor is shown in Fig.4.24 with dimensions.

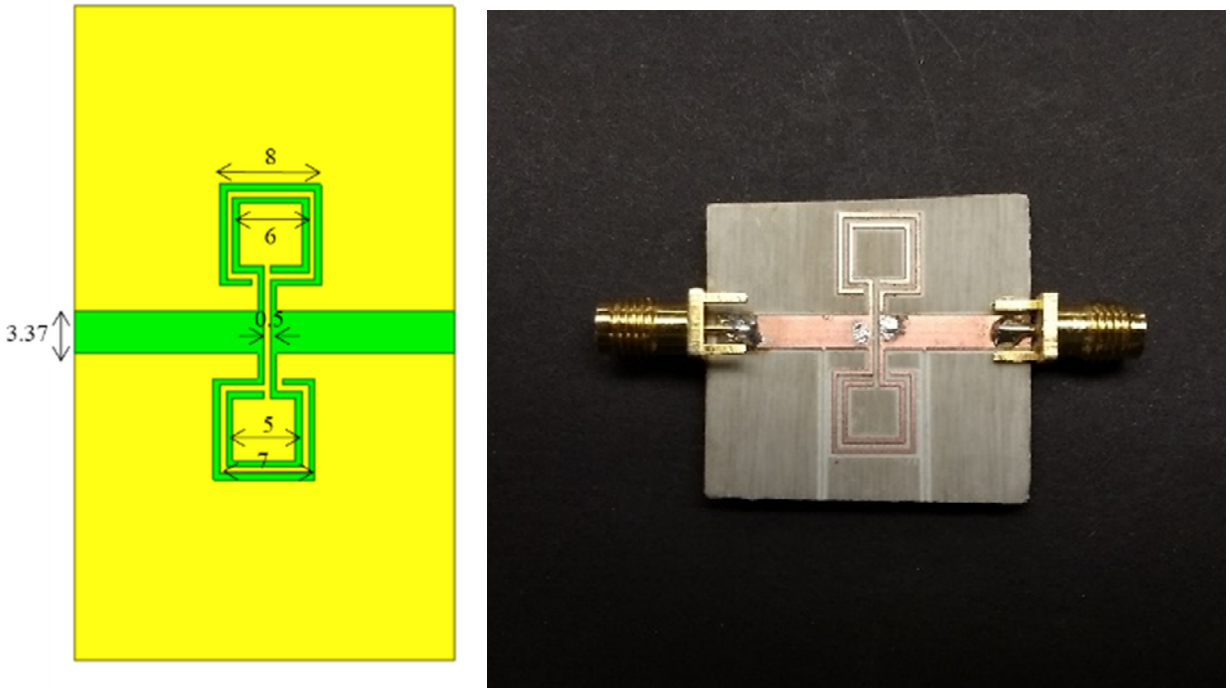

Fig.4.24 Designed sensor and its dimensions

Simulation results:

The sensor is simulated in Ansys HFSS and the simulated results are shown in Fig.4.25. The dual ring configuration gives two resonance peaks around 1.5 and 2 GHz. The system is designed to operate at 2 GHz under soil conditions, which further lower down the resonance frequency due to the dielectric loading and allows us to keep the air resonance of at a higher frequency.

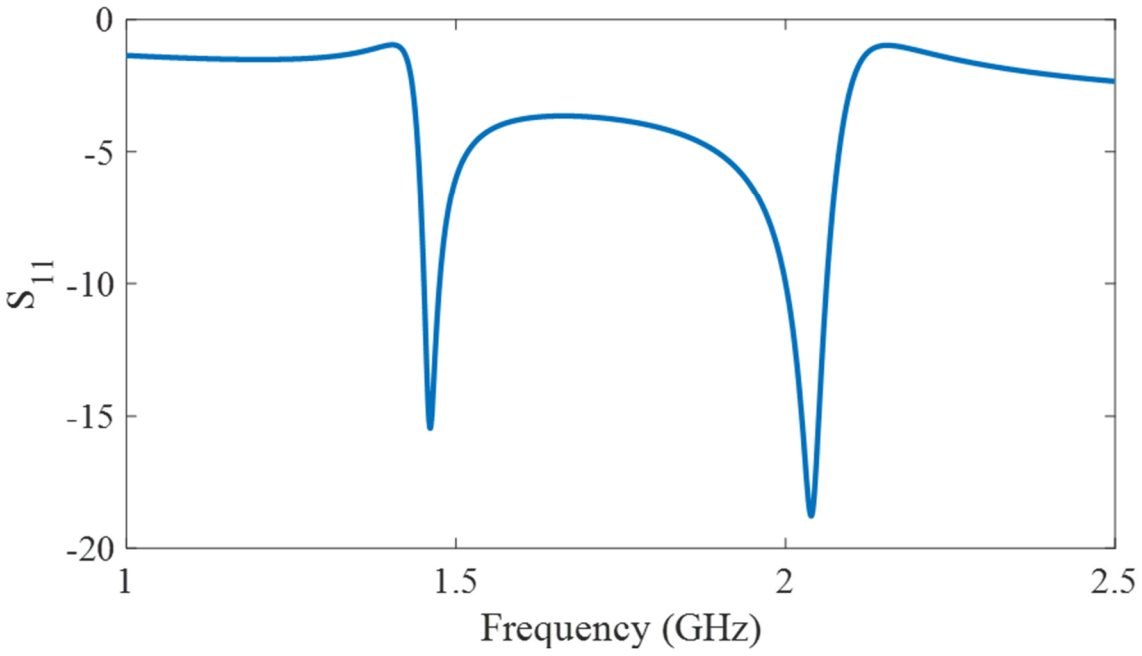

Fig.4.25. Simulated results of the designed sensor in HFSS

Experimental results:

The designed sensor is fabricated and tested using VNA, the measured frequency response is shown in Fig.4.26. The measured response is similar to the simulated response with two resonance peaks. The Q-factor of the fabricated sensor is larger and also the resonance frequency is comparatively higher.

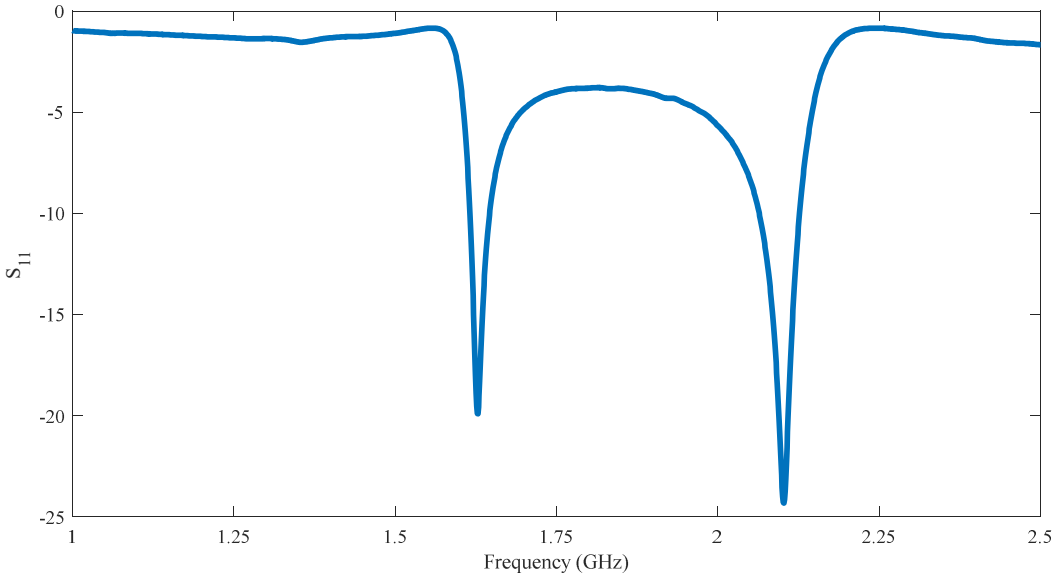

Fig.4.26. Measured frequency response of the metamaterial based sensor

The sensor is tested using known dielectric loadings, which are three selected Rogers's laminates with permittivity of 3.6, 6.0 and 10.0. All selected laminates has a height of 1.52 mm and the respective frequency response is shown in Fig.4.27. The resonance shift rate is high near low dielectric constant and slower down with the increase in dielectric constant. The shift is consistent towards left with the increase in permittivity.

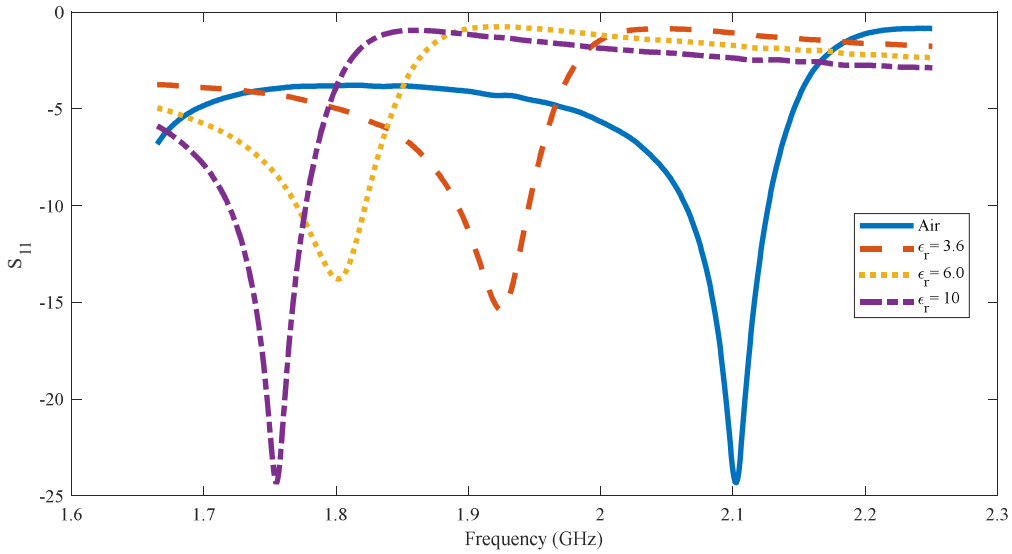

Fig.4.27 Frequency response with different dielectric loading

The similar dielectric loading experiment is performed using soil and moisture, shown in Fig.4.28. The dry soil shifts the resonance equivalent to the dielectric constant around 4.0, which has been observed in previous reports under controlled experiments. The added moisture content increased the permittivity and further lower down the resonance peak. It shows that the designed moisture sensor can detect moisture with different percentage.

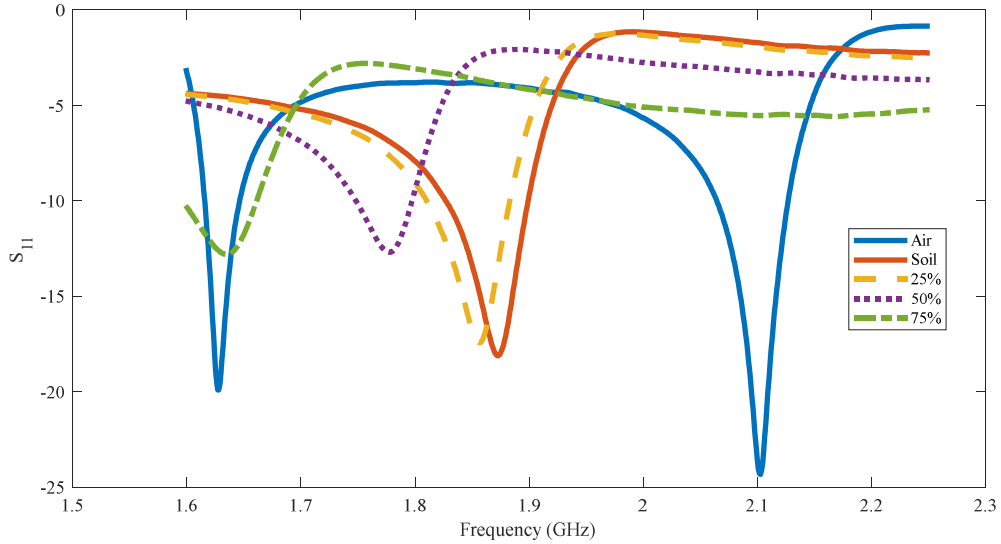

Fig.4.28. Frequency response due to soil and its moisture content

The next experiment is performed using antennas for wireless communication under soil as shown in Fig.4.29. The interrogator is placed over a container of soil with a pipe replicating a pipe leak under soil. The sensor integrated with antenna is placed on the pipe and buried under soil. The tag operates at 2 and 4 GHz, where it receive the signal at 2GHz and reflect back at 4 GHz. The integrated moisture sensor effects the reflected power according to the dielectric loadings. Fig.4.30 shows the change in harmonic received power for the standard dielectric materials. The reflected power lowers down at 4 GHz with the increase in the permittivity. Fig.4.31 shows the effects from air to soil and the additional moisture contents. The results shown a significant drop in power with loading of sensor and antenna's with the soil and moisture.

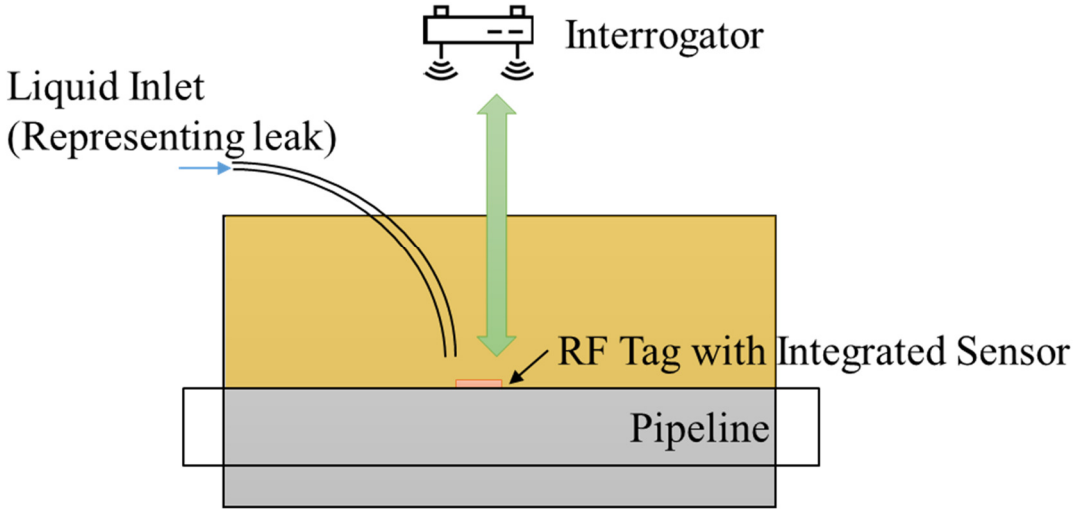

Fig.4.29. Wireless soil moisture measurement setup with block diagram

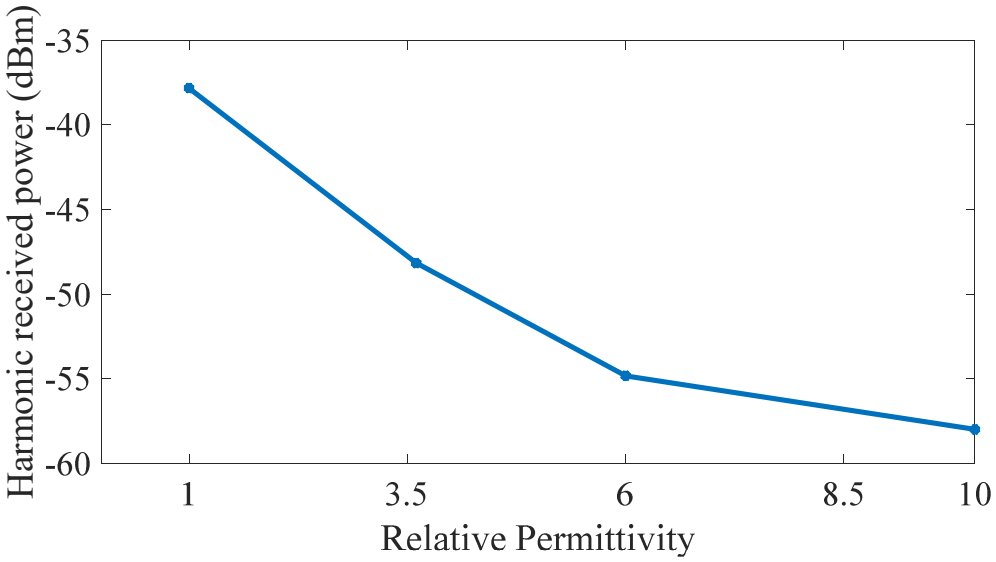

Fig.4.30. Wireless harmonic received power with dielectric loading

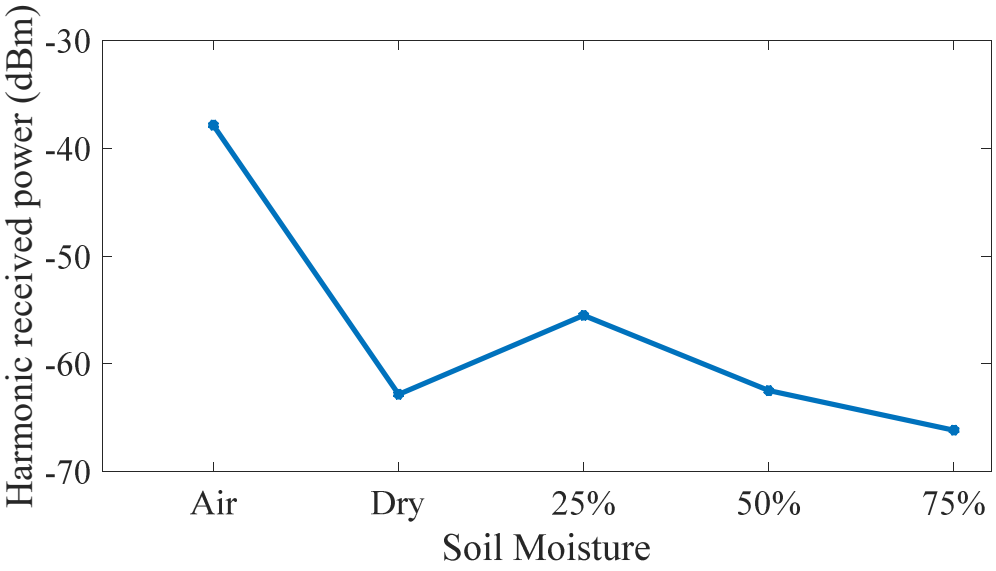

Fig.4.31. Wireless harmonic received power with soil and moisture content

4.3. Signal Processing

The embedded harmonic RF tag with integrated sensors can provide numerous advantages like detection, identification and monitoring from the raw signal data. Introduction of signal processing in the scenario expands the spectrum of capabilities. The raw data can also be used to find some hidden information like distance of tag (pipe) and interrogator (surface), data mining of sensor data can help maintaining the infrastructure's efficiency and prognostics can help mitigating the potential high risk accidents. The information from the tag can be fundamentally divided into two categories: raw RF data and the sensor data. The RF data (Amplitude, Phase and Frequency) of the received signal can be used to locate the pipe accurately using the concept and principles of RADAR. Additionally, the field for computer science has advanced to process large data set from thousands of sensor tags. The data mining extracts out the useful information from the pool of noisy and environmentally affected data set. The information can be processed further for estimating the damage growth, material degradation, and ultimately the operating life time.

In this work, distance estimation using RF data is shown with a centimeter accuracy, and the data mining and pipeline prognostics are investigated.

4.3.1. Distance Estimation

A close estimation of pipe burial depth using tag sensor is also a key feature to this project. The distance between electromagnetic source and observer can be estimated independently using two parameters i.e; time of flight or the phase of received signal. The time-of-flight estimation technique records both the time at which signal leaves the transmitter and reaches the receiver and estimates the distance according to the speed of propagation of signal into that medium. It requires a very high frequency and super accurate clock that may not be possible with current scenario due to passive tag and different receiving frequency. On the other hand, the phase of the signal can be detected at receiver's end where we have more degree of freedom in terms of power and machinery.

The distance estimation from phase requires a multiple frequency transmission and it is possible to accurately calculate the separation out of it. Initially, a homogeneous and noise free medium is chosen for start. Fig. 31 show the propagation of signals at five different frequencies in noise and attenuation free environment. The phase of signal after travelling 2-m in free space is observed shown in Table 4.

FREQUENCY	NOISE FREE PHASE	Noisy Phase
928-MHz	67.2º	63.94º
923-MHz	54.84º	52.27º
919-MHz	46.0º	47.32º
913-MHz	30.83º	33.23º
902-MHz	4.8º	1.28º

Table 4

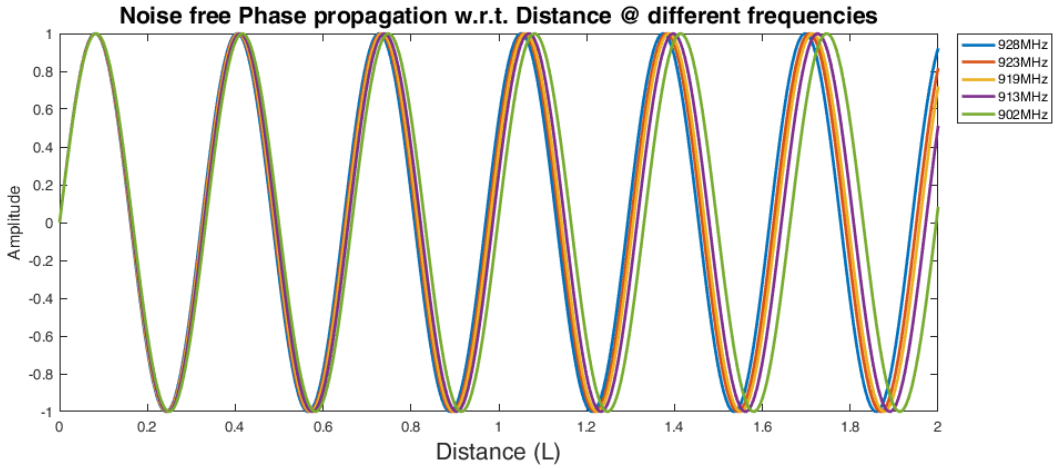

Fig.4.32. Pseudo data for the noise free propagation in air

Distance estimation is as follows:

Algorithm: Distance estimation using phase

Step1**:** Input: Phase $\boldsymbol{\phi}$), Highest and Lowest frequencies $\boldsymbol{f_1}$ **and** $\boldsymbol{f_N}$), No. of transmission (N).

Step2**:** Beat Phase $\boldsymbol{\Phi_i}) = [\boldsymbol{\phi_1} - \boldsymbol{\phi_i}]_{2\pi a}$ for $\mathbf{1} \leq \boldsymbol{i} \leq \boldsymbol{N}$

Step3**:** Beat Wavelength $\wedge_i) = \boldsymbol{ac}/[\boldsymbol{f_1} - \boldsymbol{f_N}]$

Step4**: Initialize:** $\boldsymbol{M_1} = \mathbf{0}a$

Step5**:** $\boldsymbol{M_{i+1a}} = \boldsymbol{round}\left[\left(\boldsymbol{M_{ia}} + \frac{\boldsymbol{\Phi_{ia}}}{\boldsymbol{2\pi}}\right)\frac{\wedge_{ia}}{\wedge_{i+1a}} - \frac{\boldsymbol{\Phi_{i+1a}}}{\boldsymbol{2\pi}}\right]$

Step6**:** $\boldsymbol{L_c} = \boldsymbol{M_N} \wedge_{\boldsymbol{N}} + \frac{\boldsymbol{\Phi_N}}{\boldsymbol{2\pi}} \wedge_{\boldsymbol{N}}$

The distance from given phase using above algorithm is estimated to be 2-m that is correct and proves the fidelity of algorithm for noise free and homogeneous medium. Moreover, the algorithm is also tested for noisy measurement. Fig. 4.33 shows the noisy signal of length 2-m and observed phase is shown in Table 4.

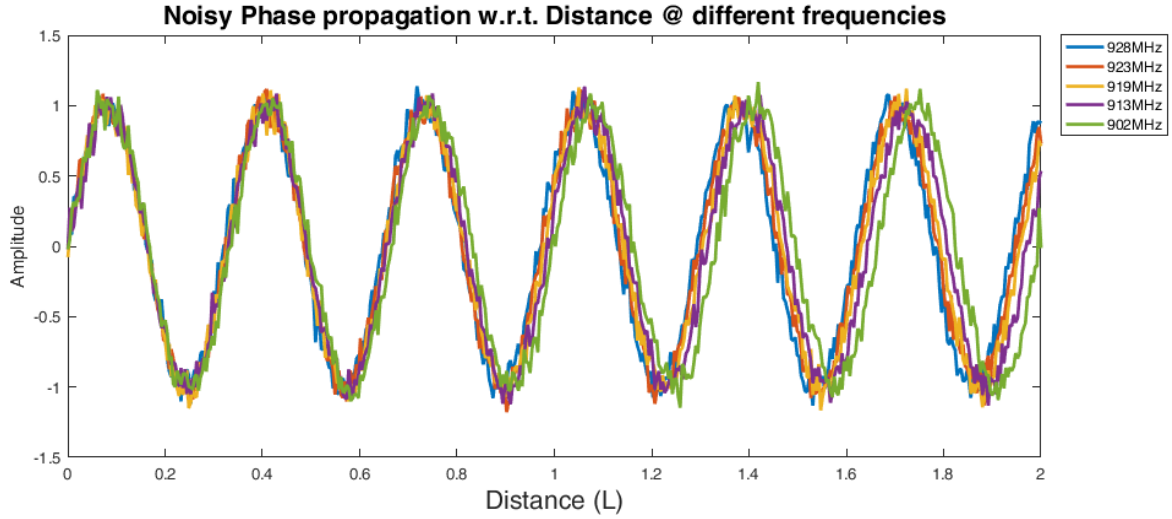

Fig.4.33. Pseudo data of sine wave propagation with white noise

With added white noise the phases at 2-m distance are shifted, the output of algorithm is 1.88-m which is a close approximation of original signal. In practical cases, the noise and the original signal comes hand in hand. The use of better phase detectors and filter may eliminate some of the noise but can't provide a very clean signal. So we can conclude that by using above algorithm, a distance can be estimated in close approximation with some low tolerance.

The signal propagation in lossy medium has also been tested, the measured phases in noise free environment are same as before because the attenuation factor is known and gives a correct distance estimation, shown in Fig.4.34. The noise changes the phase due to randomness but the algorithm converges to 2.3544-m, a close approximated solution.

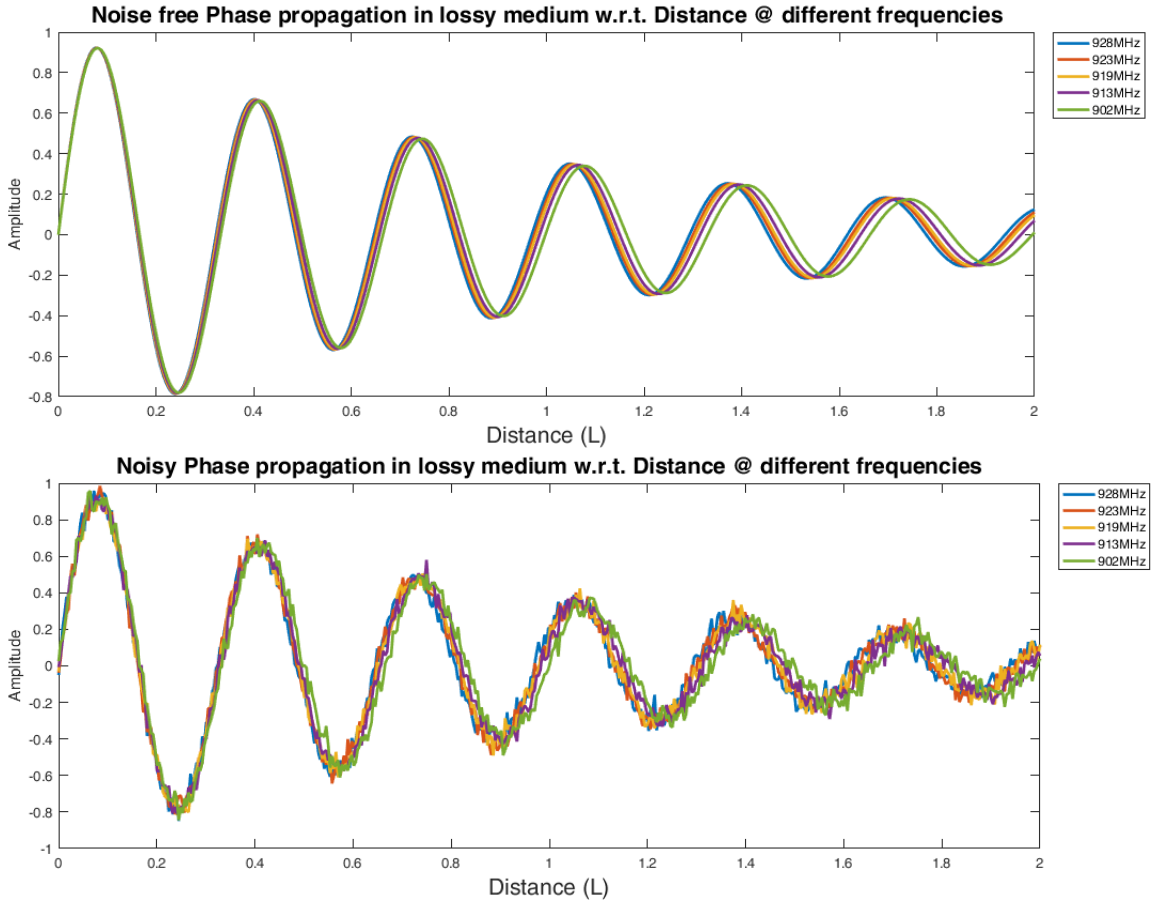

Fig.4.34. Noise free and white noise sinusoid with attenuation coefficient

Experimental Results (One Way)

The distance estimation algorithm, tested in previous section is able to give a close approximation of the separation in between source and detector. The pseudo data is generated under assumption of single tone sinusoid signal with a given attenuation factor. Theoretically, the phase information of received signal can be used to approximate the distance. The theory is tested by the experiment with its block diagram shown in Fig. 4.35.

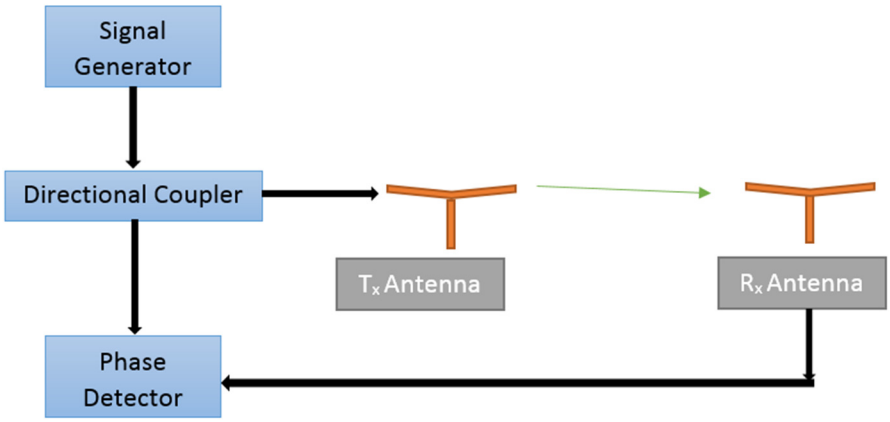

Fig. 4.35. Bock diagram of the single side propagation of RF wave

The phase detector (AD8302) gives an output voltage in accordance to the phase difference between two input signals. The reference signal is a part of the signal fed into the transmitting antenna and the received signal is used for checking the phase difference.

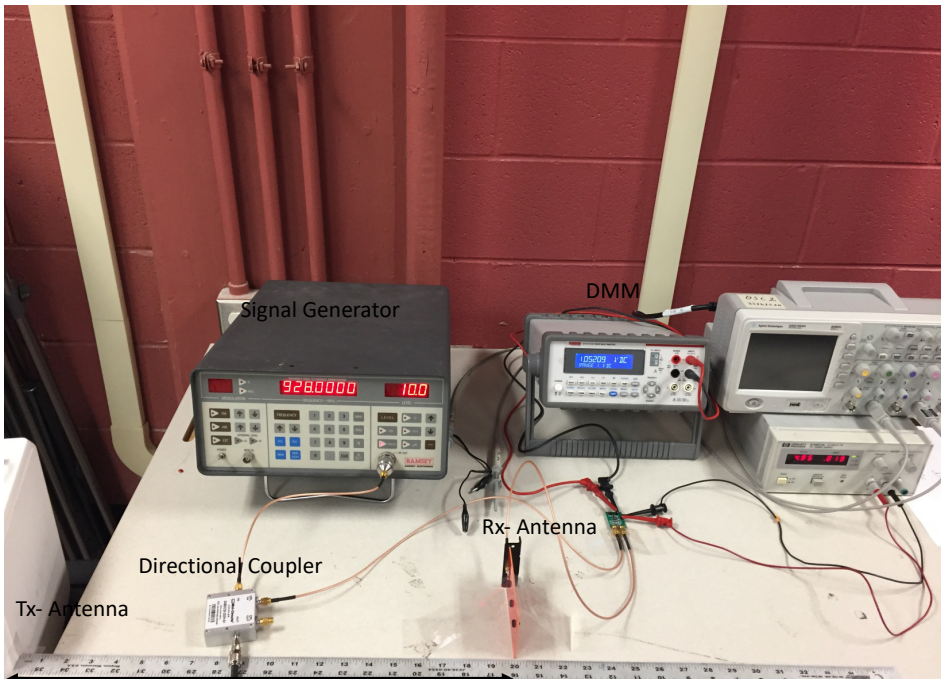

Fig.4.36. Measurement setup for single side distance estimation

The change in voltage (phase) vs distance is shown in Fig. 4.37. The output voltage representing phase changes over distance and repeats the pattern with each wavelength.

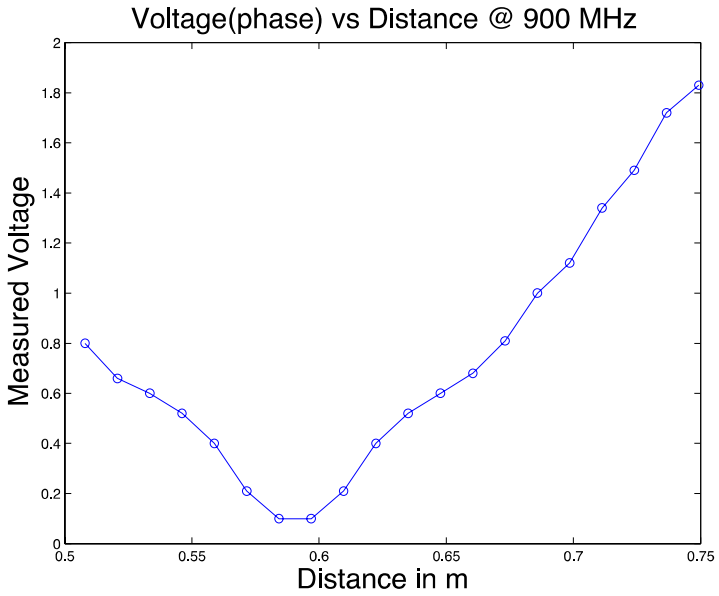

Fig.4.37. Measured phase in voltage at different spatial points

The phase difference between two signals are recorded at five different frequencies by keeping a constant separation in between transmitter and receiver. The measured voltages and translated phase are shown in Table 5.

FREQUENCY	MEASURED VOLATGE (V)	TRANSLATED PHASE (DEGREE)
928-MHZ	1.05+-0.02	17.25
923-MHZ	1.01+-0.02	13.85
919-MHZ	0.97+-0.02	12.70
913-MHZ	0.87+-0.02	4.60
902-MHZ	0.75+-0.02	1.30

Table 5

The separation between transmitter and receiver is computed using the distance estimation algorithm. The measured phases get translated into 0.564m, which is a close estimation to the actual distance (0.5m) between transmitter and receiver. The occurrence of the small offset may be due to the presence of the noise in the system. Additional experiment is also performed with the separation of 1m and translated phases are shown in Table 6. The computed distance was 1.27-m.

FREQUENCY	MEASURED VOLATGE (V)	TRANSLATED PHASE (DEGREE)
928-MHZ	1.32+-0.02	33.45
923-MHZ	1.12+-0.02	25.85
919-MHZ	1.1+-0.02	20.15
913-MHZ	1.06+-0.02	17.85
902-MHZ	0.81+-0.02	1.45

Table 6

The experimental setup for acquiring the phase information is improved to get better accuracy. In previous section, we could estimate the separation between source and target with an error of 27% in a meter. The 27% error margin in a meter is not so good for practical use. So the new idea is built upon previous method to estimate the depth or separation more accurately.

For a specific separation (r), signal at multiple frequencies needs to be transmitted and received. The received signals have a different corresponding phase. The separation can be defined as follows using the signal parameters.

$$r = n_i\lambda_i + \phi_i^{\lambda} + \delta_{ia}^{\lambda}$$

Where,
r, is the depth needs to be estimated
$n_i\lambda_i$, is the number of wavelengths for ith corresponding frequency
ϕ_{ia}^{λ} is measured phase in unit of wavelength
δ_{ia}^{λ} noise in system

The above equation would be true for all frequencies. In the above equation wavelength (λ_i), measured phase (ϕ_{ia}^{λ}) are known, number of wavelength (n_i) can have a bound according to the largest distance needs to be measured and noise (δ_{ia}^{λ}) also has a bound of ± 15°. The only unknown parameter is separation (r) can be found by solving the following minimization problem for n_i and δ_{ia}^{λ}

$$\arg\min_{n} \sum_{i=1}^{m-1} \left|\left(n_m\lambda_m + \phi_m^{\lambda} + \delta_m^{\lambda}\right) - \left(n_i\lambda_i + \phi_i^{\lambda} + \delta_i^{\lambda}\right)\right|$$

The above equation finds a combination of n's for with all the constraints over $n_{ia}$and δ_{ia}^{λ} are satisfied. An ideal situation with no noise has been generated to test the developed algorithm. The phase of the received signal is shown in Fig.4.38 after multiple distances.

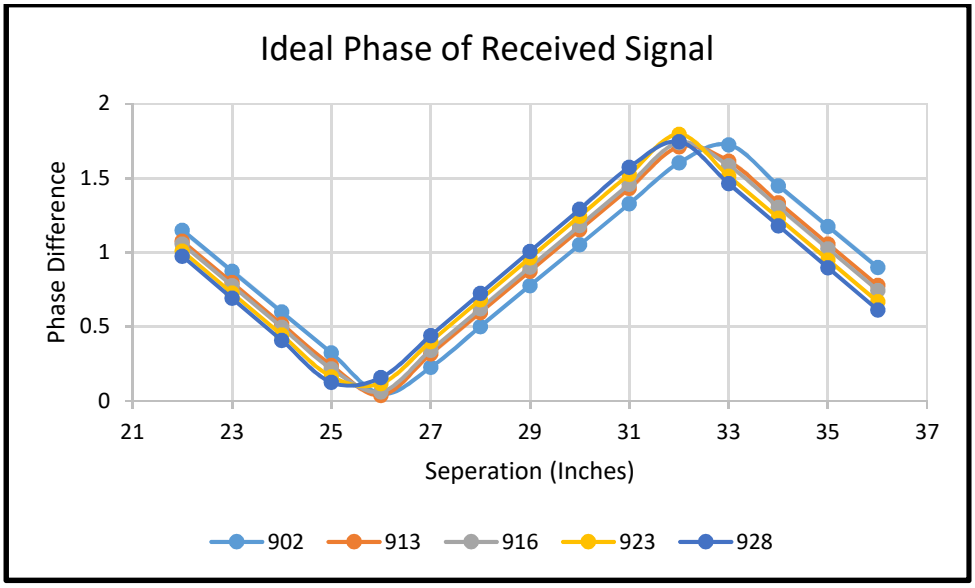

Fig.4.38. Pseudo phase data for multiple frequency propagation

According to above mentioned ideal data, the estimated distance was a perfect match. For all shown distances with a separation of an inch are estimated correctly. It proves that the developed algorithm is working correctly. Now it's time to test the new method over real measured data. Fig.4.39, shows the measured phase at the corresponding distance. The phases are shifted by the RF devices like directional coupler, transmitting antenna, receiving antenna and transmission lines.

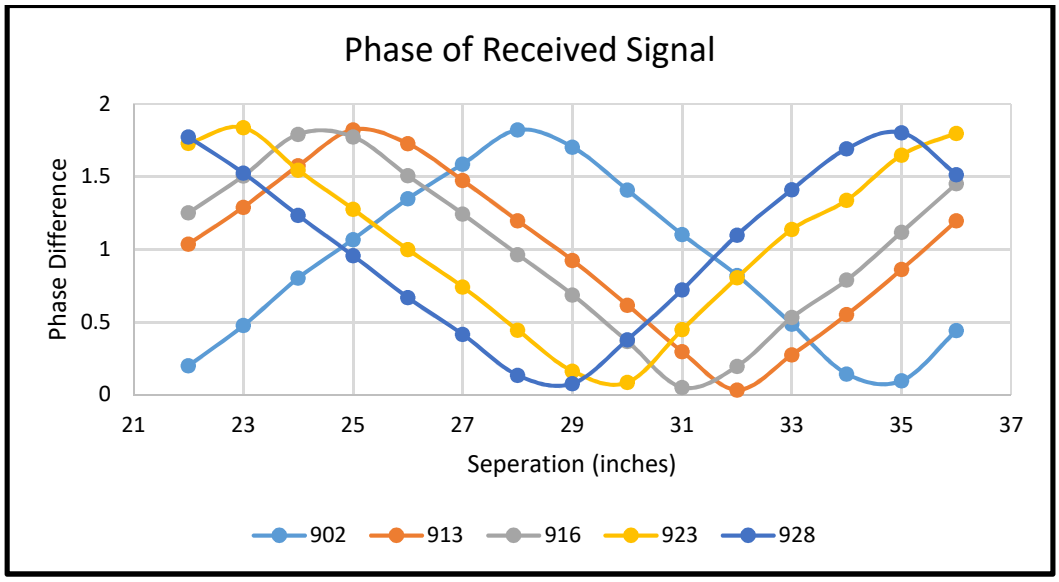

Fig.4.39. Measured phase data at multiple frequencies with phase offset

For each frequency there is a respective phase shift, which needs to be referenced out before estimating the distance. The phase can be referenced out by comparing the readings in ideal situation and measured phase. After correcting the phase shift in data, the received phase signal is shown in Fig.4.40.

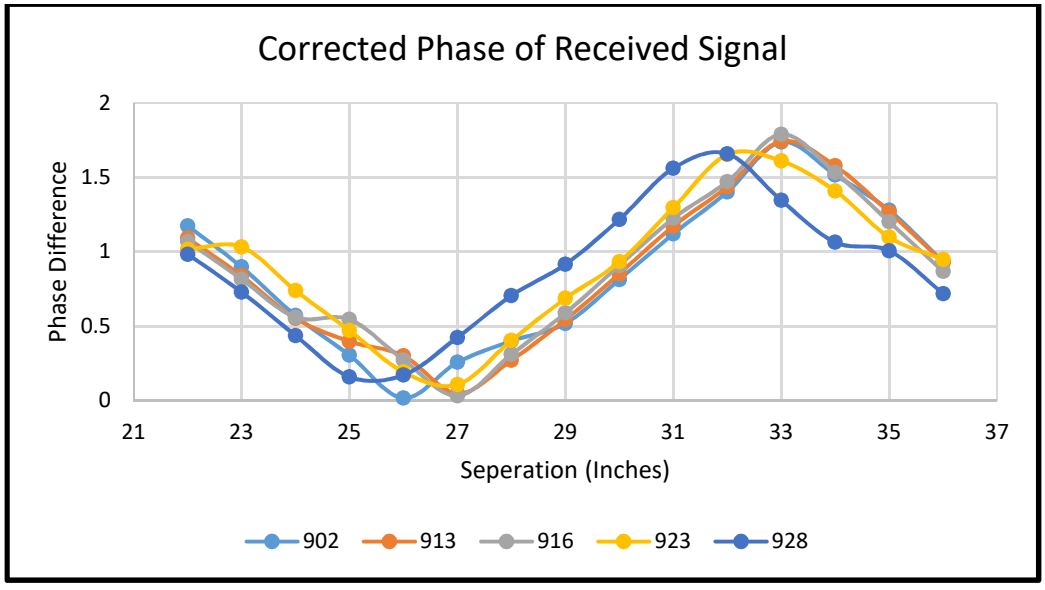

Fig.4.40. Measured phase data after removing phase offset

Feeding the above phase information into depth estimating algorithm give the results shown in Table.7.

Actual Inches	Estimated Inches	Error (%)
24.0	24.4	1.7
26.0	26.88	3.4
30.0	29.07	3.1
34.0	33.49	1.5
36.0	36.68	1.9

Table 7

It can be seen in above table that the error margin of 27% ha come down to ± 3%. The method can locate the target within few inches.

Experimental Results (Two Way)

A new harmonic RFID system (915-1830 MHz) was built to integrate on-tag sensing capabilities and to implement the depth estimation algorithm. The experimental setup block diagram and image are shown in Fig. 4.41 and Fig. 4.42, respectively. It allowed us to test the harmonic tag operating at 915-MHz, which is the center frequency for UHF RFID communication in air- interface.

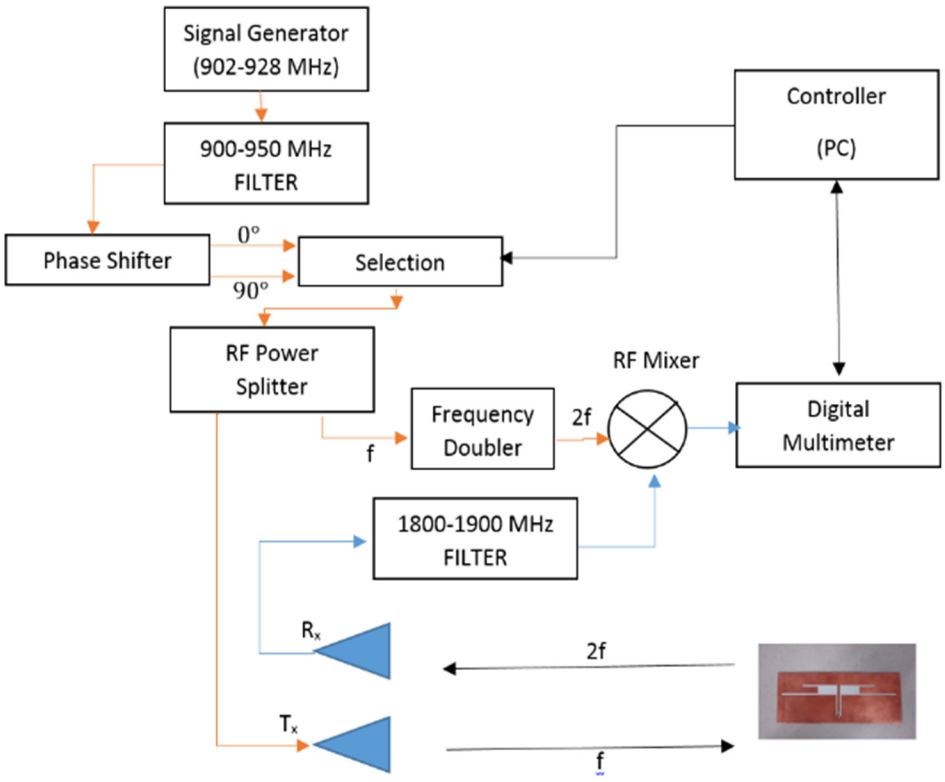

Fig. 4.41. Block diagram for the interrogator and tag distance estimation

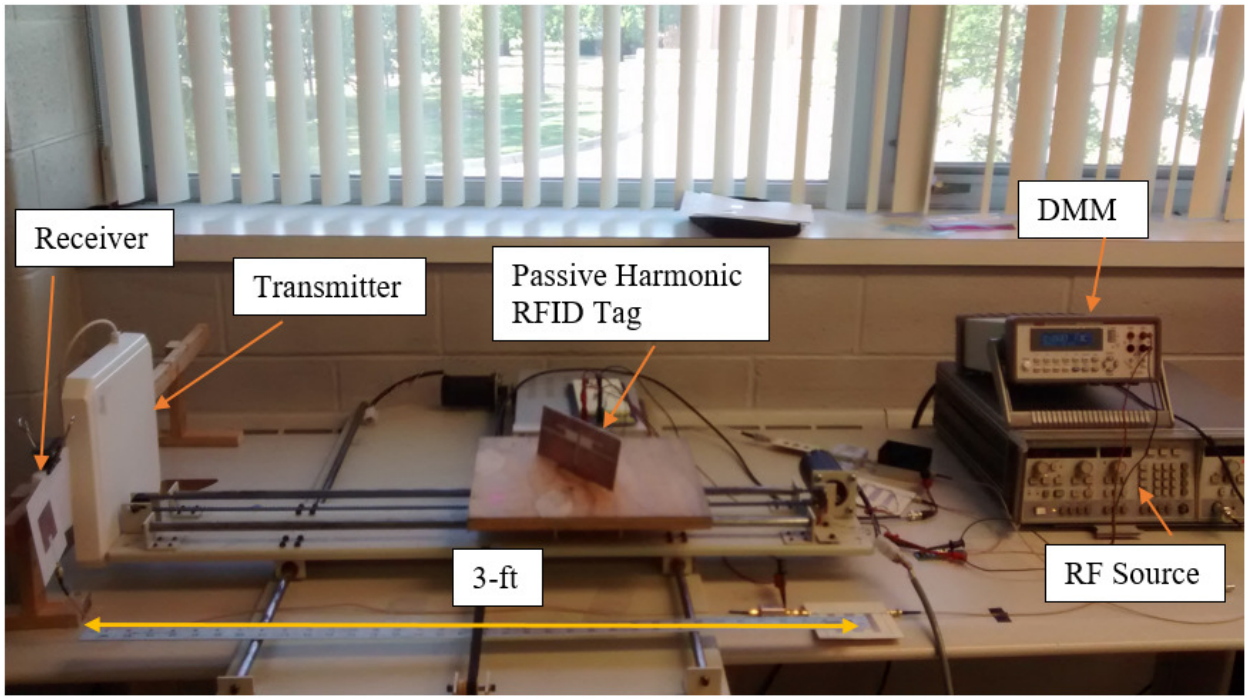

Fig.4.42. Measurement setup for the interrogator and tag distance estimation

The setup is able to detect the shown RF tag up to and including a distance of five feet. The signal strength of received power from the RF tag at the harmonic band is shown in Table 8.

Distance	Signal Strength (dBm)
1- ft	-3.97
2- ft	-5.63
3- ft	-9.42
4- ft	-23.38
5- ft	-29.85

Table 8

The harmonic RF system consists of two operating bands (fundamental and harmonic), which makes this setup more accurate, clutter free and robust over conventional passive RF system. The transmitted and received signal from interrogator can also be used for estimating the distance between the source and the RF tag. The phase of the received signal can be translated into distance using wavelength of the given medium. The uncertainty in estimation arises when the separation between source and tag is greater than a single wavelength, due to the phase repetition after completion of each wavelength. To eliminate this uncertainty several different frequencies can be used for communicating with tag. The interrogator will receive a different phase for each frequency and the combination of all those phases will be unique within a certain range of separation. The maximum range for a given set of frequencies can be calculated by taking least common factor of their respective wavelengths. After that maximum distance, the combination of phases will start repeating again. More number of frequencies can be introduced for increasing the range of the distance estimation system.

The forward propagating signal (f_o) and the backward propagating signals ($2f_o$), both will have a net phase shift of ϕ^F and ϕ^H respectively, shown on Fig.4.43. The interrogator receives a phase that is the summation of the fundamental (ϕ^F) and the harmonic (ϕ^H) phase.

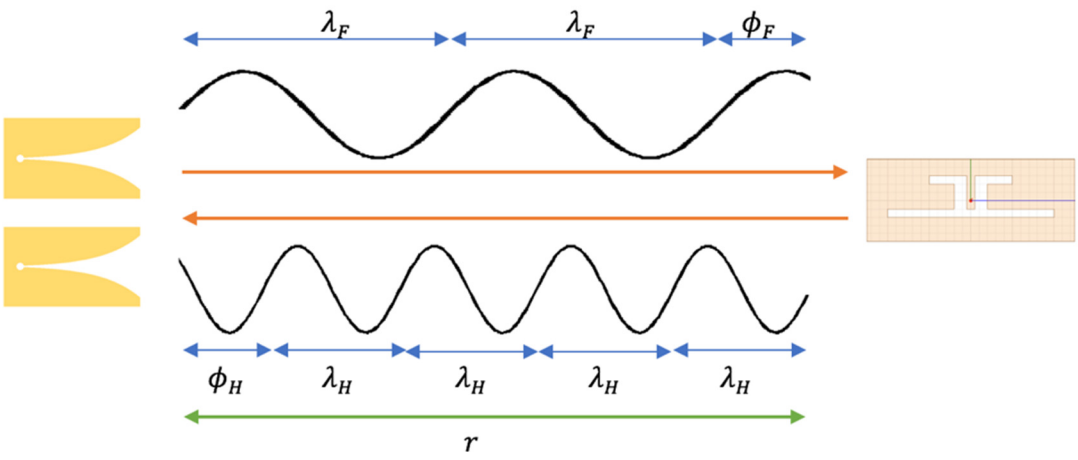

Fig.4.43. Phase shift due to propagation at fundamental and harmonic frequency

The separation r between the source and the tag can be presented as Eq. 1 and 2 for both bands of frequencies where n and m are the number of completed fundamental (λ^F) and harmonic (λ^H) wavelengths, respectively. The wavelength is assumed to be a known parameter for all equations shown below.

$$\boldsymbol{r = n\lambda^F + \phi^F + \delta^F} \quad 1$$

$$\boldsymbol{r = m\lambda^H + \phi^H + \delta^H} \quad 2$$

The distance travelled by the signal from transmitter-to-tag-to-receiver is double of the given separation *r*, as in Eq. 3.

$$\boldsymbol{2r = n\lambda^F + m\lambda^H + \phi^F + \phi^H + \delta^F} \quad 3$$

To estimate the unknown separation *r* from the given set of parameters, *n* and *m* needs to be calculated from Eq. 1 and 2 using the following optimization approach:

$$\min\left(n_k\lambda_k^F + m_k\lambda_k^H + \phi_k^F + \phi_k^H - n_i\lambda_i^F - m_i\lambda_{ia}^H - \phi_i^F - \phi_i^H + \delta_i\right)a$$

Where, $i = 1,2,3,\ldots,k-1$ and *k* is the total number of operating frequencies.

A pseudo harmonic phase data is generated for testing the modified distance estimation algorithm. Two set of data's are generated: A) with no offset or assuming all the frequency signals are starting at reference phase = 0, B) with offset data creates a similar real world situation where the frequency signal can have any arbitrary reference phase, shown in Fig. 4.44.

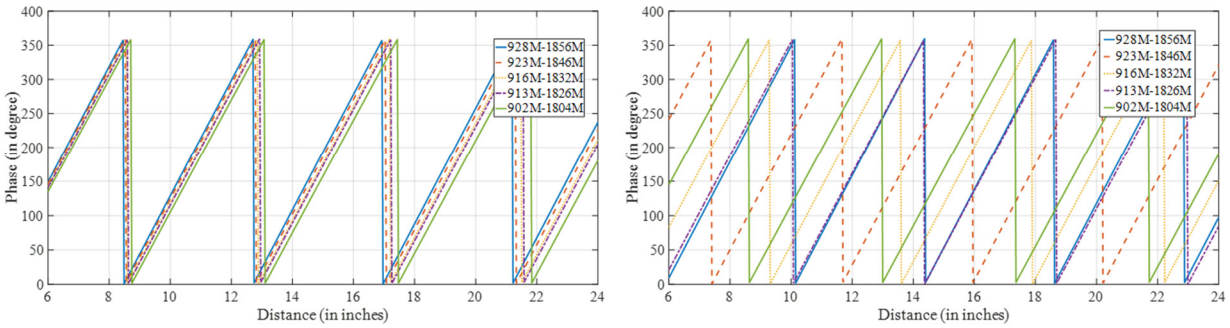

Fig.4.44. Pseudo phase data from harmonic tag at multiple frequencies

Table 9 shows the results of distance estimation algorithm based on NSGA-II. Starting with a population size of 40 and 100 total number of generation are sufficient for unwrapping phase from pseudo data. Due to the absence of noise and also the known phase offset gives the accurate results with no error.

Actual Distance (inches)	Estimated Distance (without offset)	Estimated Distance (with offset)
8	8.0	8.0
12	12.0	12.0
16	16.0	16.0
20	20.0	20.0
24	24.0	24.0

Table 9

The phase data is acquired using the developed harmonic RF system operating at 915-1830 MHz bands. All the operating frequencies were selected within the current UHF RFID protocol.

The acquired RAW phase data is the output of the mixer AD8320 shown in Fig. 4.45. The phase data is processed further to eliminate the phase uncertainty due to same voltage level associated with two phases. Phase data is processed according to the slope, if the slope is positive the phase is associated with angles less than 180 and if the slope is negative the phase is associated with angles greater than 180.

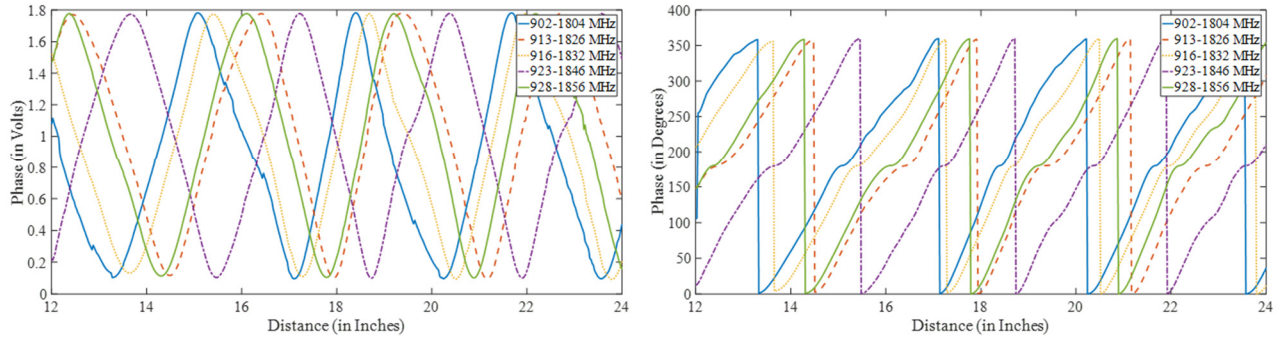

Fig.4.45. Measured phase data from harmonic RF Tag

The distance estimation algorithm is further applied to the experimentally acquired data and the results are shown in Table 10.

Actual Distance (inches)	Estimated Distance	Error Percentage
14	13.2	5
16	15.6	2.5
18	18.7	3.8

Table 10

The harmonic communication based distance estimation is demonstrated with a highly improved accuracy. The back reflected signal from the passive RF tag in harmonic configuration gives a spatial resolution of 3 times of the fundamental frequency.

4.3.2.Data Mining

Data mining technologies have been a field of study in the last decade providing industries with improved and optimized decision making procedure for different applications. The objective of using these techniques is to extract useful and predictive information from large databases for improving the operational efficiency of the industrial supply chain, logistics, inventory tracking, and asset monitoring. Data mining focuses on automating the handling of large data and to extract useful information for multiple applications simultaneously and in an efficient manner. The user issue queries to the data mining algorithms that provides an output accordingly. The mining algorithms should be able to understand the queries and scan through the complete data set for extracting the information. A number of data mining techniques exist that finds data patterns within a large data with or without any prior knowledge and are able to provide the pattern information to predict certain outcomes to optimize and improve the efficiency of the system.

Conventionally the source of data for mining algorithms was manual entries, but recently the trends are changing and industry is moving towards more efficient and automated solution based on RFID's. RFID provides a layer in between physical world with real hardware and digital world with processing algorithms. It provides numerous advantages regarding cost and time. The RFID's can provide the digital information in real time that can be stored in local units or cloud. The data mining algorithms has real-time access to these data pools and able to execute the queries for analysis and prediction.

The concept of data analysis and prediction using data mining is a two-step process. First, the raw data is pre-processed to filter the unwanted data or it can be called data reduction followed by analyzing the filtered data using a data mining algorithm. The functionality of the algorithm is to figure out correlations or patterns among the large data for the purpose of classification, prediction, clustering, association, and analysis. The algorithms are fine-tuned for the type of data being processed. For example, Radio Frequency Identification (RFID) data. In industrial supply chain management, radio frequency identification (RFID) tags are used for real-time product tracking and tracing, inventory tracking, and sensing. These tags generate a huge amount of data periodically such as user ID, geo-location, sensing data and so on. It is a challenge to maintain and analyses a large data base in real-time and hence data mining algorithms plays a crucial role in improving the data analytics to perform real-time changes to the operation of the supply chain.

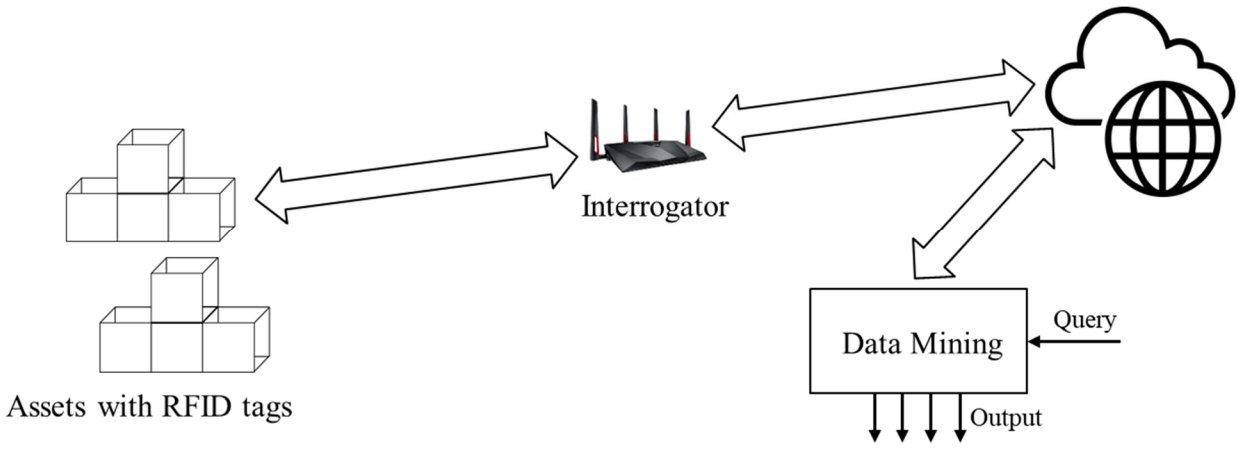

Fig. 4.46. Overview of the RFID data transfer and mining system

The million miles long pipeline infrastructure requires an automated system for monitoring the transportation medium as well as the flowing asset. RFID based marking systems seems like an appropriate choice but this solution also comes with other challenges. For example, a million mile long pipeline with one RFID tag every 10 m and interrogated once every day would generate 1.6 terabytes of data with 160 million tags generating same amount of tuples (each tuple 10kilobyte with sensing data). The mining over the data logged for several days or months poses a big problem for classification, cluster, and prediction. It requires some very efficient algorithm and a problem specific solution to funnel down the important information.

Pipeline monitoring using RFID sensors can provide location markers for buried pipes as well as sensors for conditional monitoring and predictive maintenance. Interrogating these RFID tags periodically, the data is generated and contains location as well as sensing information. The data needs to be analyzed in order to check the occurrence of events that allow predictive maintenance. A good data mining algorithm is required to classify the data rapidly and alert the stake holders if an event has occurred. For example, analyzing the sensing data to discover a pipe leakage event or to identify the chemical compound it transports and provide information to the location of the leakage in order to promote safety and effective maintenance.

The developed algorithm should be able to classify different cluster of data based on different applications with a time line to provide information on predictive maintenance. Moreover, the algorithm should be able to handle large real-time data to analyses patterns rapidly. For this purpose, an efficient filtering technique is desired that improves the efficiency of the mining technique by reducing data redundancy. Rapid analysis of the real-time data in a cost-effective manner involves usage of lesser storage capacity and ability to decide and discard unwanted data quickly. The algorithm should be able to classify data for multiple events simultaneously such as pipe leakage, corrosion gradient or structural damage and provide real-time feed back to the stake holders. The algorithm should be able to compress data without losing the accuracy of the information since most of these events require physical maintenance such as pipe leakage and has a cost associated with it.

4.3.3.Pipeline Prognostics

Pipelines are the primary means of transportation for natural oil and gas. The widespread industrial applications and common households need of these natural resources leads to a huge pipeline infrastructure. The buried and surface pipelines (gathering, transmission, and distribution) are primarily made from steel, polymers and composites. Each material has its own advantages like high strength, light weight, corrosion resistance, etc. Despite all these advantages, there are several issues that get associated during the manufacturing, installation and operation, hence it requires a routine maintenance and replacement for avoiding any failure or complete shutdown. The minor manufacturing defects are inevitable and may evolve during operation and grows rapidly due to cyclic pressurization.

Fig.4.47 shows the health degradation of a pipeline over time. The current health can be quantitatively measured using the distributed sensor network or structural health monitoring techniques installed over the pipeline infrastructure. The proper maintenance according to the sensor data can extend the usable life or the number of operation cycles.

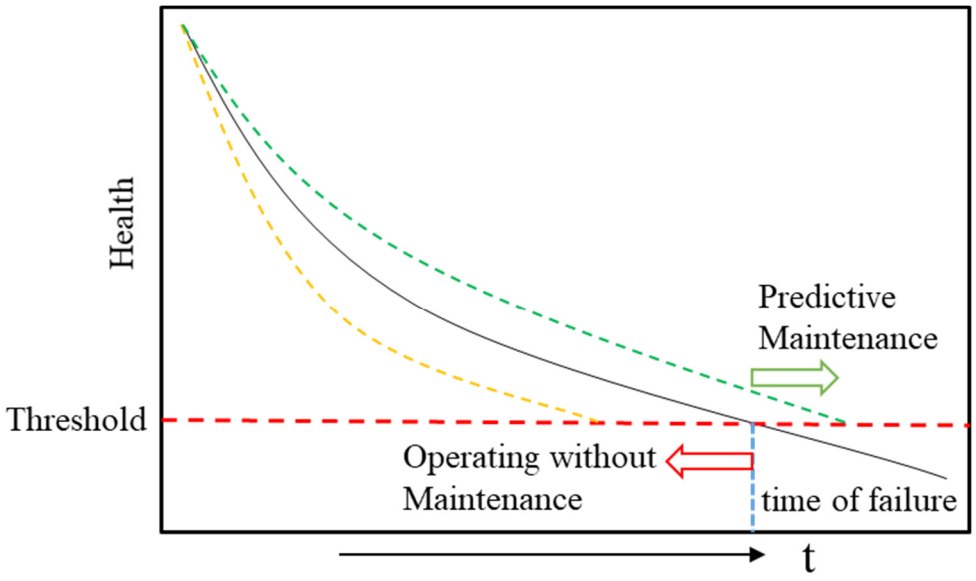

Fig.4.47. Pipeline health over time with and without maintenance

Predictive maintenance can be a tool for efficiently managing and mitigating the potential risks of failures. But predicting a failure is still a challenging task due to involved uncertainties in the system. For example, the environmental conditions, heat cycles, variable pressure range, data inaccuracy, device error, etc. are critical parameters for prognostics methods.

The goal of damage prognosis is to construct the damage growth curve or estimate function f which maps health index (y) computed from NDE measurements for every time instants (or loading cycle) x at which NDE is performed.

$$\boldsymbol{y = f\ x\ 1{:}k); \theta)} \qquad 4$$

f is a generalized damage growth model described by parameters θ. Using estimated values of θ, future health indices $\hat{y}$ are predicted upto time X_{tha} when the system reaches its failure threshold

Y_{th}or when the system is expected to fail. This information is generally obtained from domain experts.

$$\hat{\boldsymbol{y}} = \boldsymbol{f}\ \boldsymbol{x}\ \boldsymbol{k}+\boldsymbol{1}:\boldsymbol{X_{th}}); \hat{\boldsymbol{\theta}}) \quad (5)$$

For pipeline inspection, information from sensor data measuring the pressure can be used to predict change in general health of the structure which may include both crack initiation and crack propagation in the pipeline geometry. Accurate prediction can be achieved by implementing Bayes inference on measurements data acquired at periodic intervals of time using appropriate damage growth models which may be obtained through numerical modeling of cracks in pipeline geometry or through experimental failure testing of the structures.

Theory of Bayes Inference

Bayes inference is widely used for estimation of damage-growth function parameters $\hat{\theta}$which derives the posterior distribution by updating an initial prior estimate combined with information obtained from new measurements, according to equations (6) - (10).

$$\boldsymbol{f_{Y,\Theta}}\ \boldsymbol{y},\boldsymbol{\theta}) = \boldsymbol{f_{Y|\Theta}}\ \boldsymbol{y}|\boldsymbol{\theta})\boldsymbol{f_{\Theta}}\ \boldsymbol{\theta}) \quad (6)$$

$$\boldsymbol{f_{Y}}\ \boldsymbol{y}) = \int_{\boldsymbol{\Omega}} \boldsymbol{f_{Y,\Theta}}\ \boldsymbol{y},\boldsymbol{\theta})\boldsymbol{d\theta} = \int_{\boldsymbol{\Omega}} \boldsymbol{f_{Y|\Theta}}\ \boldsymbol{y}|\boldsymbol{\theta})\boldsymbol{f_{\Theta}}\ \boldsymbol{\theta})\boldsymbol{d\theta} \quad (7)$$

$$\boldsymbol{f_{Y|\Theta}}\ \boldsymbol{y}|\boldsymbol{\theta}) = \frac{\boldsymbol{f_{Y,\Theta}}\ \boldsymbol{y},\boldsymbol{\theta})}{\boldsymbol{f_{Y}}\ \boldsymbol{y})} = \frac{\boldsymbol{f_{Y|\Theta}}\ \boldsymbol{y}|\boldsymbol{\theta})\boldsymbol{f_{\Theta}}\ \boldsymbol{\theta})}{\boldsymbol{f_{Y}}\ \boldsymbol{y})} \quad (8)$$

$$\boldsymbol{E}\left[\left(\hat{\boldsymbol{\theta}}\ \boldsymbol{y}\right)-\boldsymbol{\theta}\right)^{\boldsymbol{2}}\right] = \int_{-\infty}^{\infty}\int_{\boldsymbol{\Omega}}\left(\hat{\boldsymbol{\theta}}\ \boldsymbol{y}\right)-\boldsymbol{\theta}\right)^{\boldsymbol{2}}\boldsymbol{f_{Y,\Theta}}\ \boldsymbol{y},\boldsymbol{\theta})\boldsymbol{dyd\theta} \quad (9)$$

$$\boldsymbol{E}\left[\left(\hat{\boldsymbol{\theta}}\ \boldsymbol{y}\right)-\boldsymbol{\theta}\right)^{\boldsymbol{2}}\right] = \int_{-\infty}^{\infty}\boldsymbol{f_{Y}}\ \boldsymbol{y})[\int_{\boldsymbol{\Omega}}\left(\hat{\boldsymbol{\theta}}\ \boldsymbol{y}\right)-\boldsymbol{\theta}\right)^{\boldsymbol{2}}\boldsymbol{f_{\Theta|Y}}\ \boldsymbol{\theta}|\boldsymbol{y})\boldsymbol{d\theta}]\boldsymbol{dy} \quad (10)$$

For complex damage growth functions, it is non-trivial to solve equation (10) analytically. Approximate solution of Bayes inference or $E(\theta|Y)$ can be achieved by Kalman filtering for linear systems with Gaussian noise. However for non-linear systems, particle filtering is a more suitable approach. Apart from computational ease, particle filtering approach can be implemented in systems with non-Gaussian noise as well.

5. Conclusion

In this report a harmonic tag is proposed, which can have a better S/N ratio compared to the conventional single frequency RFID tags. The frequency and power of the designed harmonic tag was optimized at fundamental transmitted frequency at 400 MHz and received frequency at 800 MHz based on the antenna size and power budget analysis of the soil medium. The soil medium was characterized from 100 MHz to 700 MHz with different volumetric moisture content using a coaxial cable to obtain the parameters for power budget analysis. A nonlinear transmission line based harmonic tag was proposed for the buried pipe application as the tag could generate the harmonic power efficiently at a low received power. The tag could communicate upto distance at 9 feet in air medium. Apart from nonlinear transmission line based tag, a Schottky diode based tag was also reported. However, the schottky diode based tag is much effective at high frequency operation (~2 GHz) and has small size with simple structure. On the other hand, the nonlinear transmission line based tag worked effectively at low frequency but have bulky size because of low frequency operation. Packaging of the harmonic tag is very important as it is needed to be integrated with existing plastic pipes. Hence, injection molding was performed on an existing harmonic tag and the tag could withstand temperature of more than 150^0 C.

The designed harmonic RF tags are ideal for detection and localization. Furthermore, the capability of the RF tags can be enhanced by integrating a sensory layer that provides the local information. The pressure and humidity on tag sensing capabilities are investigated and the wireless passive sensors are designed. The capacitive pressure sensor is integrated with a harmonic RF tag, which introduce a change in the phase of the reflected signal according to the applied pressure. The designed humidity sensor works on a principle of the frequency resonator, which shifts its resonance according to the moisture contents in the soil. Additionally, the signal processing of the raw RF data allows us to extract the distance information of the RF tag and the interrogator. The investigated methods for data mining and prognostics allows to extract the information from the large scale integration and estimate the heath of the infrastructure.